

The Investigation of the Interaction of a Sodium Atomic Beam with a Strong Standing Wave Laser Field

by

QIMING LI



A thesis submitted for the degree of Doctor of Philosophy of the
Australian National University

August 1994

Statement of Authorship

The contents of this thesis, except where indicated by references, are entirely my own work.

A handwritten signature in black ink, appearing to read 'Qiming Li'.

Qiming Li

August 1994

Acknowledgments

I sincerely thank my supervisors, Dr H.-A. Bachor, K.G.H.Baldwin and D.E.McClelland, for their carefully considered advice and opinions on all aspects of this work, and for their wholehearted support of the project. Without their wealth of experience in both academic and bureaucratic matters, this work would not have been possible.

I sincerely thank my adviser, Dr P.T.H.Fisk in the CSIRO, for his constructive discussion.

I am very grateful to my fellow graduate student B.W.Stenlake and Dr I.C.M.Littler, for their help in the experiments and useful discussion.

Finally, I would like to thank Mr. B.Brown in the workshop for his technical help for making parts of the experimental setup.

Abstract

The interaction of a beam of two level atoms with a standing wave laser field has been the subject of extensive investigation in recent times. A standing wave perpendicular to an atomic beam allows the manipulation of the transverse velocity distribution. The interaction of an atomic beam with a strong standing wave laser field has been systematically investigated by both theoretical simulation and experiment in this thesis.

We have developed a numerical model based on a continued fraction solution for the light pressure forces to simulate the near perpendicular interaction of an atomic beam with a strong standing wave laser field.

The reshaping of the transverse spatial profile of an atomic beam by a perpendicular, near resonant, standing wave laser field is investigated for red detunings using a longitudinal velocity selective detection system. The experimental dependence of the reshaped profile on the longitudinal and transverse atomic velocities agrees well with a continued fraction solution for the light force. In particular, a regime is found where channelling of the atoms near the antinodes of the standing wave produces a central peak in the spatial distribution of the atomic beam in the far field which have also been observed elsewhere.

We found that the central peaks in the spatial atomic profile were formed mainly by two factors: collimation (for transverse velocity $v_t^{in} < 0.1m/s$ in our experimental conditions) and focusing (for $v_t^{in} > 0.1m/s$). For large detunings, the standing wave acts like a conservative potential and the magnitude of output transverse velocity of atoms would be the same as that of input transverse velocity ($v_t^{out} = \pm v_t^{in}$). The atoms with negative $v_t^{out} = -v_t^{in}$ lead to a 1 : 1 focusing of atoms on the atomic beam axis.

For small detunings, the atoms experience non-conservative force and will get heated (for small negative detuning) or cooled (for small positive detuning). Atoms having opposite sign and different magnitude of v_t^{out} will be focused in a variable position on the atomic beam axis depending on the intensity and detuning of the standing wave. The standing wave therefore acts like a zoom-lens. From both experiments and simulation, this zoom-lens property of the standing wave was observed.

If the atomic beam is not in the exact perpendicular position in respect to the standing wave (a few degrees between the atomic beam and the normal to the standing wave beam) the transverse kinetic energy of atoms will be larger than the potential of the standing wave. For fixed detuning, only the spatially averaged force is important. This force is modulated by Doppleron resonances and has no sign change within the small range of transverse velocities in the atomic beam. As a result, the atoms will experience both deflection and Doppleron resonance structure.

The deflection of an atomic beam was both observed experimentally and predicted theoretically. From the simulation, the higher order Doppleron resonance structure was predicted. However, we found that these structures were very sensitive to both the intensity and detuning of the standing wave and consequently these structures are not experimentally observable.

Contents

1	Introduction	1
1.1	Overview of Light Pressure Forces	1
1.2	Outline of the Interaction of an Atomic Beam with a Standing Wave Laser Field	3
1.2.1	Channelling	6
1.2.2	Laser Focusing of Atomic Beam	7
1.2.3	Deflection and Doppleron Resonances	9
1.3	Arrangement of This Thesis	10
2	Theory of Light Pressure Forces	12
2.1	Quantum Mechanical Analogy of Light Pressure Forces	13
2.2	The Density Matrix for a Two-Level System	13
2.3	The Hamiltonian for a Two-Level System Interacting with a Laser Field	14
2.4	Relaxation Processes	15
2.5	The Master Equations	16
2.6	Force Acting on Atom Moving in a Plane Traveling Wave and the Doppler Cooling Limit	19
2.7	Forces Acting on an Atom Moving in a Standing Wave Laser Field	22
2.7.1	A Simple Solution of Gradient Force in a Standing Wave Field	26

2.7.2	Continued Fraction Solution of Forces	27
3	Numerical Simulation	31
3.1	Velocity-Dependent Forces and Doppleron Resonance Structure	31
3.2	Physical Interpretation of the Heating Effect by Using Dressed-State Approach	36
3.3	Approximation of Simple Gradient Force	37
3.4	Simulation of Atomic Motion	42
3.4.1	Atomic Trajectories	45
3.4.2	$v_t^{in} \sim v_t^{out}$ Relationship	48
3.4.3	Effect of Longitudinal Velocity Change	54
3.5	Diffusion Processes	58
4	Experimental Arrangement	63
4.1	Formation of a Two-Level Atom System	63
4.2	Experimental Setup	65
4.3	Interaction Region	70
4.4	Detection System	71
4.4.1	Adjustment of the Interaction Angle	73
4.4.2	Determination Of the Detuning	73
4.4.3	Determination of D_2 Line of Sodium	76
4.5	Measurement of the Standing Wave Laser Beam Diameter	76
4.6	Experimental Procedure	77
5	Heating Effects with Stimulated Emission	80
5.1	Experimental Arrangement and Parameters	80
5.2	Experimental Results	81

5.3	Simulation of the Experimental Results	85
5.3.1	Small Detuning $ \Omega /2\pi \leq 100MHz$	86
5.3.2	Large Detuning $ \Omega /2\pi \geq 500MHz$	89
5.4	Summary	92
6	Focusing (Zoom-Lens) and Collimation of Atoms	94
6.1	Review	94
6.2	Experimental Arrangements and Procedures	95
6.3	Experimental Results	97
6.3.1	Intensity Dependence of Focusing Length of Atoms	105
6.3.2	Detuning Dependence of Focusing Length of Atoms	110
6.4	Simulation Results	115
6.5	Summary	122
7	Deflection and Doppleron Resonances	124
7.1	Experimental Arrangements And Procedures	125
7.2	Experimental Results	126
7.3	Theoretical Simulation of the Deflection	129
7.4	Theoretical Prediction of Higher Order Doppleron Resonances	129
7.5	Summary	140
8	Conclusion	141
	Appendix: Magnetic-Optic Trap	146
	Bibliography	147

Chapter 1

Introduction

1.1 Overview of Light Pressure Forces

Maxwell predicted the strength of light pressure by means of his classical theory of electromagnetic phenomena[1]. In the 1930s, Frisch[2] observed the deflection of a sodium atomic beam by the light pressure of a sodium lamp. Because of the low spectral brightness of the sodium lamp, the beam was deflected by only $0.01mm$. This experiment showed that without a drastic increase in the spectral brightness of light sources, light pressure could not become an effective tool to influence the motion of atomic particles. With the advent of the laser, which can produce a source of intense, coherent, directional and frequency-tunable monochromatic radiation, the experiments became much easier to perform. The first experiments using laser radiation pressure to control the motion of small particles were performed by Ashkin and collaborators[3, 4].

In 1975, Wineland and Dehmelt[5, 6] and Hänsch and Schawlow[7] proposed to use resonant laser radiation for deep cooling of trapped ions and free neutral atoms and, since then, the laser control of atomic motion has become a rapidly developing field of atomic-laser physics. This field has already been discussed in a number of reviews [8]-[16], special issues of scientific journals [17, 18], monographs [19, 20], and conference proceedings [21].

Normally, there are three kinds of interaction between laser light and atomic particles: The first is a destructive interaction (resonance photoionization, etc). The second interaction is known as nondestructive interaction between photons and the internal degrees of freedom of atomic particles (single resonance excitation,

etc.) and the third is the nondestructive multi-photon interaction with the internal and translational degrees of freedom of atomic particles (large change of the atomic momentum by light, resonance light pressure on atoms, etc.).

The third kind of interaction is used to manipulate neutral atoms, especially to cool and trap neutral atoms.

The forces acting on atoms in a laser light field can be separated into two categories. One is called the radiation force which is mainly due to the spontaneous emission of photons and exists in both uniform and non-uniform resonant light fields. The other force is called the dipole force (or the gradient force) which arises from stimulated light-scattering processes and exists only in optical field gradients. The radiation force is now well known, and its various features, such as velocity dependence and momentum diffusion, have been analyzed in detail in terms of cycles involving absorption of laser photons and spontaneous emission of fluorescent photons[22, 23, 41].

The interaction of a beam of two level atoms with a standing wave laser light field has been the subject of extensive investigation in recent times. Standing waves have been used to longitudinally cool[24, 25] and guide[26], transversely collimate[66]-[69], channel[27]-[31], trap[32, 33, 34], deflect[35] and diffract[36, 37] beams of atoms. Recent attention has centered on the use of standing waves as a means of guiding atoms for direct-write lithography[38].

Laser cooling of two-level atoms in a low intensity standing wave laser beam, referred to as Doppler cooling, is well understood. The atoms move in a laser field with frequency tuned below the resonance frequency of an atomic transition and the intensity is less than or near the saturation intensity of the transition. The radiation pressures due to the two counterpropagating waves can be added independently. If the frequency of the laser beam ω is tuned below the atomic transition frequency ω_0 , because of the Doppler effect, a moving atom will be closer to resonance with the traveling wave opposite to the motion of the atom, and farther from resonance with the copropagating wave. The radiation pressure of the opposing wave will predominate, and the atom will be slowed down. Theory accurately describes the dynamics of atomic motion and ultimate cooling temperatures can be precisely predicted[12].

In the case of a two-level atom moving in an intense standing wave, for which

the light intensity is much larger than the saturation intensity of the interaction transition, the force that an atom experiences differs considerably from that at low intensities and is dominated by several fundamentally different physical mechanisms depending on the velocity of the atom and the intensity of the field[62]. The stimulated emission processes, responsible for a coherent redistribution of photons between the two counterpropagating waves, become predominant, but the spontaneous processes are still crucial to the light force on the atom.

In next section, we will outline the interaction of an atomic beam with a strong standing-wave laser light field.

1.2 Outline of the Interaction of an Atomic Beam With a Standing Wave Laser Field

The interaction of an atom with a standing wave field differs fundamentally from the interaction with a traveling wave due to the possibility of photon exchange between the two counter-propagating light fields comprising the standing wave. The importance of such stimulated processes is determined by the atomic saturation parameter $G = 2\omega_R^2/\Gamma^2$ for the light field (amplitude E). Here $\omega_R = \mu E/\hbar$ is the Rabi frequency, and μ and $1/\Gamma$ are the dipole moment and natural lifetime of the atomic transition respectively.

At very low laser intensities for which the atomic saturation parameter $G \ll 1$, spontaneous emission forces dominate. When the laser field is detuned below the atomic resonance, the atom experiences a velocity-dependent viscous damping force responsible for optical molasses, as used for some atom traps[39]. In this classical optical molasses, the total force is simply equal to the sum of the radiation pressure (spontaneous) forces for the two traveling waves which comprise the standing wave. Because the magnitude of the spontaneous emission force is determined by the rate of spontaneous emission events, it is limited by saturation of the atomic transition.

However at high laser intensities, $G \gg 1$, stimulated processes, which arise from redistribution of photons between the two traveling waves, dominate the light force on the atom[40]. Because the redistribution rate is dependent directly on the Rabi frequency and does not saturate at high field strengths, the stimulated force (unlike the spontaneous force) increases with laser intensity.

It is important to note that the stimulated forces in the standing wave are velocity dependent, since the interaction of the atom with the light field is dependent on the Doppler shift with respect to each traveling wave. Indeed, multiple stimulated interactions between the atoms and both traveling waves can give rise to Doppleron resonances[41], when the laser detuning in the rest frame of the atom is equal to an odd multiple of the Doppler shift. Such resonances have been observed in both the longitudinal[45] and transverse[46] motion of atoms in standing waves that were respectively parallel and perpendicular to the atomic beam.

When the velocity of the atom in the direction of the standing wave approaches zero, the stimulated force simply reduces to the usual (velocity independent) dipole or field gradient force. The gradient force is purely conservative and consequently has no effect on the magnitude of the atomic momentum (although it can be used to alter the direction of the atoms[38], or even to diffract them[36, 37]).

But for finite velocities, where the Doppler shift plays an important role in the interaction of the moving atom with the standing wave, the force on the atom is no longer conservative and becomes velocity dependent. At relatively low laser intensities ($G \leq 1$) the force averaged over a wavelength can be a damping or a heating force, depending on whether the laser detuning in the atomic rest frame is positive or negative - exactly the opposite of the spontaneous force case. At higher laser intensities ($G \gg 1$) the situation becomes more complicated: the velocity-dependent dipole force can change rapidly in sign and magnitude as Doppleron resonances come into play for particular velocity groups.

A number of experiments have been performed elsewhere which to some degree have explored the role of these different force regimes on the atomic motion in a standing wave laser field (we consider here the case of strong light fields $G \gg 1$ where stimulated processes dominate). In particular, Aspect et al. and Tanner et al. [66]-[69] have studied the motion of a caesium beam in a strong standing wave aligned perpendicularly to the atomic motion. Similar experiment using sodium atoms was performed in 1990 by Wang et al[70] and in the same group, the collimation and decollimation of an atomic beam in a misaligned standing wave were observed in 1994[71]. These experiments demonstrated that the velocity-dependent dipole force can produce significant cooling or heating of the transverse motion of the atoms for positive and negative laser detuning respectively. Strong collimation of the atomic beam was observed for positive detunings as a result of the transverse

cooling process.

An additional effect was observed in the presence of a heating force (negative detuning): a small peak in the center of the decollimated atomic beam distribution was observed (fig.3 in Aspect et al. and fig.2 in Tanner et al.). This structure was consistent with the trapping of atoms with near zero transverse velocities at the antinodes of the standing wave. Atoms whose transverse kinetic energy is smaller than the depth of the potential produced by the negatively detuned laser field are channelled in the potential “valleys” centered on the antinode. More direct evidence for such channeling processes have been observed in the experiments[27]-[31]

However, the two experiments by Aspect et al. and in Tanner et al. used hot-wire detectors to measure the far field atomic beam spatial distribution. Although the hot-wire ionization detectors are easy to handle and sufficiently sensitive, they have disadvantages. The main disadvantage is that they are velocity insensitive and can not detect different velocity group of atoms. They therefore measured the final position of the atoms perpendicular to the atomic beam (which is related to the final transverse velocity), but were unable to resolve the detected atoms according to their velocity along the atomic beam (the longitudinal velocity). The resultant spatial profiles thus represented a summation of different transverse and longitudinal velocity contributions. The third experiments by Wang et al. used a laser beam to detect the atomic profile, but the detection laser beam was set to be perpendicular to the atomic beam and it was also longitudinal velocity insensitive. Also in this experiment, the detuning of the laser beam was controlled using an AO modulator which could only provide to do the experiments in small detuning region and it was impossible to do experiments for large detunings.

In a similar experiment, Chen et al.[69] used a strong, positively detuned standing wave to transversely cool a beam of lithium atoms traveling perpendicular to the laser field. Atoms trapped near the nodes of the standing wave were channelled and then cooled adiabatically by gradually reducing the standing wave intensity in the direction along the atomic motion. To ensure the adiabatic nature of the process, and to increase the fraction of atoms channelled in the high intensity region (which required small transverse velocities), only slow atoms (900m/s) in the low velocity tail of the thermal atomic beam distribution (centered at 1700m/s) were detected in the far field. To achieve this, a probe laser with a coarse longitudinal velocity resolution of 150m/s was used to measure the spatial distribution. Transverse

cooling to near the recoil limit was observed using this technique. Experiments by the same group[72] were also carried out at negative detunings, but under conditions where strong momentum diffusion washed out any effects due to channelling.

In this thesis, we investigate the competing role of the heating and channelling effects (see below), observed in the earlier hot-wire detector experiments, by separately resolving the longitudinal and transverse velocity components. The main features of the experimental profiles (both heating and the formation of a small peak in the center of the atomic profile, see [66]) were investigated for small detuning and the spatial distributions were simulated using the exact force solution of the Optical Bloch Equations (OBE).

1.2.1 Channelling

The motion of atoms in a standing wave is governed mainly by the velocity dependent dipole force which is proportional to the laser-intensity gradient, the spontaneous emission force and momentum diffusion[19, 22, 40]. For atoms which interact with the standing wave at right angles, the standing wave acts like a periodic array of potential valleys parallel to the atomic beam. When the atomic transverse kinetic energy is lower than the potential energy of the standing wave, the atoms will be channelled into these valleys. Because of the short transit time of the atoms through the standing wave, both spontaneous emission and momentum diffusion do not drastically affect the channelling[28].

The gradient or dipole force mentioned above acting on an atom in a standing wave field can be determined from the derivation of a potential

$$F_g = -\frac{\partial U_g}{\partial z} \quad (1.1)$$

The related potential takes the form (the details of the calculation will be given in Chapter 2)

$$U_g = \frac{\hbar\Omega}{2} \cdot \ln\left(1 + \frac{G}{1 + 4\Omega^2/\Gamma^2}\right) \quad (1.2)$$

where Ω is the detuning of the laser beam. For a monochromatic standing wave, $G = 4G_0 \cos^2(kz)$ and G_0 is the transition saturation parameter of atoms.

For positive detunings ($\Omega > 0$), the potential wells coincide with the standing wave nodes and for negative detunings ($\Omega < 0$) with its antinodes. The maximum

potential U_g^0 is located at the antinode of the standing wave for positive detuning. The atoms in this potential are divided into two groups according to their total energy $W = U(z) + mv_t^2/2$, where $U(z)$ is the local potential energy in the standing wave and v_t is the transverse velocity of atoms. The transverse motion of atoms with total energy less than U_g^0 is confined between the adjacent maxima of the potential and is referred to as channelling. In the general case, channelled atoms exhibit anharmonic oscillations relative to the wells of the potential with amplitude in the transverse direction being less than $\lambda/4$. For atoms with total energy greater than U_g^0 , the presence of a potential is only responsible for the corresponding velocity component being modulated and the atoms will not be limited within the $\lambda/4$ region.

The determination of the maximum channelling velocity can be estimated using the criterion $mv_{tmax}^2/2 \leq U_g^0$ for the case that both friction force and momentum diffusion can be omitted. If the friction force and momentum diffusion are important, the maximum channelling velocity would be either smaller than v_{tmax} for negative detuning or larger than v_{tmax} for positive detuning.

When atoms are interacting with a Gaussian standing wave laser beam, the intensity is not uniform in space. The atoms may get channelled only in some region of the beam depending on the total energy. Because of the oscillations related to the wells of the potential, the output direction of atoms from the standing wave field may not keep the same as the input direction. Some atoms will keep their original direction and some will emerge in the other directions. If there is no energy loss for the atoms interacting with the standing wave (conservative potential), the amplitude of the output transverse velocity is equal to the input transverse velocity in which case the output transverse velocity of atoms have only two possible directions: $v_e (= v_{in})$ and $-v_e$, where v_e is the output transverse velocity of atoms. Here the effect on the longitudinal velocity is ignored (this is a good approximation for short interaction time). Those atoms scattered in opposite direction will be reflected back and focused towards the atomic beam axis. Next, a brief review of the focusing of atoms will be presented.

1.2.2 Laser Focusing of Atomic Beam

One of the significant applications of forces exerted on the atoms by the laser light field is to focus an atomic beam. It has been suggested, and in some way

demonstrated[48, 49, 50], that an atomic beam can be focused using the forces exerted on the atoms by the laser light. The ability to focus an atomic beam provides a number of interesting applications, including atomic microscopy, microfabrication, and precise control of atomic beams for precision measurements. In case of positive detuning, the dipole force (see Eq.2.81) on the atoms is from the region of higher laser intensity towards lower laser intensity. The opposite is true for negative detuning, i.e., the force is toward higher intensity.

In 1978, Bjorkholm et al.[48] demonstrated that an atomic beam propagating coaxially with a Gaussian (TEM_{00}) laser beam could be focused to about $250\mu m$ making use of the dipole force. Negative detuning was used so that the atoms were attracted to the higher laser intensity in the center of the beam. In a subsequent paper[49], they showed that a spot size of $28\mu m$ could be obtained, and examined the limitations on the ultimate spot size imposed by spontaneous emission process. In 1988, Balykin et al.[50] reported experiments using a lens made up of two counter-propagating, diverging, Gaussian laser beams oriented transversely to the atom beam. They were able to obtain the image of two atomic sources, demonstrating real image formation with a laser-atom lens.

Balykin and Letokhov[51] first analyzed the properties of a laser-beam lens consisting of an atomic beam traveling coaxially through the focus of a TEM_{01} laser beam. With positive detuning, the dipole force is toward the hollow center of the laser beam. This type of lens has the advantage that the atoms go through a relatively low intensity region, so spontaneous emission is kept to a minimum.

Two-dimensional focusing of an atomic beam using perpendicular interaction of two crossed strong standing-wave laser fields for large detuning was observed by T.Esslinger et al.[47]. In the large detuning conditions, the spatial-averaged heating force for negative detuning almost equals zero and only gradient force acts on the atoms(see Chapter 2), and hence there was no energy loss in this situation. From the view of the law of energy conservation, if ignore the longitudinal velocity change (the details will be given later), the magnitude of the output transverse velocity from the standing wave should be the same as that of the input transverse velocity of atoms. This would cause 1 : 1 focusing image of atoms on the atomic beam axis.

For small detunings, the situation changes and the non conservative heating force becomes important. The output velocity will not be the same as the input velocity

any more. For negative detuning, the output velocity will be larger than the input velocity which leads to a smaller and variable focusing length of atoms (zoom-lens). To our knowledge, there is no previous report of the changing of the focusing length of atom lenses by a standing wave laser field. In this thesis, we will present some experimental evidence which shows this zoom-lens property of atoms in a strong standing wave laser field.

1.2.3 Deflection and Doppleron Resonances

One of the clear results of the continued fraction solution of OBE (see Chapter 2) is the Doppleron resonances which is caused by multiphoton interaction of atoms with the standing wave.

Fig.2.2 shows the results of the continued fraction calculations of the velocity-dependent spatial averaged force F_0 on an atom as a function of the atom's velocity. From the figures, there is a critical velocity v_c at which the force changes sign for high intensity. When the velocity of atom is larger than v_c , the force is always negative (positive) for negative (positive) detuning, which means the velocity of atom in this velocity region will be decreased (increased) and the atomic beam will get to be deflected. Besides the deflection, we can see, from the figure, resonances at certain velocities for high intensities of the standing wave. These velocity-tuned multiphoton resonances have been designated "*Doppleron*" resonances[41]. The resonance condition is

$$|kv| = -\Omega/N \quad (1.3)$$

where $N = 1, 3, 5, \dots$. The force due to the one-photon process which is often called Doppler force will be saturated for high intensity and the width (in velocity) is significantly power broadened by the field. Since the N th-order resonance corresponds to a N -photon process, the width of the N th resonance is narrower than the width of the $(N - 1)$ th process. For large N , the width of the resonances in velocity space can be much narrower than the Doppler spread of the natural linewidth. The force due to the N th-order Doppleron process can be N times larger than the saturated Doppler force (N -photon process). However, the force due to the highest-order processes are weaker because of their relative inefficiency (small probability for multi-photon processes).

The first direct experimental observation of the Doppleron resonances was per-

formed by N.P. Bigelow et al.[45] and the standing-wave field was arranged collinear with a sodium atomic beam. Almost at the same time, another group in the Rice University[46] demonstrated the experimental observation of the effects of the Doppleron resonances on the transverse velocity distribution of atoms in an standing wave laser field. On both experiments, only the first few Doppleron resonances were (up to 7th order) observed.

The higher the order of the Doppleron resonance, the narrower the peak which makes it very difficult to observe experimentally. Because of the sharpness of the peak of the high Doppleron resonances, it would be very useful as a tool in atomic physics, for example, for the velocity bunching of atoms.

1.3 Arrangement of This Thesis

This thesis is organized as follows:

In Chapter 2, I present the details of the force calculation for a two-level atom interacting with laser beam in a simple way using the Optical Bloch Equations (OBE). The exact solutions will be given by using the continued fraction method, the same method used by Minogin et al[42].

In Chapter 3, the details of the simulation processes will be described and we will use these processes to simulate the motion of atoms in a strong standing wave laser field.

The details of the experimental arrangement for the investigation of near perpendicular interaction of atoms with a strong standing wave laser field are given in Chapter 4.

The experiments, presented in Chapter 5 of this thesis, study in detail the effect of stimulated light forces on an atomic beam using a strong, perpendicular, standing wave detuned negatively with respect to the atomic transition. This experimental work is similar to and expands on the work done by Aspect et al[66] and Wang et al[70, 71]. In our experiments, we used a velocity sensitive detector to detect the spatial atomic beam profile. The results of the theoretical simulation using the continued fraction solution will be given.

In chapter 6, we will present the experimental evidence of focusing and variable

focal length imaging of an atomic beam in a strong standing wave under small detuning and high laser intensity. This is the first experimental results which show the change of the focusing length of an atomic beam as function of detuning and intensity of the strong standing wave laser field .

The deflection of an atomic beam and the higher order Doppleron resonances will be discussed in Chapter 7. The experimental result for the deflection of atoms will be given. The necessary conditions for observing the higher order Doppleron resonances will be discussed.

Chapter 2

Theory of Light Pressure Forces

In this chapter, the complete Optical Bloch Equations (OBE) for the system of two-level atom shown in fig.2.1 in a standing wave laser field will be solved to calculate

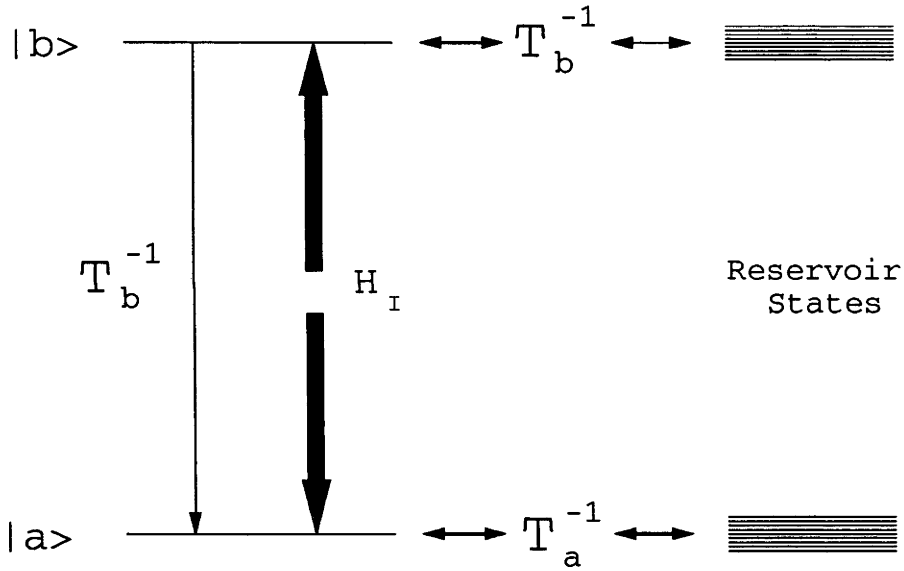


Figure 2.1: *Typical two-level system. The interaction that couples the levels is shown as a thick arrow, while population relaxation processes are shown as a thin arrow. The decay of the upper level of a closed two-level atom repopulates the lower level. In the open two-level system, each level separately reequilibrates with a reservoir of nearby states. In the T_1, T_2 approximation, $T_a = T_b = T_1$.*

the force that an atom experiences using a more direct and more clear way than that in [19]. The motion of an atom in a standing wave field will be treated classically using Newton's second law. This semi-classical method treats the electromagnetic field classically and the atom's internal state as a quantum mechanical system.

2.1 Quantum Mechanical Analogy of Light Pressure Forces

The Heisenberg equation for the operator $\hat{A}(t)$ is given by

$$\frac{d\hat{A}(t)}{dt} = \frac{1}{i\hbar}[\hat{A}(t), \hat{H}] \quad (2.1)$$

from which the Newton's second law of the motion of atoms can be written as

$$\hat{F}(t) = \frac{d\hat{p}}{dt} = \frac{1}{i\hbar}[\hat{p}, \hat{H}] \quad (2.2)$$

where $[\hat{p}, \hat{H}] = \hat{p}\hat{H} - \hat{H}\hat{p}$ is the commutator of the operator of the momentum of the atom \hat{p} and the Hamiltonian \hat{H} describing the atomic states in a light field.

Taking the Hamiltonian as an arbitrary function of the atomic coordinate and momentum, calculation of the commutator leads to the relation (the Ehrenfest Theorem)

$$\hat{F}(t) = -\nabla\hat{H} \quad (2.3)$$

where $\nabla = e_i\frac{\partial}{\partial x} + e_j\frac{\partial}{\partial y} + e_k\frac{\partial}{\partial z}$ and e_i, e_j, e_k are the unit vectors of the x, y and z axis. The ensemble average of the force for the system is

$$F = \langle \hat{F}(t) \rangle = -\langle \nabla\hat{H} \rangle \quad (2.4)$$

where the expectation value is to be calculated with the use of the atomic density matrix. To evaluate the radiation force (Eq.2.4), in the next section, we will present the equations for the atomic density matrix for a two-level system.

2.2 The Density Matrix for a Two-Level System

The simplest quantum-mechanical system consists of an isolated entity with energy eigenstates $|b\rangle$ and $|a\rangle$ having energies ϵ_b and ϵ_a ($\epsilon_b > \epsilon_a$), respectively. If the entity is in the ground state $|a\rangle$, the wave function describing the system is

$$|\psi_a\rangle = e^{-i\epsilon_a t/\hbar}|a\rangle \quad (2.5)$$

and the energy is

$$\langle \psi_a | i\hbar \frac{\partial}{\partial t} | \psi_a \rangle = \epsilon_a \quad (2.6)$$

Similarly, if the entity is known to be in the excited state, the wave function and energy are

$$|\psi_b\rangle = e^{-i\epsilon_b t/\hbar}|b\rangle \quad \text{and} \quad \langle \psi_b | i\hbar \frac{\partial}{\partial t} | \psi_b \rangle = \epsilon_b \quad (2.7)$$

The most general wave function for this system, however, is described by a coherent superposition state

$$|\Psi\rangle = a_\Psi e^{-i\epsilon_a t/\hbar} |a\rangle + b_\Psi e^{-i\epsilon_b t/\hbar} |b\rangle \quad (2.8)$$

where a_Ψ and b_Ψ are real numbers. The wave function in Eq.2.8 describes a system which has probability a_Ψ^2 of being found in the ground state $|a\rangle$ and probability b_Ψ^2 of being in the excited eigenstate $|b\rangle$. All measurable properties of a two-level system in this state can be calculated by taking the expectation value of the operator describing the property.

All measurable properties of the system can be calculated using the density matrix method. In terms of the wave function $|\Psi\rangle$, the density matrix for an isolated system is defined as

$$\rho = |\Psi\rangle\langle\Psi| \quad (2.9)$$

The density matrix for an ensemble obeys the Liouville's equation

$$i\hbar\dot{\rho} = [\hat{H}, \rho] \quad (2.10)$$

and the ensemble averaged expectation value for an operator \hat{A} can be found by using

$$\langle\hat{A}\rangle = Tr(\rho\hat{A}) \quad (2.11)$$

2.3 The Hamiltonian for a Two-Level System Interacting with a Laser Field

The total Hamiltonian for the interaction of atoms with external electromagnetic field has the form

$$\hat{H} = \hat{H}_0 + \hat{H}_I + \hat{H}_R \quad (2.12)$$

where \hat{H}_0 is the Hamiltonian describing the internal states of the isolated two-level system and it specifies the zeroth-order energy eigenstates. \hat{H}_I is the interaction Hamiltonian of atom with the electromagnetic field. The Hamiltonian \hat{H}_R is the operator of relaxation describing all of the processes that return the ensemble to thermal equilibrium. The most important relaxation processes are spontaneous emission and collisions of atoms.

If the states of the two-level system $|a\rangle$ and $|b\rangle$ are coupled by laser field, in the optical frequency range the wavelength $\lambda = 2\pi/k$ is essentially larger than the atomic size a ($ka < 10^{-3}$). This fact enable us to use the dipole approximation for \hat{H}_I . The interaction Hamiltonian that corresponds to the incident wave $E(z, t)$ is

$$\hat{H}_I = -\hat{\mu} \cdot E(z, t) \quad (2.13)$$

where $\hat{\mu}$ is the operator of dipole moment. The matrix element of the dipole moment can be assumed to be real

$$\begin{aligned} \langle b|\hat{\mu}|a\rangle &= \langle a|\hat{\mu}|b\rangle \equiv \mu \\ \langle b|\hat{\mu}|b\rangle &= \langle a|\hat{\mu}|a\rangle = 0 \end{aligned} \quad (2.14)$$

The possibility of such a choice is based on the fact that for a single nondegenerate atomic state, the phase of the corresponding wave function is arbitrary. Therefore for the nondegenerate levels the phase of the atomic wave functions can always be chosen so that the matrix element of the dipole moment is real.

2.4 Relaxation Processes

Because of the complexity of the relaxation phenomena, the relaxation processes are usually dealt with in a quasi-phenomenological manner.

Processes similar to spontaneous emission which cause decay of state $|b\rangle$ to state $|a\rangle$ can be described by the relaxation operator matrix element

$$\begin{aligned} \langle \psi_b|(i\hbar)^{-1}[\hat{H}_R, \rho]|\psi_b\rangle &= (i\hbar)^{-1}[\hat{H}_R, \rho]_{bb} = -\rho_{bb}/T_b \\ \langle \psi_a|(i\hbar)^{-1}[\hat{H}_R, \rho]|\psi_a\rangle &= (i\hbar)^{-1}[\hat{H}_R, \rho]_{aa} = \rho_{bb}/T_b = (1 - \rho_{aa})/T_b \end{aligned} \quad (2.15)$$

The quantity T_b is to be the lifetime of the excited state (see fig.2.1). The lifetime of state $|a\rangle$ is assumed infinite. The third equals sign in (Eq.2.7) results from the conservation of particles condition

$$\rho_{aa} + \rho_{bb} = a_{\Psi}^2 + b_{\Psi}^2 = 1 \quad (2.16)$$

holds when the two-level system is closed.

The off-diagonal elements of the density matrix in this two-level atom approximation also decay toward an equilibrium, but with a different relaxation time,

conventionally called T_2 , the transverse relaxation time. The appropriate matrix elements of the relaxation operator are

$$\begin{aligned}\langle \psi_a | (i\hbar)^{-1} [\hat{H}_R, \rho] | \psi_b \rangle &= (i\hbar)^{-1} [\hat{H}_R, \rho]_{ab} = -\rho_{ab}/T_2 \\ \langle \psi_b | (i\hbar)^{-1} [\hat{H}_R, \rho] | \psi_a \rangle &= (i\hbar)^{-1} [\hat{H}_R, \rho]_{ba} = -\rho_{ba}/T_2\end{aligned}\quad (2.17)$$

The transverse relaxation time T_2 is related to the lifetime of the eigenstates by

$$\frac{1}{T_2} = \frac{1}{2} \left(\frac{1}{T_a} + \frac{1}{T_b} \right) \quad (2.18)$$

T_a is the lifetime of the ground state and is infinite. In the two-level atom approximation $T_2^{-1} = T_a^{-1}/2$

2.5 The Master Equations

The equations of motion for the elements of the density matrix are called the master equations. From the Liouville equation (Eq.2.5), the elements of the density matrix for a two-level system can be calculated as follows:

$$\begin{aligned}\dot{\rho}_{bb} &= \langle \psi_b | \frac{d\rho}{dt} | \psi_b \rangle = \frac{1}{i\hbar} \langle \psi_b | [\hat{H}, \rho] | \psi_b \rangle \\ &= \frac{1}{i\hbar} \{ \langle \psi_b | [\hat{H}_0, \rho] | \psi_b \rangle + \langle \psi_b | [\hat{H}_I, \rho] | \psi_b \rangle + \langle \psi_b | [\hat{H}_R, \rho] | \psi_b \rangle \}\end{aligned}\quad (2.19)$$

The three terms in the Eq.2.19 can be calculated as follows, respectively,

$$\begin{aligned}\langle \psi_b | [\hat{H}_0, \rho] | \psi_b \rangle &= \langle \psi_b | \hat{H}_0 \rho | \psi_b \rangle - \langle \psi_b | \rho \hat{H}_0 | \psi_b \rangle \\ &= \sum_{i=a,b} \{ \langle \psi_b | \hat{H}_0 | \psi_i \rangle \langle \psi_i | \rho | \psi_b \rangle - \langle \psi_b | \rho | \psi_i \rangle \langle \psi_i | \hat{H}_0 | \psi_b \rangle \} \\ &= \langle \psi_b | \hat{H}_0 | \psi_b \rangle \langle \psi_b | \rho | \psi_b \rangle - \langle \psi_b | \rho | \psi_b \rangle \langle \psi_b | \hat{H}_0 | \psi_b \rangle \\ &= \epsilon_b \rho_{bb} - \rho_{bb} \epsilon_b = 0\end{aligned}\quad (2.20)$$

where the sum in the above equation is due to the fact that the two-level system forms a complete base set of the Hilbert space and any vector can be expanded in this Hilbert space.

$$\begin{aligned}\langle \psi_b | [\hat{H}_I, \rho] | \psi_b \rangle &= \langle \psi_b | \hat{H}_I \rho | \psi_b \rangle - \langle \psi_b | \rho \hat{H}_I | \psi_b \rangle \\ &= \sum_{i=a,b} \{ \langle \psi_b | \hat{H}_I | \psi_i \rangle \langle \psi_i | \rho | \psi_b \rangle - \langle \psi_b | \rho | \psi_i \rangle \langle \psi_i | \hat{H}_I | \psi_b \rangle \}\end{aligned}$$

$$\begin{aligned}
&= \langle \psi_b | \hat{H}_I | \psi_a \rangle \langle \psi_a | \rho | \psi_b \rangle - \langle \psi_b | \rho | \psi_a \rangle \langle \psi_a | \hat{H}_I | \psi_b \rangle \\
&= -\mu E(z, t) \rho_{ab} e^{i\omega_0 t} + \mu E(z, t) \rho_{ba} e^{-i\omega_0 t} \\
&= \mu E(z, t) (\rho_{ba} e^{-i\omega_0 t} - \rho_{ab} e^{i\omega_0 t})
\end{aligned} \tag{2.21}$$

here

$$\begin{aligned}
\langle \psi_b | \hat{H}_I | \psi_a \rangle &= e^{i\epsilon_b t/\hbar} \langle b | \hat{H}_I | a \rangle e^{-i\epsilon_a t/\hbar} \\
&= -\mu E(z, t) e^{i\omega_0 t}
\end{aligned} \tag{2.22}$$

where $\omega_0 = (\epsilon_b - \epsilon_a)/\hbar$

From equations Eq.2.15, Eq.2.19, Eq.2.20, Eq.2.21

$$\dot{\rho}_{bb} = \frac{\mu E(z, t)}{i\hbar} (\rho_{ba} e^{-i\omega_0 t} - \rho_{ab} e^{i\omega_0 t}) - \Gamma \rho_{bb} \tag{2.23}$$

where $\Gamma = 1/T_b$ is the transition rate of the upper level.

Before calculating the off-diagonal elements of the density matrix, we first calculate the following term

$$\begin{aligned}
\dot{\rho}_{ba} &= \frac{d}{dt} (\langle \psi_b | \rho | \psi_a \rangle) = \frac{d}{dt} (\langle b | \rho | a \rangle e^{i\omega_0 t}) \\
&= \langle b | \frac{d\rho}{dt} | a \rangle e^{i\omega_0 t} + i\omega_0 \langle b | \rho | a \rangle e^{i\omega_0 t} \\
&= \langle \psi_b | \frac{d\rho}{dt} | \psi_a \rangle + i\omega_0 \langle \psi_b | \rho | \psi_a \rangle
\end{aligned} \tag{2.24}$$

Then the off-diagonal element can be calculated as

$$\begin{aligned}
\dot{\rho}_{ba} &= \langle \psi_b | \frac{d\rho}{dt} | \psi_a \rangle + i\omega_0 \langle \psi_b | \rho | \psi_a \rangle = \frac{1}{i\hbar} \langle \psi_b | [\hat{H}, \rho] | \psi_a \rangle + i\omega_0 \rho_{ba} \\
&= \frac{1}{i\hbar} \{ \langle \psi_b | [\hat{H}_0, \rho] | \psi_a \rangle + \langle \psi_b | [\hat{H}_I, \rho] | \psi_a \rangle + \langle \psi_b | [\hat{H}_R, \rho] | \psi_a \rangle \} + i\omega_0 \rho_{ba}
\end{aligned} \tag{2.25}$$

By the same way as before, the three terms in the above equation can be calculated as

$$\begin{aligned}
\langle \psi_b | [\hat{H}_0, \rho] | \psi_a \rangle &= \langle \psi_b | \hat{H}_0 \rho | \psi_a \rangle - \langle \psi_b | \rho \hat{H}_0 | \psi_a \rangle \\
&= \sum_{i=a,b} \{ \langle \psi_b | \hat{H}_0 | \psi_i \rangle \langle \psi_i | \rho | \psi_a \rangle - \langle \psi_b | \rho | \psi_i \rangle \langle \psi_i | \hat{H}_0 | \psi_a \rangle \} \\
&= \langle \psi_b | \hat{H}_0 | \psi_b \rangle \langle \psi_b | \rho | \psi_a \rangle - \langle \psi_b | \rho | \psi_a \rangle \langle \psi_a | \hat{H}_0 | \psi_a \rangle \\
&= \epsilon_b \rho_{ba} - \rho_{ba} \epsilon_a = (\epsilon_b - \epsilon_a) \rho_{ba} = \hbar \omega_0 \rho_{ba}
\end{aligned} \tag{2.26}$$

$$\begin{aligned}
\langle \psi_b | [\hat{H}_I, \rho] | \psi_a \rangle &= \langle \psi_b | \hat{H}_I \rho | \psi_a \rangle - \langle \psi_b | \rho \hat{H}_I | \psi_a \rangle \\
&= \sum_{i=a,b} \{ \langle \psi_b | \hat{H}_I | \psi_i \rangle \langle \psi_i | \rho | \psi_a \rangle - \langle \psi_b | \rho | \psi_i \rangle \langle \psi_i | \hat{H}_I | \psi_a \rangle \} \\
&= \langle \psi_b | \hat{H}_I | \psi_a \rangle \langle \psi_a | \rho | \psi_a \rangle - \langle \psi_b | \rho | \psi_b \rangle \langle \psi_b | \hat{H}_I | \psi_a \rangle \\
&= -\mu E(z, t) e^{i\omega_0 t} \rho_{aa} - \rho_{bb} (-\mu E(z, t)) e^{i\omega_0 t} \\
&= \mu E(z, t) e^{i\omega_0 t} (\rho_{bb} - \rho_{aa})
\end{aligned} \tag{2.27}$$

combine equations Eq.2.15, Eq.2.24, Eq.2.25, Eq.2.26 and Eq.2.27

$$\dot{\rho}_{ba} = \frac{\mu E(z, t)}{i\hbar} e^{i\omega_0 t} (\rho_{bb} - \rho_{aa}) - \frac{\Gamma}{2} \rho_{ba} \tag{2.28}$$

The master equations will have the form

$$\begin{aligned}
\dot{\rho}_{bb} &= \frac{\mu E(z, t)}{i\hbar} (\rho_{ba} e^{-i\omega_0 t} - \rho_{ab} e^{i\omega_0 t}) - \Gamma \rho_{bb} \\
\dot{\rho}_{ba} &= \frac{i\mu E(z, t)}{i\hbar} e^{i\omega_0 t} (\rho_{bb} - \rho_{aa}) - \frac{\Gamma}{2} \rho_{ba} \\
\rho_{aa} + \rho_{bb} &= 1
\end{aligned} \tag{2.29}$$

From these master equations of the density matrix, we can calculate the elements of the density matrix if the external interaction laser field $E(z, t)$ is given. Usually, the laser fields interacting with atoms are plane traveling wave and standing wave laser. We will use the above master equations to calculate the forces that atoms experience when they traveling in these two fields.

By using the density matrix method, the force in Eq.2.4 has the form

$$\begin{aligned}
F &= -Tr(\nabla \hat{H} \rho) = -Tr(\nabla \hat{H}_I \rho) \\
&= -(\langle \psi_a | \nabla \hat{H}_I \rho | \psi_a \rangle + \langle \psi_b | \nabla \hat{H}_I \rho | \psi_b \rangle) \\
&= -\sum_{i=a,b} (\langle \psi_a | \nabla \hat{H}_I | \psi_i \rangle \langle \psi_i | \rho | \psi_a \rangle + \langle \psi_b | \nabla \hat{H}_I | \psi_i \rangle \langle \psi_i | \rho | \psi_b \rangle) \\
&= -(\langle \psi_a | \nabla \hat{H}_I | \psi_b \rangle \langle \psi_b | \rho | \psi_a \rangle + \langle \psi_b | \nabla \hat{H}_I | \psi_a \rangle \langle \psi_a | \rho | \psi_b \rangle) \\
&= \mu \nabla E(z, t) (e^{-i\omega_0 t} \rho_{ba} + e^{i\omega_0 t} \rho_{ab})
\end{aligned} \tag{2.30}$$

As soon as one knows the matrix element ρ_{ab} and the laser field $E(z, t)$, the exact solution of force acting on the atoms can be calculated by using Eq.2.30.

2.6 Force Acting on Atom Moving in a Plane Traveling Wave and the Doppler Cooling Limit

The linearly polarized plane traveling wave propagating in the positive direction of the z axis ($\vec{k} = k\vec{e}_z$) will take the form

$$E(z, t) = E_0 \cos(kz - \omega t) = \frac{E_0}{2} [e^{i(kz - \omega t)} + e^{-i(kz - \omega t)}] \quad (2.31)$$

where ω is the frequency of the laser field. which gives,

$$\nabla E(z, t) = \frac{ikE_0}{2} [e^{i(kz - \omega t)} - e^{-i(kz - \omega t)}] \quad (2.32)$$

In the Rotating Wave Approximation (RWA), the master equations have the form

$$\begin{aligned} \frac{d\rho_{bb}}{dt} &= \frac{\mu E_0}{2i\hbar} [\rho_{ba} e^{-i(kz - \Omega t)} - \rho_{ab} e^{i(kz - \Omega t)}] - \Gamma \rho_{bb} \\ \frac{d\rho_{ba}}{dt} &= \frac{\mu E_0}{2i\hbar} (\rho_{bb} - \rho_{aa}) e^{i(kz - \Omega t)} - \frac{\Gamma}{2} \rho_{ba} \\ \rho_{aa} + \rho_{bb} &= 1 \end{aligned} \quad (2.33)$$

It is clear from Eq.2.33 that the time dependence of the off-diagonal elements of the density matrix is determined by the exponents $\exp(\pm i\Omega t)$ and the diagonal elements ρ_{bb} and ρ_{aa} are independent of time, it is convenient to use the substitution

$$\rho_{ba} = \rho_{ba}^k e^{i(kz - \Omega t)} \quad (2.34)$$

where ρ_{ba}^k does not depend on the time and velocity of the atom. Thus Eq.2.33 are reduced to a set of algebraic equations

$$\begin{aligned} \frac{\mu E_0}{2\hbar} (\rho_{ab}^k - \rho_{ba}^k) + i\Gamma \rho_{bb} &= 0 \\ \frac{\mu E_0}{2\hbar} (\rho_{aa} - \rho_{bb}) + (\Omega - kv + i\frac{\Gamma}{2}) \rho_{ba}^k &= 0 \\ \rho_{aa} + \rho_{bb} &= 1 \end{aligned} \quad (2.35)$$

where $v = dz/dt$ is the velocity of atom in the direction of z axis.

The nondiagonal density matrix element can be found by solving these equations

$$\rho_{ba}^k = -\frac{\mu E_0}{2\hbar} \cdot \frac{\Omega - kv - i\Gamma/2}{(\Omega - kv)^2 + \Gamma^2/4 + (\mu E_0/\hbar)^2/2} \quad (2.36)$$

From Eq.2.30, the radiation force acting on a two-level atom in the plane traveling wave will be expressed as (using RWA approximation):

$$F = \frac{i\mu k E_0}{2} [e^{i(kz - \omega t)} - e^{-i(kz - \omega t)}] (e^{-i\omega_0 t} \rho_{ba} + e^{i\omega_0 t} \rho_{ab})$$

$$\begin{aligned}
&= \frac{i\mu k E_0}{2} [\rho_{ab} e^{i(kz - \Omega t)} - \rho_{ba} e^{-i(kz - \Omega t)}] \\
&= \frac{i\mu k E_0}{2} (\rho_{ab}^k - \rho_{ba}^k) = \mu k E_0 \text{Im} \rho_{ba}^k \\
&= \frac{\mu^2 E_0^2 k \Gamma}{4\hbar} \cdot \frac{1}{(\Omega - kv)^2 + \Gamma^2/4 + (\mu E_0/\hbar)^2/2} \\
&= \frac{\hbar k \Gamma}{2} \cdot \frac{G}{1 + G + 4(\Omega - kv)^2/\Gamma^2} \\
&= \hbar k R
\end{aligned} \tag{2.37}$$

where R is the photon scattering rate. This equation has the same expression as in the Ref.[52].

This force (often called the radiation-pressure force, scattering force, or spontaneous force) is in the direction of the propagation of light. Note that this force will be saturated with increasing laser intensity and the maximum value of this force is $\hbar k \Gamma/2$. There is no contribution to this average force from the momentum transfer on spontaneous emission because spontaneous emission is random in direction and hence gives a zero average contribution and consequently the atom can be cooled down.

In the case of two weak counterpropagating laser beams with the same intensity (weak standing wave $G \ll 1$), the two waves act independently on the atoms and the average force on the atom is given by

$$F = F_+ + F_- = \frac{\hbar k \Gamma G}{2} \cdot \frac{kv}{\Gamma} \cdot \frac{16\Omega/\Gamma}{1 + 8(\Omega^2 + k^2 v^2)/\Gamma^2 + 16(\Omega^2 - k^2 v^2)^2/\Gamma^4} \tag{2.38}$$

In the small velocity approximation where $|kv| \ll \Gamma$ and $|kv| \ll |\Omega|$, we have

$$F = 2\hbar k G \cdot \frac{kv(2\Omega/\Gamma)}{[1 + 4\Omega^2/\Gamma^2]^2} \tag{2.39}$$

For negative detuning ($\Omega < 0$), this is a friction force, linear in and opposite to velocity v . The atom sees the laser beam opposing its motion Doppler shifted closer to resonance, so it absorbs photons propagating opposite its motion more often than photons propagating along its motion. At the small velocity approximation of $|kv| \ll \Gamma$ and $|kv| \ll |\Omega|$, the force is damping for all velocities for negative detuning. In the case where the detuning is positive, ($\Omega > 0$), the force accelerates the atom. This damping force leads to a rate of kinetic energy loss

$$\left(\frac{dE}{dt}\right)_{cool} = Fv = 4\hbar k^2 G \cdot \frac{2\Omega/\Gamma}{[1 + 4\Omega^2/\Gamma^2]^2} \cdot v^2 = -\alpha v^2 \tag{2.40}$$

As the kinetic energy of the atom is being reduced by the damping force, it is accompanied by a heating process from the random nature of the absorption and emission of photons. Each absorption represents a step of size $\hbar k$ in a random walk of the momentum of the atoms, with equal probability of both positive and negative steps. In the same way, each spontaneous emission represents a random-walk step. In a truly one-dimensional problem the spontaneous emission is along either the positive or negative direction, so that each cycle of absorption followed by spontaneous emission represents two random-walk steps. After a given number of steps, the mean square momentum of the atom grows by the number of steps times the square of the photon momentum $\hbar^2 k^2$.

$$\frac{d(p^2)}{dt} = 2\hbar^2 k^2 R \quad (2.41)$$

The kinetic energy will increase at a rate of

$$\left(\frac{dE}{dt}\right)_{\text{heat}} = \hbar^2 k^2 R / M \quad (2.42)$$

where M is the mass of the atom. The total scattering rate R is the sum of the scattering rates from the positive and negative traveling waves

$$R = \frac{\Gamma}{2} \cdot \frac{G}{1 + G + 4(\Omega + kv)^2/\Gamma^2} + \frac{\Gamma}{2} \cdot \frac{G}{1 + G + 4(\Omega - kv)^2/\Gamma^2} \quad (2.43)$$

With the approximations that $|kv| \ll \Gamma$, $|kv| \ll \Omega$ and $G \ll 1$, one can have

$$\left(\frac{dE}{dt}\right)_{\text{heat}} = \frac{\hbar^2 k^2}{M} \cdot \Gamma \frac{G}{1 + 4\Omega^2/\Gamma^2} \quad (2.44)$$

At equilibrium, the heating and cooling rates are equal, that is

$$\left(\frac{dE}{dt}\right)_{\text{cool}} + \left(\frac{dE}{dt}\right)_{\text{heat}} = 0 \quad (2.45)$$

and from equations Eq.2.40 and Eq.2.44, we can get

$$-4\hbar k^2 G \cdot \frac{(2\Omega/\Gamma)v^2}{[1 + 4\Omega^2/\Gamma^2]^2} + \hbar^2 k^2 \Gamma \cdot \frac{G}{1 + 4\Omega^2/\Gamma^2} = 0 \quad (2.46)$$

so

$$v^2 = \frac{\hbar \Gamma}{4M} \cdot \frac{1 + 4\Omega^2/\Gamma^2}{2|\Omega|/\Gamma} \quad (2.47)$$

As the expressions for the heating and cooling rates are time or ensemble average rates, the Eq.2.47 can be interpreted as giving the mean square velocity of a group

of atoms undergoing laser cooling, or the time average of the squared velocity of a single atom. So we have

$$\frac{k_B T}{2} = \frac{M v_{rms}^2}{2} \quad (2.48)$$

or

$$k_B T = \frac{\hbar \Gamma}{4} \cdot \frac{1 + 4\Omega^2/\Gamma^2}{2|\Omega|/\Gamma} \quad (2.49)$$

This temperature has a minimum value when $2\Omega/\Gamma = -1$, giving

$$k_B T_{min} = \hbar \Gamma / 2 \quad (2.50)$$

This is the so called Doppler-cooling limit. For sodium, it is equal to $240\mu K$, which corresponds to an r.m.s. velocity of $0.3m/s$ in one dimension.

The recoil effect due to the photon absorption or emission at a nonrelativistic atomic velocity can be found using the law of conservation of momentum and the change in the velocity as the atom absorbs or emits a photon at a given wavelength is $v_r = \hbar k/M$. For sodium atoms, the recoil velocity $v_r = 3cm/s$ which is only a tenth of the Doppler-cooling limit velocity.

2.7 Forces Acting On an Atom Moving In A Standing Wave Laser Field

For simplicity's sake, the laser fields forming the standing wave will be considered to be plane and to have the same frequency, amplitude and polarization. Let the counter-propagating wave travel along the $\pm z$ axis, the standing wave has the form

$$\begin{aligned} E(z, t) &= E_0 \cos(kz - \omega t) + E_0 \cos(kz + \omega t) \\ &= 2E_0 \cos(kz) \cos \omega t \\ &= \frac{E_0}{2} (e^{ikz} + e^{-ikz}) (e^{i\omega t} + e^{-i\omega t}) \end{aligned} \quad (2.51)$$

where the amplitudes E_0 of the plane wave are assumed to be real. Then we can get

$$\nabla E(z, t) = \frac{ikE_0}{2} (e^{ikz} - e^{-ikz}) (e^{i\omega t} + e^{-i\omega t}) \quad (2.52)$$

The master equation (Eq.2.33) becomes (using RWA)

$$\dot{\rho}_{bb} = \frac{\mu E_0}{2i\hbar} (e^{ikz} - e^{-ikz}) (e^{i\omega t} + e^{-i\omega t}) (\rho_{ba} e^{-i\omega_0 t} - \rho_{ab} e^{i\omega_0 t}) - \Gamma \rho_{bb}$$

$$\begin{aligned}
&= -i\omega_R[\rho_{ba}e^{i\Omega t} - \rho_{ab}e^{-i\Omega t}] \cos(kz) - \Gamma\rho_{bb} \\
\dot{\rho}_{ba} &= \frac{\mu E_0}{i\hbar} \cos(kz)(e^{i\omega t} + e^{-i\omega t})e^{i\omega_0 t}(\rho_{bb} - \rho_{aa}) - \frac{\Gamma}{2}\rho_{ba} \\
&= -i\omega_R \cos(kz)(\rho_{bb} - \rho_{aa})e^{-i\Omega t} - \frac{\Gamma}{2}\rho_{ba} \\
\rho_{aa} + \rho_{bb} &= 1
\end{aligned} \tag{2.53}$$

By using the following substitution

$$\rho_{ba} = \tilde{\rho}_{ba}e^{-i\Omega t} \tag{2.54}$$

where $\tilde{\rho}_{ba}$ does not depend on time. The explicit time dependence will be eliminated in the equations (Eq.2.53) and they will be expressed in the form

$$\begin{aligned}
\frac{d\rho_{bb}}{dt} &= v \frac{d\rho_{bb}}{dz} = -i\omega_R(\tilde{\rho}_{ba} - \tilde{\rho}_{ab}) \cos(kz) - \Gamma\rho_{bb} \\
\frac{d\tilde{\rho}_{ba}}{dt} &= v \frac{d\tilde{\rho}_{ba}}{dz} = -i\omega_R(\rho_{bb} - \rho_{aa}) \cos(kz) + (i\Omega - \frac{\Gamma}{2})\tilde{\rho}_{ba} \\
\rho_{aa} + \rho_{bb} &= 1
\end{aligned} \tag{2.55}$$

As used by Minogin et al.[19] the solution of the steady-state density matrix Eq.2.55 could be solved in the form of the series

$$\begin{aligned}
\tilde{\rho}_{ba} &= \sum_{n=-\infty}^{+\infty} \rho_{ba}^{nk} e^{inkz} \\
\tilde{\rho}_{\alpha\alpha} &= \sum_{n=-\infty}^{+\infty} \rho_{\alpha\alpha}^{nk} e^{inkz}
\end{aligned} \tag{2.56}$$

To simplify the calculations, it is convenient to introduce the real Blochian variables

$$\begin{aligned}
u &= \rho_{aa} - \rho_{bb} \\
c &= \tilde{\rho}_{ba} + \tilde{\rho}_{ab} = 2\text{Re}\tilde{\rho}_{ba} \\
s &= i(\tilde{\rho}_{ab} - \tilde{\rho}_{ba}) = 2\text{Im}\tilde{\rho}_{ba}
\end{aligned} \tag{2.57}$$

Using the Blochian variable, the series (Eq.2.56) can be rewritten in the form of

$$u = \sum_{n=-\infty}^{+\infty} u_n e^{inkz}, \quad c = \sum_{n=-\infty}^{+\infty} c_n e^{inkz} \quad \text{and} \quad s = \sum_{n=-\infty}^{+\infty} s_n e^{inkz} \tag{2.58}$$

where u_n , c_n and s_n satisfy the usual reality condition

$$u_n^* = u_{-n}, \quad c_n^* = c_{-n} \quad \text{and} \quad s_n^* = s_{-n} \tag{2.59}$$

From equations (Eq.2.57) and $\rho_{aa} + \rho_{bb} = 1$, we have

$$\rho_{aa} = \frac{1+u}{2}$$

$$\begin{aligned}
\rho_{bb} &= \frac{1-u}{2} \\
\tilde{\rho}_{ab} &= \frac{c-is}{2} \\
\tilde{\rho}_{ba} &= \frac{c+is}{2}
\end{aligned} \tag{2.60}$$

By substituting (Eq.2.60), into the first equation of (Eq.2.55), we get

$$\begin{aligned}
-v \cdot \frac{du}{dz} &= 2\omega_R s \cos(kz) - (1-u)\Gamma \\
-v \sum_{n=-\infty}^{+\infty} u_n \text{in} k e^{\text{in} k z} &= \omega_R \sum_{n=-\infty}^{+\infty} [s_n e^{\text{in} k z} \cdot (e^{\text{in} k z} + e^{-\text{in} k z}) + \Gamma [\sum_{n=-\infty}^{+\infty} u_n e^{\text{in} k z} - \delta_{n0} e^{\text{in} k z}]] \\
(\Gamma + \text{in} k v) u_n &= -\omega_R (s_{n-1} + s_{n+1}) + \Gamma \delta_{n0}
\end{aligned} \tag{2.61}$$

The equations of the off-diagonal element of the density matrix, are

$$v \frac{d\tilde{\rho}_{ba}}{dz} = -i\omega_R (\rho_{bb} - \rho_{aa}) \cos(kz) + (i\Omega - \frac{\Gamma}{2}) \tilde{\rho}_{ba} \tag{2.62}$$

$$v \frac{d\tilde{\rho}_{ab}}{dz} = i\omega_R (\rho_{bb} - \rho_{aa}) \cos(kz) + (-i\Omega - \frac{\Gamma}{2}) \tilde{\rho}_{ab} \tag{2.63}$$

Now adding Eq.2.62 and Eq.2.63 gives

$$v \frac{dc}{dz} = -\Omega s - \frac{\Gamma}{2} c \tag{2.64}$$

or

$$(\frac{\Gamma}{2} + \text{in} k v) c_n = -\Omega s_n \tag{2.65}$$

By the same way, the second equation of (Eq.2.55) will have the form

$$v (\frac{dc}{dz} + i \frac{ds}{dz}) = i\omega_R \cdot u (e^{\text{in} k z} + e^{-\text{in} k z}) + (i\Omega - \frac{\Gamma}{2}) (c + is)$$

$$\begin{aligned}
(c_n + is_n) \text{in} k v &= i\omega_R (u_{n-1} + u_{n+1}) + (i\Omega - \frac{\Gamma}{2}) (c_n + is_n) \\
(c_n + is_n) (\text{in} k v - i\Omega + \frac{\Gamma}{2}) &= i\omega_R (u_{n-1} + u_{n+1})
\end{aligned} \tag{2.66}$$

or (using Eq.2.65)

$$(\frac{\Gamma}{2} + \text{in} k v) s_n = \omega_R (u_{n-1} + u_{n+1}) + \Omega c_n \tag{2.67}$$

Then equations (Eq.2.55) can be reduced to an infinite set of recursive algebraic equations

$$\begin{aligned}
(\Gamma + \text{in} k v) u_n &= -\omega_R (s_{n-1} + s_{n+1}) + \Gamma \delta_{n0} \\
(\frac{\Gamma}{2} + \text{in} k v) c_n &= -\Omega s_n \\
(\frac{\Gamma}{2} + \text{in} k v) s_n &= \omega_R (u_{n-1} + u_{n+1}) + \Omega c_n
\end{aligned} \tag{2.68}$$

The radiation force (Eq.2.30) is reduced to (using RWA)

$$\begin{aligned}
F &= \frac{i\mu k E_0}{2} (e^{ikz} - e^{-ikz}) (e^{i\omega t} + e^{-i\omega t}) (\rho_{ba} e^{-i\omega_0 t} + \rho_{ab} e^{i\omega_0 t}) \\
&= \frac{i\mu k E_0}{2} (e^{ikz} - e^{-ikz}) (\rho_{ba} e^{i\Omega t} + \rho_{ab} e^{-i\Omega t}) \\
&= \frac{i\mu k E_0}{2} (e^{ikz} - e^{-ikz}) (\tilde{\rho}_{ba} + \tilde{\rho}_{ab}) \\
&= \frac{i\mu k E_0}{2} (e^{ikz} - e^{-ikz}) c = \frac{i\mu k E_0}{2} (e^{ikz} - e^{-ikz}) \sum_{n=-\infty}^{+\infty} c_n e^{inkz} \\
&= \frac{i\mu k E_0}{2} \left(\sum_{n=-\infty}^{+\infty} c_n e^{i(n+1)kz} - \sum_{n=-\infty}^{+\infty} c_n e^{i(n-1)kz} \right) \\
&= \frac{i\mu k E_0}{2} \left(\sum_{m=-\infty}^{+\infty} c_{2m-1} e^{i2mkz} - \sum_{j=-\infty}^{+\infty} c_{2j+1} e^{i2jkz} \right) \\
&= \frac{ik\hbar\omega_R}{2} \sum_{n=-\infty}^{+\infty} (c_{2n-1} - c_{2n+1}) e^{i2nkz} \\
&= \hbar k \sum_{n=-\infty}^{+\infty} f_{2n} e^{i2nkz} \tag{2.69}
\end{aligned}$$

where

$$f_{2n} = \frac{i\omega_R}{2} (c_{2n-1} - c_{2n+1}) \tag{2.70}$$

and

$$\begin{aligned}
f_{-2n} &= \frac{i\omega_R}{2} (c_{-2n-1} - c_{-2n+1}) \\
&= \frac{i\omega_R}{2} (c_{2n+1}^* - c_{2n-1}^*) = f_{2n}^* \tag{2.71}
\end{aligned}$$

Then

$$\begin{aligned}
F &= \hbar k [f_0 + \sum_{n=1}^{+\infty} f_{2n} e^{i2nkz} + \sum_{n=-1}^{-\infty} f_{2n} e^{i2nkz}] \\
F &= \hbar k [f_0 + \sum_{n=1}^{\infty} (f_{2n} e^{i2nkz} + f_{-2n} e^{-i2nkz})] \\
&= \hbar k \{ f_0 + \sum_{n=1}^{\infty} [(f_{2n} + f_{2n}^*) \cos(2nkz) + i(f_{2n} - f_{2n}^*) \sin(2nkz)] \} \\
&= F_0 + \sum_{n=1}^{\infty} [F_{2nc} \cos(2nkz) + F_{2ns} \sin(2nkz)] \tag{2.72}
\end{aligned}$$

where

$$F_0 = \hbar k f_0 = \frac{i\hbar k \omega_R}{2} (c_{-1} - c_1) = \hbar k \omega_R \text{Im} c_1 \tag{2.73}$$

$$\begin{aligned}
F_{2nc} &= \hbar k (f_{2n} + f_{2n}^*) = 2\hbar k \text{Re}(f_{2n}) \\
&= \hbar k \omega_R \text{Im}(c_{2n+1} - c_{2n-1}) \tag{2.74}
\end{aligned}$$

$$\begin{aligned}
 F_{2ns} &= \hbar k i (f_{2n} - f_{2n}^*) = 2\hbar k i \text{Im}(f_{2n}) \\
 &= \hbar k \omega_R \text{Re}(c_{2n+1} - c_{2n-1})
 \end{aligned}
 \tag{2.75}$$

From Ref.[42], the solution of the recursion equations (Eq.2.68) can be obtained in the form of convergent continued fractions which was used by Stenholm and Lamb [43] in the theory of gas lasers.

2.7.1 A Simple Solution of Gradient Force in a Standing Wave Field

In this section, I calculate the density matrix equations for a special condition in which the transverse velocity of the atom is selected as zero. This is an alternative derivation of the gradient force expression calculated by me using OBE.

For zero velocity atoms, the master equations (Eq.2.55) will have the following forms

$$\begin{aligned}
 -i\omega_R(\tilde{\rho}_{ba} - \tilde{\rho}_{ab}) \cos(kz) - \Gamma \rho_{bb} &= 0 \\
 -i\omega_R(\rho_{bb} - \rho_{aa}) \cos(kz) + (i\Omega - \frac{\Gamma}{2})\tilde{\rho}_{ba} &= 0 \\
 \rho_{aa} + \rho_{bb} &= 1
 \end{aligned}
 \tag{2.76}$$

To simplify the calculation, here we introduce the substitutions $\tilde{\rho}_{ba} = x + iy$ and $\tilde{\rho}_{ab} = x - iy$. From the first equation of Eq.2.76, we have

$$\rho_{bb} = \frac{2y\omega_R}{\Gamma} \cos(kz)
 \tag{2.77}$$

From the second equation of Eq.2.76

$$-i\omega_R(2\rho_{bb} - 1) \cos(kz) + (i\Omega - \frac{\Gamma}{2})(x + iy) = 0
 \tag{2.78}$$

From Eq.2.77 and Eq.2.78, x and y can be expressed as

$$x = -\frac{2\Omega}{\Gamma} y
 \tag{2.79}$$

$$y = \frac{\sqrt{2G_0} \cos(kz)}{1 + 4\Omega^2/\Gamma^2 + 4G_0 \cos^2(kz)}
 \tag{2.80}$$

where $G_0 = 2\omega_R^2/\Gamma^2 = 2\mu^2 E_0^2/\hbar^2 \Gamma^2$ is the saturation parameter of the single traveling laser field.

The force has the form, according to Eq.2.69,

$$F = \frac{i\mu k E_0}{2} (e^{ikz} - e^{-ikz})(\tilde{\rho}_{ba} + \tilde{\rho}_{ab}) = -\mu k E_0 \sin(kz) 2x$$

$$\begin{aligned}
&= \frac{4\mu k E_0 \Omega}{\Gamma} \cdot \frac{\sqrt{2G_0} \sin(kz) \cos(kz)}{1 + 4\Omega^2/\Gamma^2 + 4G_0 \cos^2(kz)} \\
&= \frac{2\hbar k \Omega G_0}{1 + 4\Omega^2/\Gamma^2 + 4G_0 \cos^2(kz)} \sin(2kz) \\
&= -\frac{dU(z)}{dz}
\end{aligned} \tag{2.81}$$

where $U(z)$ is the potential related to the gradient or dipole force and takes the form

$$U(z) = \frac{\hbar \Omega}{2} \cdot \ln \left[1 + \frac{4G_0 \cos^2(kz)}{1 + 4\Omega^2/\Gamma^2} \right] \tag{2.82}$$

which has the same expression as in Ref.[62, 64]. From the formula it follows that the potential period is equal to one half of the wavelength. And, at a positive detuning ($\Omega > 0$), the potential wells coincide with the light wave nodes and at a negative detuning ($\Omega < 0$) with its antinodes.

2.7.2 Continued Fraction Solution of Forces

In order to calculate the forces, the first step needed is the determination of the coefficients c_n . Following the same procedure as Minogin et al.[19], from the recursion equations (Eq.2.68), u_n is nonzero for even n and s_n is nonzero for odd n . It is convenient to introduce a common notation x_n for the quantities u_n and s_n :

$$x_n = \begin{cases} u_n & \text{for even } n \\ s_n & \text{for odd } n \end{cases}$$

Then from Eq.2.68, the first and third can be written in the form of a single recursion equation

$$x_n - D_n(x_{n-1} + x_{n+1}) = \delta_{n0} \tag{2.83}$$

where the coefficients D_n are

$$D_n = \begin{cases} -\frac{\omega_R}{\Gamma + inkv} & \text{for even } n \\ \frac{\omega_R(\Gamma/2 + inkv)}{(\Gamma/2 + inkv)^2 + \Omega^2} & \text{for odd } n \end{cases}$$

Because of the reality condition (Eq.2.59),

$$x_{-n} = x_n^* \tag{2.84}$$

For $n \geq 0$, the connection between the successive unknown quantities x_n and x_{n+1} can be written in the form

$$x_{n+1} = q_n x_n \quad (2.85)$$

Substituting Eq.2.85 into Eq.2.83 gives the following recursion relation

$$q_{n-1} = \frac{D_n}{1 - D_n q_n} \quad (2.86)$$

then the quantity q_0 can be expressed as an infinite fraction

$$q_0 = D_1 / (1 + p_1 / (1 + p_2 / (1 + p_3 / (1 + \cdots)))) \quad (2.87)$$

Here the numerators are

$$p_n = -D_n D_{n-1} = G \cdot \frac{\Gamma/2 + in_1 kv}{\Gamma + in_2 kv} \cdot \frac{\Gamma^2/2}{(\Gamma/2 + in_1 kv)^2 + \Omega^2} \quad (2.88)$$

where $n_1 = \begin{cases} n+1 \\ n \end{cases}$ and $n_2 = \begin{cases} n & \text{for even } n \\ n+1 & \text{for odd } n \end{cases}$

When $n = 0$, from Eq.2.83 and $x_1 = q_0 x_0$, $u_0 = x_0$ has the form

$$x_0 + 2\omega_R \text{Re} x_1 / \Gamma = x_0 (1 + 2\text{Re} Q) = 1 \quad (2.89)$$

The solution of Eq.2.89 is determined by the formula

$$x_0 = u_0 = \frac{1}{1 + 2\text{Re} Q} \quad (2.90)$$

where Q is an infinite convergent fraction

$$Q = p_0 / (1 + p_1 / (1 + p_2 / (1 + p_3 / (1 + \cdots)))) \quad (2.91)$$

All other values $x_n = u_n (n = \pm 2, \pm 4, \cdots)$ and $x_n = s_n (n = \pm 1, \pm 3, \cdots)$ can be obtained from the recursion relation (Eq.2.85) and the reality condition (Eq.2.84).

For an arbitrary atomic velocity it is impossible to get an analytical expression for the force. It is possible to use the continued fraction expansion method mentioned above to get a numerical estimation of the force. Some examples of the force calculations as function of velocity of an atom are plotted in fig.2.2. At low intensity (fig.2.2A: $\Omega = -75 \text{ MHz}$ and $G = 2$), the force is nearly equal to the sum of the radiation pressure forces of the two counterpropagating waves. It is never a heating force for such a negative detuning and small intensity. When the intensity increases, this conclusion is reversed, at least for small velocities, as it can be seen in fig.2.2B

to fig.2.2D, plotted for increasing detunings Ω and intensities G . When the Rabi frequency $\omega_R = \mu E/\hbar = \Gamma\sqrt{G/2}$ and detuning Ω are large compared to the natural linewidth Γ , the curves have the following characteristics:

- (a). For low velocities ($v \ll 2m/s$), the force varies linearly with the velocity.
- (b). The force is maximum for $v \sim 2m/s$ and can be much higher than the maximal spontaneous emission force $\hbar k\Gamma/2$. For example in fig.2.2D, for $G = 5000$ and $\Omega = -240MHz$, the maximal force is about $6 \times (\hbar k\Gamma/2)$.
- (c). The force then decreases as $1/v$ until v reaches a critical value v_c , whose value increases with Ω and G .
- (d). When velocity is larger than the critical velocity v_c , resonances appear as Doppleron Resonances[41] and the sign of the force changes: it becomes a cooling force for negative detuning $\Omega < 0$ and an accelerating one for positive detuning $\Omega > 0$.

In the next chapters, we will investigate most of these force characteristics both in experiments and simulations.

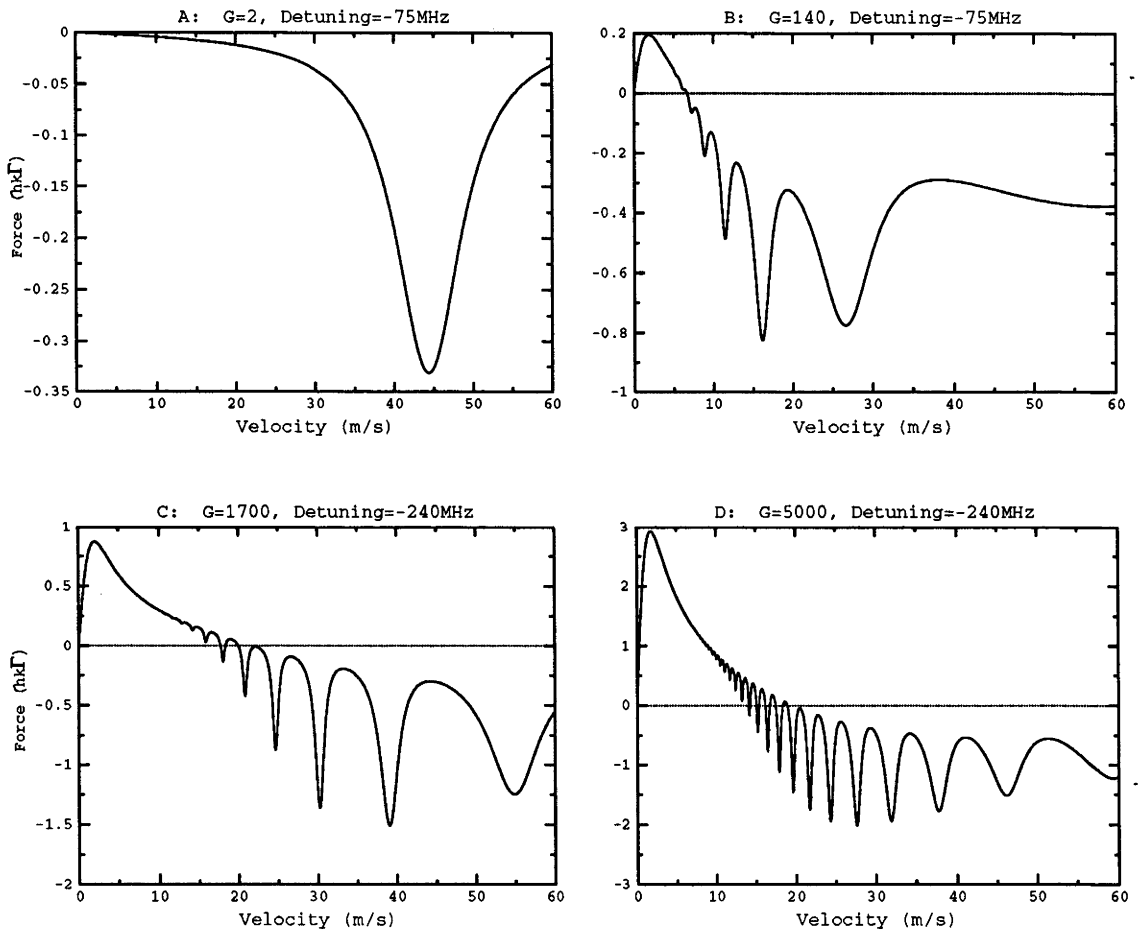


Figure 2.2: Variations of the spatial averaged force F_0 acting on an atom in a standing wave as a function of the atomic velocity. These curves have been calculated for increasing detunings Ω and saturation parameters G .

Chapter 3

Numerical Simulation

Various theoretical methods have been developed to describe the evolution of atomic motion for long interaction time $t \gg \tau$ ($= \Gamma^{-1}$). One of the first of these methods used the Fokker-Planck equation (FPE) for the Wigner distribution[12] which treats the motion of the atom classically and, hence it is not valid for $p \sim \hbar k$ (photon momentum). A dressed-state approach developed by Dalibard et al. is a fully-quantum-mechanical theory and can give a clear physical picture of “Sisyphus” cooling for atoms with small velocity[67]. Unfortunately, this approach can not give an exact numerical solution of the force for the high laser intensity ($\omega_R \gg \Gamma$) and small laser detuning ($\Omega \ll \omega_R$) regime.

In this chapter, we will use the continued fraction solution which is the exact force solution of the Optical Bloch Equations (OBE) to simulate the motion of the atoms moving in a standing wave field. The continued fraction solution of the OBE is valid for all interaction parameters (including small detuning and high intensity) of the standing wave. If we consider conditions where diffusion is not important, e.g. for large detuning $\Omega \gg \Gamma$, this method is a good approximation to simulate the motion of atoms in an strong standing wave laser field. The atomic beam in the following simulation is set to be near perpendicular to the standing wave laser field (see fig.4.2).

3.1 Velocity-Dependent Forces And Doppleron Resonance Structure

In order to determine the interaction of the atomic beam with the standing wave field, we have to calculate the velocity dependent forces (Eq.2.72) as a function

of the variable parameters in the experiment: laser intensity I , detuning Ω (in the rest frame of the atom) and transverse velocity v_t of atoms. This requires the evaluation of the Fourier coefficients using the continued fraction technique outlined by Minogin and Serimaa [42]. (see Chapter 2)

The Fourier coefficients for the zeroth and first order ($n = 1$) terms are shown in fig.3.1 as a function of transverse velocity. The intensity is quoted throughout using the single traveling wave saturation parameter $G [= G_{local}(z = 0)/4]$, and in fig.3.1 is chosen to be in the mid-range of the intensities present in the standing wave ($G_0 = 70$) in one of our experiments. The detuning $\Omega/2\pi = -75 MHz$ corresponds to the detuning used in the same experiment.

The zeroth order term F_0 represents the spatially averaged force and therefore has no z dependence, while the first order ($n = 1$) sine and cosine terms reflect the fundamental periodicity of the standing wave potential. Fig.3.1b and fig.3.1c show the higher order coefficients ($n = 2 - 5$) which contribute to the specific shape of each periodic potential well: the sine harmonic (fig.3.1b) and the cosine harmonic (fig.3.1c).

The obvious undulations in (fig.3.1) are the multi-photon or Doppleron resonances [44, 45, 46]. The Doppleron Resonances can be understood using a simple physical picture (see fig.3.2). The resonances results from processes in which an atom absorbs $n + 1$ photons from one traveling wave and is stimulated to reemit n photons into the oppositely directed traveling wave. The final photon is spontaneously emitted. For negative detuning ($\Omega < 0$), the atom absorbs the $n + 1$ photons from the counterpropagating traveling wave which has the detuning $\Omega + |kv|$ in the atom's rest frame. Similarly, the copropagating field will have the frequency $\Omega - |kv|$ in the same rest frame. In accordance with the energy conservation law written in the rest frame of an atom

$$\hbar(\omega + |kv|)(n + 1) - \hbar(\omega - |kv|)n = \omega_0 \quad (3.1)$$

Then the resonance condition is

$$|kv| = -\frac{\Omega}{2n + 1} \quad (3.2)$$

The true position of the Doppleron peaks deviates from Eq.3.2 for high laser intensities ($I \gg I_{sat}$). This discrepancy arises primarily because of the Stark shift associated with the laser field itself. If I is increased, the Stark shift will increase,

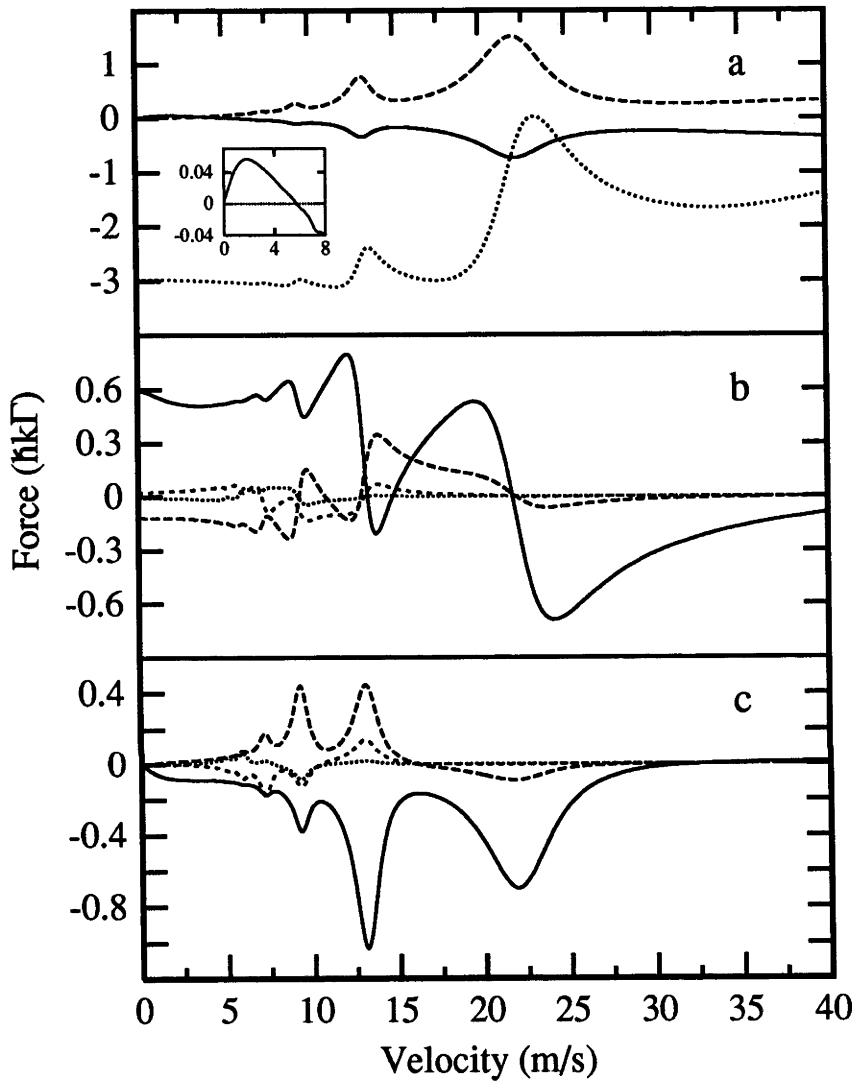


Figure 3.1: Fourier coefficients for the velocity dependent dipole force as a function of transverse velocity for a saturation parameter $G = 70$ and detuning $\Omega/2\pi = -75\text{MHz}$: (a) zero order term F_0 (solid), and first order coefficients F_1^c (dashed) and F_1^s (dotted). Inset: F_0 with magnified force scale; (b) sine coefficients $n = 2$ (solid), 3 (dashed), 4 (small dashed) and 5 (dotted); (c) cosine coefficients $n = 2 - 5$ as for (b). Note that the interested transverse velocity in our experiments was $v_t < 5\text{m/s}$.

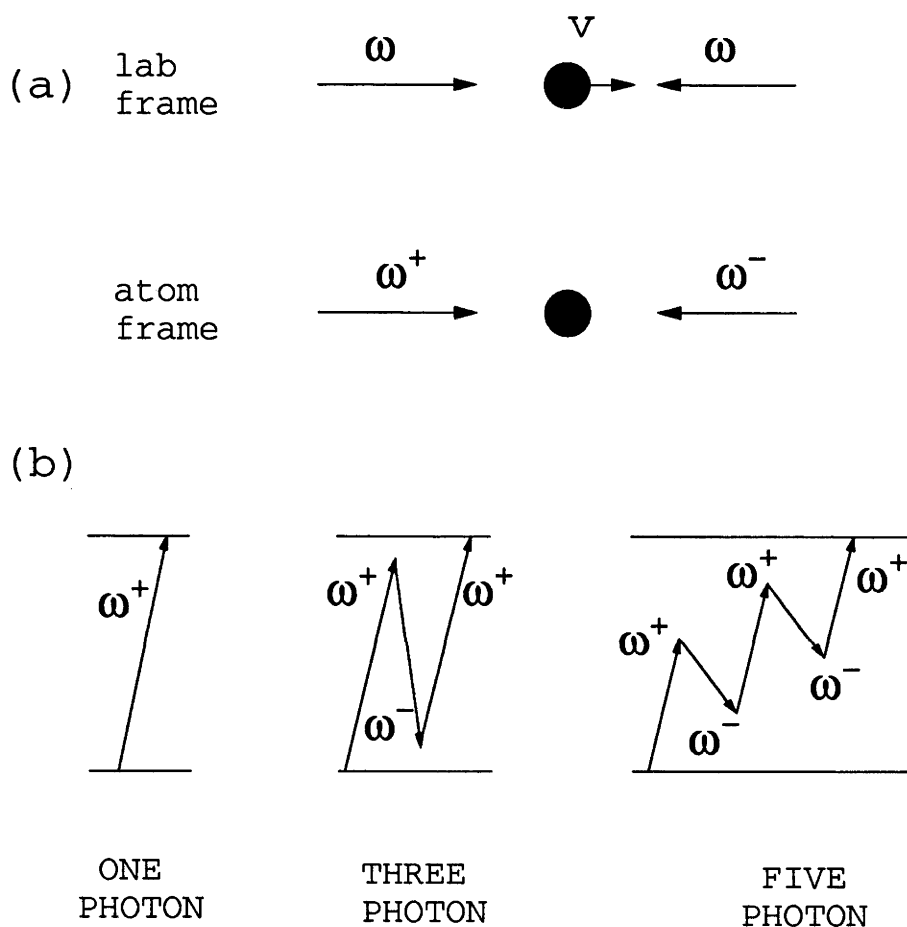


Figure 3.2: (a) An atom travels at velocity v in the laboratory frame in the presence of counterpropagating, equal-frequency traveling waves. In transforming to the frame of the atom, the frequencies of the traveling waves acquire equal, but opposite Doppler shifts: $\omega_{\pm} = \omega \pm kv$. (b) Assume that ω is below the resonant frequency of the atom by an amount δ . A one-photon transition will be resonant for $|\Omega| = kv$. Similarly, multiphoton stimulated Raman transitions involving the absorption and stimulated emission of photons from both traveling waves will be resonant for certain velocities. The resonance conditions are $|\Omega| = (2n + 1)kv$, where n is integer. These are the velocity-tuned Doppleron resonances.

and the positions of the Doppleron resonances will move to a higher velocity region, and at the same time, the peaks are power broadened.

One of the important consequences of the force solution is the change of the sign of the light force for small velocities when the laser intensity increases. For negative detuning ($\Omega < 0$), the sign of the force near zero velocity for high laser intensity is opposite to the sign of the force for low intensity. This can be seen from (fig.3.1), the F_0 term is positive for low transverse velocities ($v_t < 6m/s$) i.e. a heating force, but changes sign at higher transverse velocities to become a damping force. If the diffusion processes are not taken into account and the intensity of the standing wave is uniform in space, we can expect, from the force diagram, the accumulation of atoms at a critical velocity v_c where the force is zero. For a different intensity of the standing wave, the position of the critical velocity v_c changes. In the actual Gaussian laser standing wave beam, the electric field is not uniform and the critical velocity v_c will change over a small region and the atoms will accumulate in this small region.

As shown in fig.3.1, F_0 is primarily responsible for heating of the atoms at small negative detunings.

In our experimental conditions of an atomic beam perpendicularly interacting with a strong standing wave, in order to get a maximum SNR (Signal to Noise Ratio) and to stay with the limit of the oven heating system, the temperature of the oven is set to be $500 \pm 20^\circ C$ which corresponding to a most probable velocity of $1000m/s$. A $1mm$ diameter skimmer just in front of the standing wave field allowed a maximum divergence angle (half width) of $(0.35 + 1.0) \times 0.5/720.0 = 0.95mrad$, where $0.35mm$ is the diameter of the oven nozzle and $720mm$ is the distance between the oven nozzle and the standing wave field. The peak of the transverse velocity distribution is around $1.0m/s$, and hence the region of interest is $v_t < 5m/s$.

Although the continued fraction methods can provide an exact solution for the atoms traveling in a standing wave laser beam, unfortunately, they do not give any physical picture for these sign change features that appear in the small velocity regime at high intensities. In 1985, by using the dressed-atom approach that has already been applied with success to the physical interpretation of resonance fluorescence in the high-intensity limit[56, 57, 58], a physical picture was proposed to interpret this phenomenon[59]. In the next section, we will outline the basic points of this dressed state picture developed by J.Dalibard and C.Cohen-Tannoudji.[59].

3.2 Physical Interpretation of The Heating Effect By Using Dressed-State Approach

The heating effect can be explained by using the dressed-state method described in [66]. When the Rabi frequency $\omega_R = \mu E/\hbar$ characterizing the strength of the laser-atom interaction is large enough compared with the spontaneous rate, it is a good approximation to consider the energy levels of the combined system: atom and laser photons interacting together (dressed states). In an inhomogeneous laser beam, the Rabi frequency ω_R then varies in space, since it is proportional to the position-dependent laser amplitude. The dressed-atom Hamiltonian at a fixed point \vec{r} , $\hat{H}_{DA}(\vec{r})$ is the sum of the atomic internal energy, the laser mode energy and the atom-laser mode coupling

$$\hat{H}_{DA}(\vec{r}) = \hbar\omega_0 b^\dagger b + \hbar\omega a^\dagger a - [\hat{\mu} \cdot \epsilon(\vec{r}) b^\dagger a + \hat{\mu} \cdot \epsilon^*(\vec{r}) b a^\dagger] \quad (3.3)$$

If there is no interaction between the laser field and atom ($\hat{\mu} = 0$ or laser beam was turned off), the dressed-state eigenenergy can be written as

- (a). $n + 1$ [photons in the laser mode and the atoms are in the ground states g

$$E_{DE}^g = (n + 1 + \frac{1}{2})\hbar\omega - \frac{1}{2}\hbar\omega_0 \quad (3.4)$$

where $\frac{1}{2}\hbar\omega$ represents the vacuum energy.

- (b). n photons in the laser mode and the atoms are in the excited state e

$$E_{DE}^e = (n + \frac{1}{2})\hbar\omega + \frac{1}{2}\hbar\omega_0 \quad (3.5)$$

From the definition of the detuning $\Omega = \omega - \omega_0$, Eq.3.4 and Eq.3.5 have the forms:

$$\begin{aligned} E_{DE}^g &= (n + 1 + \frac{1}{2})\hbar\omega - \frac{1}{2}\hbar(\omega - \Omega) = (n + 1)\hbar\omega + \frac{1}{2}\hbar\Omega \\ E_{DE}^e &= (n + \frac{1}{2})\hbar\omega + \frac{1}{2}\hbar(\omega - \Omega) = (n + 1)\hbar\omega - \frac{1}{2}\hbar\Omega \end{aligned} \quad (3.6)$$

when the atom-laser interaction is taken into account, because of the Stark effect, at different position in space, there is different energy displacement for both ground and excited states of atoms. The new eigenenergies for E_{DE}^g and E_{DE}^e are

$$\begin{aligned} E_{DE}^g &= (n + 1)\hbar\omega + \frac{1}{2}\hbar\Omega \pm \frac{\hbar\omega_{GR}}{2} \\ E_{DE}^e &= (n + 1)\hbar\omega - \frac{1}{2}\hbar\Omega \mp \frac{\hbar\omega_{GR}}{2} \end{aligned} \quad (3.7)$$

with $\omega_{GR} = \sqrt{\omega_R^2 + \Omega^2}$, the generalized Rabi frequency; Plus refers to positive detuning and minus refers to negative detuning.

In fig.3.3, the variation of the energy levels across a standing wave laser beam are represented for positive detuning: at the node of the standing wave ($\omega_R = 0$), the dressed levels coincide with Eqs.3.6 and their splitting between $E_{DE}^g(\vec{r})$ and $E_{DE}^e(\vec{r})$ is just $\hbar\Omega$. At the antinode of the standing wave, the splitting between the two dressed levels is now $\hbar\Omega_{GR}$, larger than $\hbar\Omega$ and reaches maximum at the antinodes of the standing wave. In fact, the splitting of the dressed energy level is caused by the AC stark effect. When the atoms are in the antinode of the standing wave, the intensity of the field is maximum, that means, the probability of atoms in the excited level with n photons in laser field is maximum. As the atoms move in the standing wave away from an antinode, the intensity decreases. If we follow the “trajectory” of the moving atoms starting, for example, at an antinode of the standing wave in level $|e, n\rangle$ (see fig.3.3), the atoms go uphill until they reach the top (node) where their decay rate is maximum (intensity of the standing wave laser is zero). Once the atoms have decayed they have the largest probability to stay in the dressed-state $|g, n+1\rangle$ (ground state with $n+1$ photons in the laser field), in which case the atoms are again in the valley. It has now to go uphill again until they reach a new top (node) where $|g, n+1\rangle$ is most unstable and so on. It is clear that the atoms always move uphill and get cooled by the positive detuning field. When the detuning is negative, the process is opposite and the atoms always move downhill and get heated.

3.3 Approximation of Simple Gradient Force

From the previous chapter, we found that there is no simple analytical solution for the OBE and the simple gradient force is only a special solution for $v_t = 0$. In this section, we will examine the possibility to use the approximation in which the total force may be expected to be the sum of F_0 and the gradient force in small velocity regime, the latter being independent of velocity.

In (fig.3.1) it should be noted that the Doppler shift velocity corresponding to the sodium natural linewidth ($10MHz$) is $5.9m/s$, and hence the inequality $kv_t \ll \Gamma$ holds in the region of interest in the experiments for which an atomic beam is perpendicular to the standing wave. Fig.3.1 indicates that the net contribution of the higher order terms ($n \geq 1$) changes relatively slowly with transverse velocity in this regime. This supports the hypothesis that for $kv_t \ll \Gamma$, the summation of the higher order forces in Eq.2.72 may be identified with the velocity independent

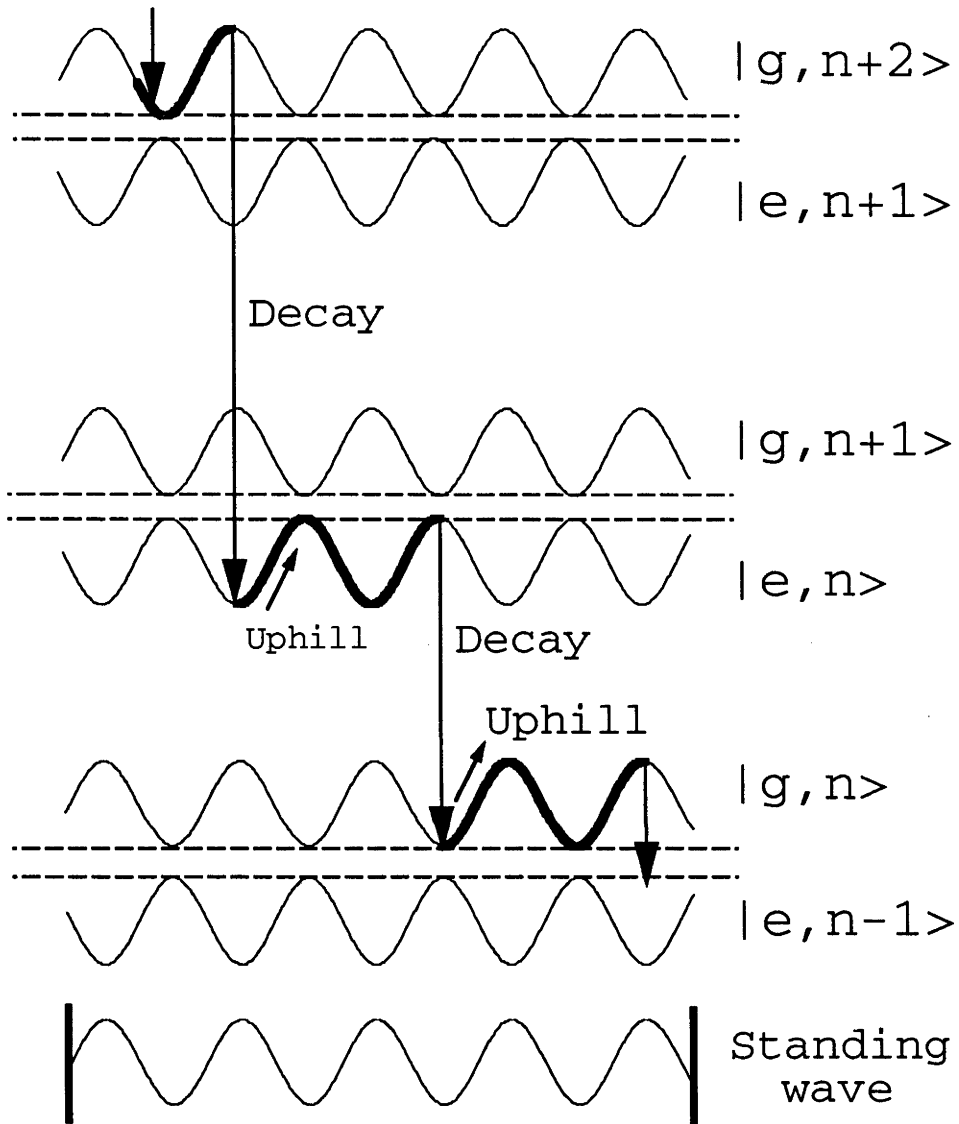


Figure 3.3: Changing of the dressed-state in a strong standing wave laser field. The thin solid lines represent the spatial variations of the dressed-state energy levels. The thick solid lines represent the “trajectory” of a slowly moving atom. Because of the spatial variation of the dressed-state levels, for positive detuning, the atoms have the largest probability in the ground dressed state (for example $|g, n+2\rangle$) at node and in the excited dressed state (for example $|e, n\rangle$) at an antinode. Between two spontaneous emissions, the atoms see, on the average, more uphill parts than downhill ones and are therefore slowed down. For positive detuning, the situation is just opposite and the atoms get heated.

gradient force in Eq.2.81 i.e.

$$\begin{aligned} F - F_0 &= \sum_{n=1}^{\infty} [F_n^c \cos(2nkz) + F_n^s \sin(2nkz)] \\ &\sim -dU(z)/dz \end{aligned} \quad (3.8)$$

To illustrate this, the sum of the higher order force terms is compared with the gradient force in (fig.3.4) over the regime of our experiments ($kv_t \ll \Gamma$). From the force figure (fig.3.1), it is clear that the sine and cosine force coefficients decrease very quickly when n increases. The force terms are ignorable when n is larger than 5. Here we selected n up to 20 to increase the accuracy of the force. Shown is the sum of the $n = 1 \sim 20$ sine and cosine force terms in the Fourier expansion for $\Omega/2\pi = 75\text{MHz}$ as a function of the spatial position (z) over one standing wave period, for 5 transverse velocities. (Note, however, that the transverse velocity is assumed constant i.e. independent of z , over each period). Also shown is the gradient force calculated for the same standing wave period. As can be seen from fig.3.4, the sum of the Fourier components (which determine the potential well shape) closely approximates the result for the gradient force, particularly for the lower transverse velocities. However, we show later that despite the similarity of these two models for the light force, the effect on the predicted far field spatial atomic beam profile can be significantly different.

To emphasize the importance of the spatially invariant heating term at these detunings, the potential corresponding to the continued fraction solution is shown as a function of z in fig.3.5 with and without the heating component F_0 (assuming a constant 1.0m/s transverse velocity). It is clear that the heating contribution becomes significant compared to the spatially varying potential once atoms have traversed a number of wavelengths.

Examination of fig.3.1 indicates that in the region of interest, the sine force terms dominate the cosine terms, and consequently the spatially varying force component is predominantly a sinusoidal damping force. This is to be expected from Eq.2.81

$$\begin{aligned} F &= 2\hbar k \Omega G_0 \frac{\sin(2kz)}{1 + 4\Omega^2/\Gamma^2 + 4G_0 \cos^2(kz)} \\ &= 2\hbar k \Omega G_0 \frac{\sin(2kz)}{(1 + 4\Omega^2/\Gamma^2 + 2G_0) + 2G_0 \cos(2kz)} \\ &= \frac{2\hbar k \Omega G_0}{1 + 4\Omega^2/\Gamma^2 + 2G_0} \cdot \frac{\sin(2kz)}{1 + 2G_0/(1 + 4\Omega^2/\Gamma^2 + 2G_0) \cos(2kz)} \end{aligned} \quad (3.9)$$

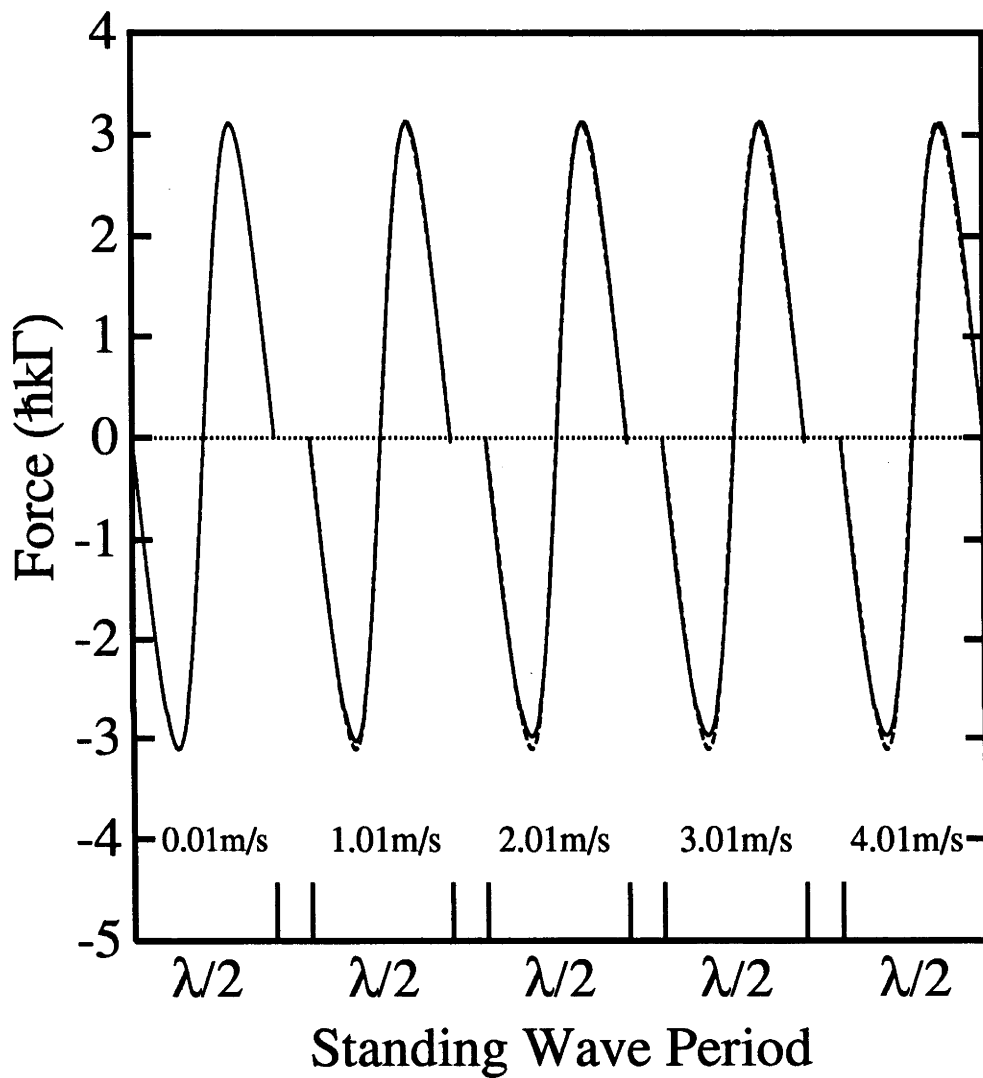


Figure 3.4: Comparison of continued fraction solution ($1 \leq n \leq 20$ —solid curve) with gradient force (dotted curve) as a function of z over one standing wave period for 5 values of transverse velocity. Conditions as for fig.3.1.

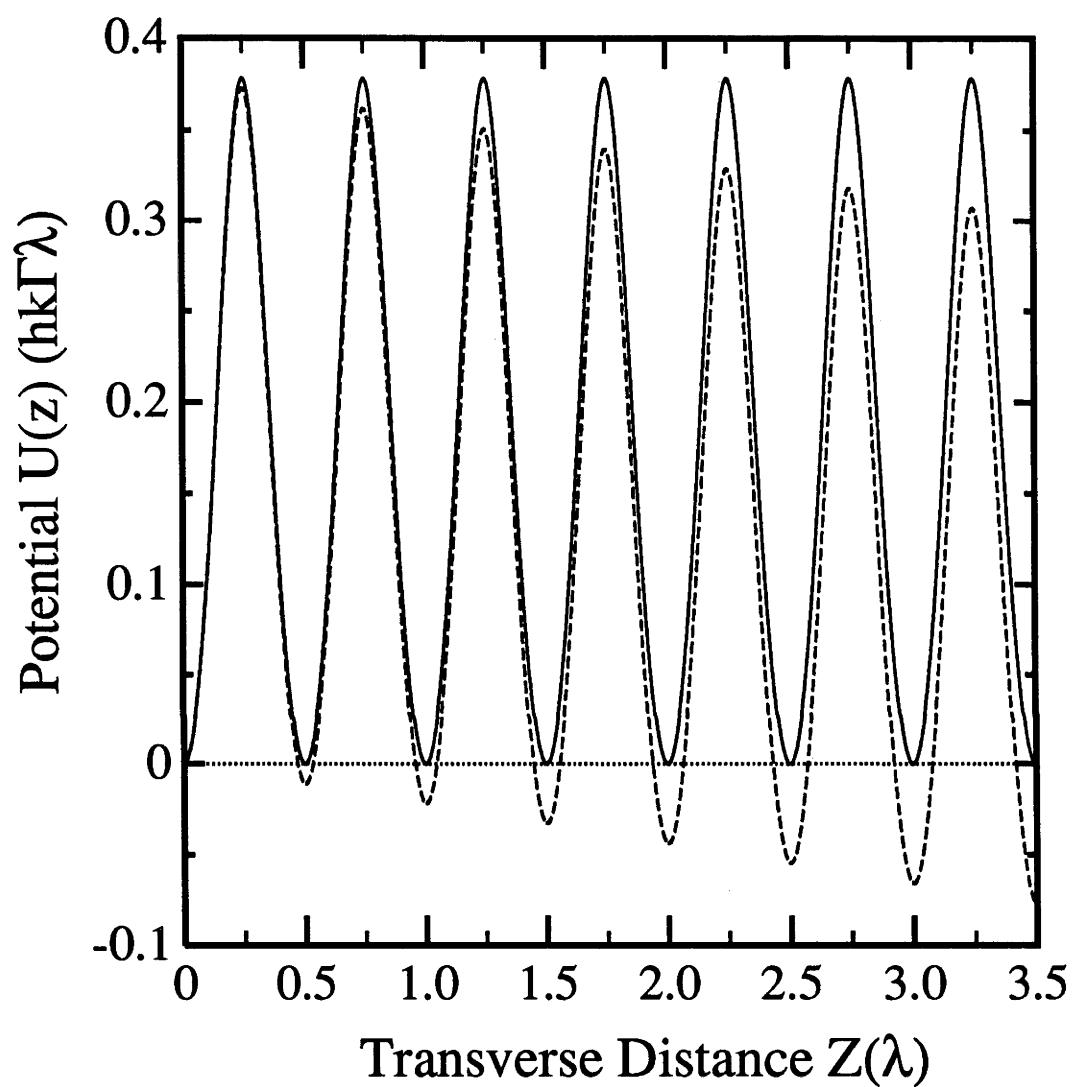


Figure 3.5: Continued fraction potential with (dashed curve) and without (solid curve) the heating term F_0 , assuming a constant transverse velocity of 1m/s (same condition as fig.3.1).

because

$$\frac{2G_0}{1 + 4\Omega^2/\Gamma^2 + 2G_0} < 1 \quad (3.10)$$

for all parameters, Eq.3.9 has the following form

$$F = \frac{A \sin(2kz)}{1 + B \cos(2kz)} \quad (3.11)$$

where $B < 1$. Using the true fact that $\sin(x) \cos^n(x)$, for any $n > 0$, can only be expanded to sine harmonic terms (this can be verified using mathematical method and the procedure is omitted here). Then the expansion of Eq.3.11 are only related to sine harmonic terms and the first a few terms are as follows

$$\begin{aligned} F_{\text{gradient}}(z) &= -\frac{\delta U(z)}{\delta z} \\ &= A \sin(2kz)[1 - B \cos(2kz) + B^2 \cos^2(2kz) - B^3 \cos^3(2kz) + \dots] \\ &\sim F[\sin(2kz), \sin(4kz), \sin(6kz), \sin(8kz), \dots] \end{aligned} \quad (3.12)$$

Similarly, the spatial variation of the force in fig.3.5 is approximately that of a sine-wave, resulting from the dominance of the sinusoidal terms.

As the detuning Ω is increased in Eq.3.9, the logarithmic expansion becomes closely sinusoidal. To illustrate this, the force term F_1^s is shown in the bottom of fig.3.6, while F_0 and F_1^c are shown in the top of fig.3.6 as a function of detuning for a fixed transverse velocity of $1.0m/s$. The significant feature here is that the F_1^s term is considerably larger in magnitude than the other terms. This dominance increases at very large detuning (many GHz), with the zeroth order and F_1^c terms approaching zero for detunings above $200MHz$. The result is that at very large detunings (where spontaneous events are negligible), the continued fraction solution to the force becomes purely conservative (i.e. negligible heating), and for small velocities closely approximates the gradient force which exactly follows the sinusoidal periodicity of the standing wave light field.

3.4 Simulation of Atomic Motion

In this section, we will present the details of the simulation of the atomic trajectories in a strong standing wave laser field which was perpendicular to the atomic beam axis.

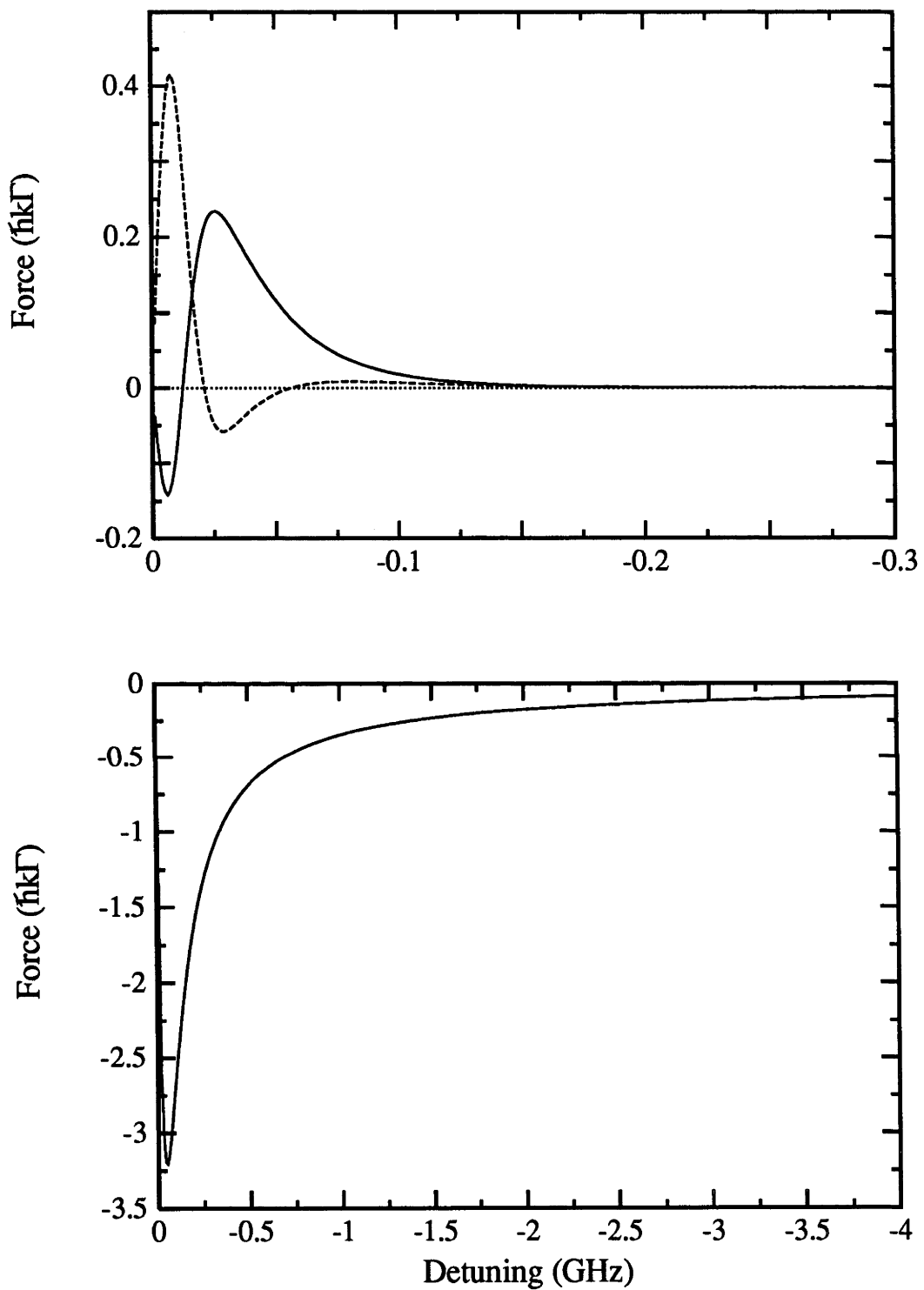


Figure 3.6: Variation of forces as function of detuning at a fixed intensity ($G = 70$) and transverse velocity ($v_t = 1.0\text{m/s}$). Top: Force F_0 (solid) and first order cosine term F_1^c (dashed). Bottom: First order sine term F_1^s . Note that the scales are different for these two graphics.

A calculation of the atomic trajectory from a source point from the oven nozzle was performed for a given transverse velocity.

The real electric field that an atom was subjected to as it moves through the standing wave laser wave was given by

$$E(z, t) = 2E_0 g(t) \cos(kz) \cos(\omega t) \quad (3.13)$$

In this expression $g(t)$ describes the time dependence of the field amplitude due to atom's passage through the laser beam with velocity v_l ($t = x/v_l$). For Gaussian laser profile: $g(t) = \exp(-t^2/2\tau^2) = \exp(-x^2/2a^2)$, where τ is the transit time for the radius (a) of $1/e$ intensity.

The trajectory of atoms in a given longitudinal velocity group (v_l) was calculated for each particular initial condition (position of source point, transverse velocity v_t). In these calculations it was assumed that the longitudinal velocity was unaffected by changes to the transverse velocity due to the disparity between the magnitudes of these two velocities. Later, in the next section we will show that it is a good approximation in our experimental conditions.

The calculation is based on the Newton's equation, i.e. $F = M \cdot dv/dt$. Under the condition that the change of time dt is small enough, then the velocity can be calculated using only the first order approximation as $v_f = v_i + M/Fdt$. If the diameter of the laser standing wave is $2a(mm)$ (e^{-1} point of the single traveling wave intensity), it is a good approximation to choose the interaction region from $a \times 10/3(mm)$ to $-a \times 10/3(mm)$ with which the zero point is in the center of the Gaussian standing wave laser field. (For example, for $4.2mm$ diameter standing wave laser field, the interaction region can be chosen for $-7mm$ to $7mm$). Beyond this region, the atom travels freely in space. In the interaction region, a total of 14000 steps was chosen to calculate the atomic trajectories and a small distance $\delta x = 2a \times 10/(3 \times 14000)m$ was corresponding to the distance steps for the atom propagating through the interaction region, for which the transit time $\delta t = \delta x/v_l$ for the longitudinal velocity (v_l) of atom. Consider a Gaussian standing wave laser field, the saturation parameter has the form

$$G = G_0 \exp(-\frac{x^2}{a^2}) \quad (3.14)$$

Within this small distance change, the intensity change of the laser field can be

calculated as

$$\delta G = -G \frac{2x}{a^2} \delta x \quad (3.15)$$

In this section of simulation, we will use the parameters which are chosen from one of our experiments. The diameter of the standing wave was selected to be $2a = 4.2mm$ and the central saturation parameter is $G_0 = 140$. Then $\delta x = 1\mu m$, $\delta t = \delta x/v_l = 10^{-9}s$ for the longitudinal velocity ($1000m/s$) and the saturation parameter change δG , from Eq.3.15, will be less than 0.4 and can be considered as constant.

The maximum transverse acceleration under the above conditions calculated was $a_t^{max} < 10^7 m/s^2$, yielding a maximum transverse velocity change $\delta v_t^{max} < 10^{-2} m/s$. For such small transverse velocity changes, the forces on atoms will keep almost constant over the distance δx (fig.3.1), and hence to a good approximation the final transverse velocity of atom can be calculated assuming a constant force over that small region. Using the new value for the transverse velocity, the atom is again propagated a distance δx , and the procedure repeated until the atom has left the interaction region.

3.4.1 Atomic Trajectories

The results of some of these propagation calculations are shown in fig.3.7, where the instantaneous atomic velocity for one source point is plotted as a function of propagation distance (x) for three values of the initial transverse velocity. The influence of the periodic potential is clearly shown by the oscillatory behavior of the atomic velocity. Channelling (see below) is indicated when the atomic velocity changes sign. It is clear from this behavior that the final velocity can be in the opposite direction to the initial velocity for some of those atoms which experience channelling.

The channelling effect can be explained using the potential property of the standing wave field. The motion of an atom in the standing wave is dominated by the potential $U(z)$ of the standing wave field (because of the force coefficient $F_1^s > F_0$) and the potential period is equal to one half the laser wavelength. From the potential expression (Eq.2.82), it is clear that for positive detuning ($\Omega > 0$), the potential wells coincide with the laser wave nodes and at a negative detuning ($\Omega < 0$) with its antinodes. The criterion for channelling to occur is that the sum of the instan-

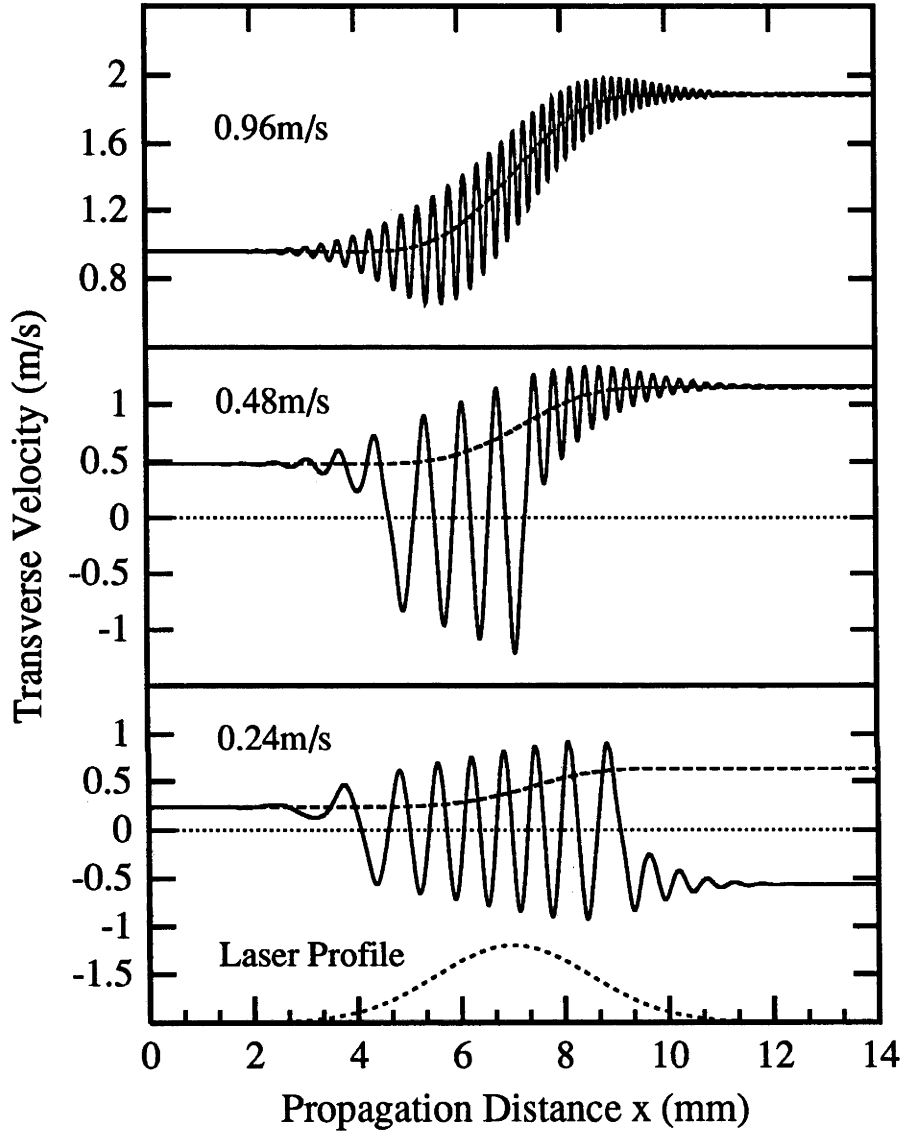


Figure 3.7: Instantaneous transverse velocity as a function of propagation distance (x) for three different initial transverse velocities. The longitudinal velocity is 1000 m/s, detuning is -75 MHz , and $G_0 = 140$. Solid curves—continued fraction solution; dashed curves—heating term (F_0) only. The dotted curve is the standing wave intensity profile.

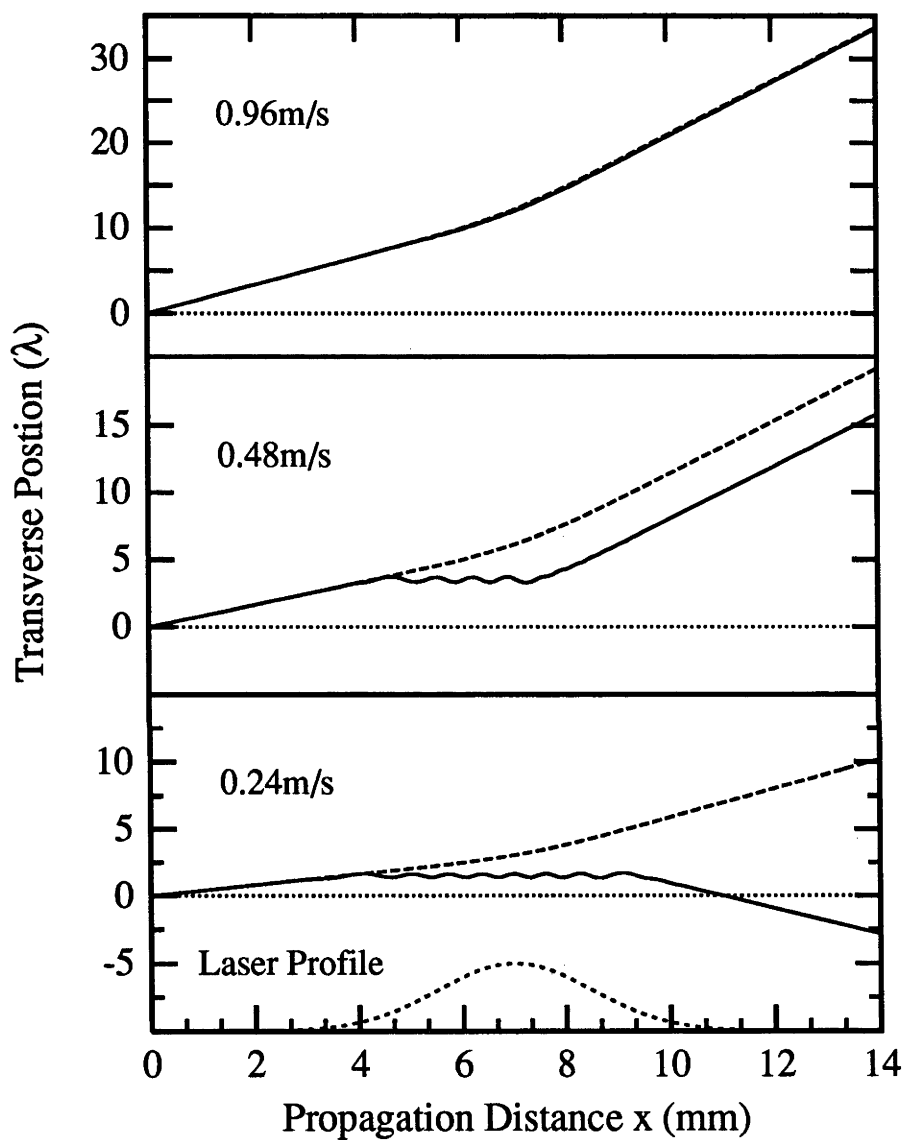


Figure 3.8: *Spatial trajectory for the cases in fig.3.7. Channelling of the atom between adjacent nodes of the standing wave can be clearly seen for the two lower velocities.*

taneous potential energy and transverse kinetic energy of the atom is less than the local depth of the standing wave potential. In a Gaussian standing wave laser field, after the atoms have passed the highest intensity region, they experience a gradually decreasing field. As soon as the total energy of the atoms is larger than the potential of the standing wave, the atoms will not be channelled in the standing wave laser field any more. The atoms can escape at both v_e and $-v_e$ directions (where v_e is the transverse escape velocity). As a result of channelling, the final direction was found to depend sensitively on the initial transverse velocity condition.

The spatial trajectories executed by atoms with the initial conditions of fig.3.7 are shown in fig.3.8. The oscillatory behavior is clearly the result of channelling in the periodic potential, and can result in widely varying final positions which again depend sensitively on the initial transverse velocity. For large initial transverse velocities (greater than the escape initial transverse velocity) the trajectory closely follows that for the heating term only.

The calculations were carried out for initial transverse velocities (in steps of $5 \times 10^{-4} m/s$) over the range from $-5 m/s$ to $5 m/s$ corresponding to the range of transverse velocities in almost all our experiments (except the experiment of Doppleron resonance).

3.4.2 $v_i^{in} \sim v_i^{out}$ Relationship

For each initial transverse velocity, a unique final transverse velocity was obtained. Fig.3.9 shows the results of such a calculation derived from a single source point using the continued fraction solution for a range of initial transverse velocities (in steps of $5 \times 10^{-5} m/s$. In order to save computing time and the disk space, we used steps of $5 \times 10^{-4} m/s$ in calculating the atomic spatial profiles). This figure shows that atoms can have a final transverse velocity in either positive or negative direction (depending on the initial conditions) due to channelling.

For some atoms, the initial transverse velocity is sufficiently large that channelling does not occur at any stage during the interaction with standing wave. The threshold for this condition is defined here as the escape initial transverse velocity (or capture transverse velocity) and has a value of $\sim 0.7 m/s$ under the conditions of $G_0 = 140$ and $\Omega/2\pi = -75 MHz$ (in fig.3.9). The value of this escape initial transverse velocity estimated using the simple gradient force expression (Eq.2.82)

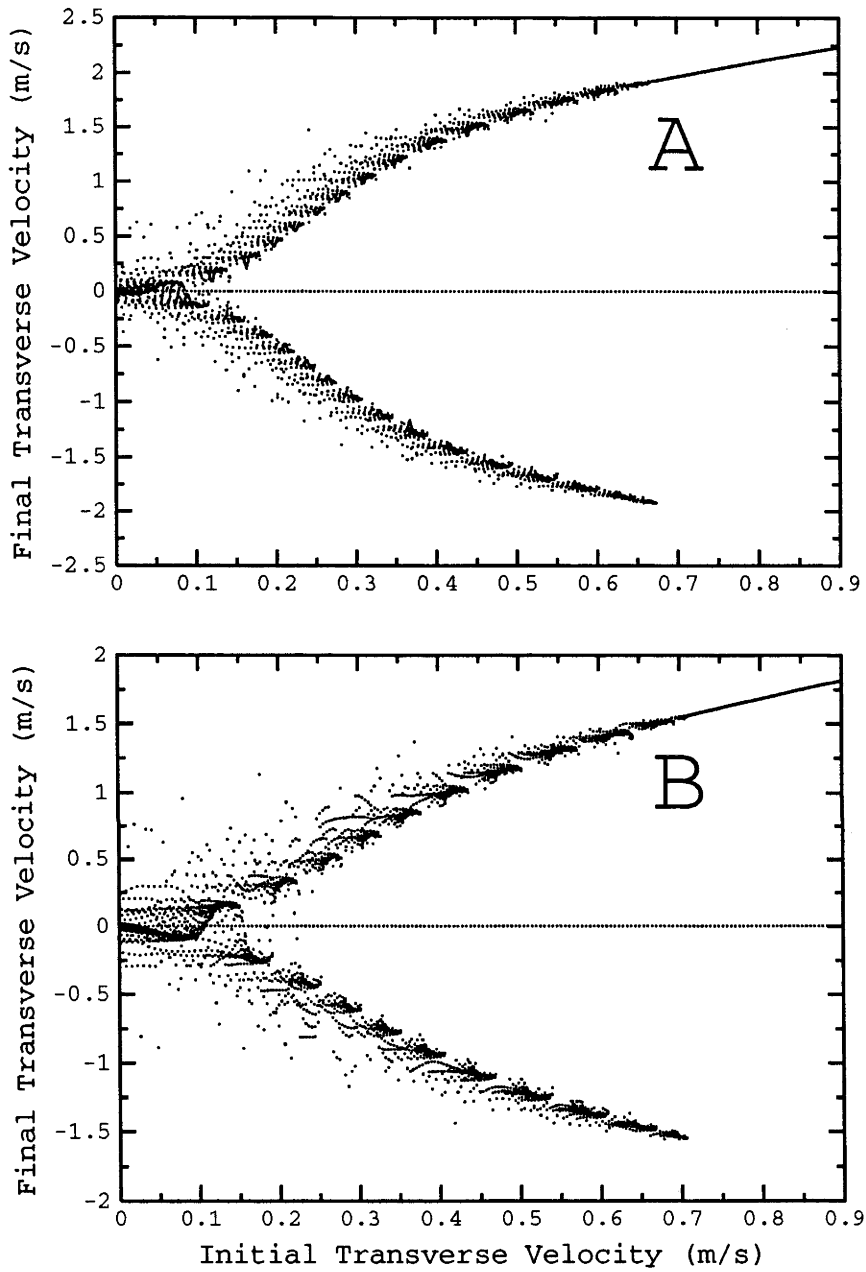


Figure 3.9: Plot of the final transverse velocity as a function of initial transverse velocity for a single source point for $G_0 = 140$, $\Omega/2\pi = -75\text{MHz}$. A: $v_l = 700\text{m/s}$; B: $v_l = 1000\text{m/s}$. Note: the scales of the final transverse velocity are different for these two curves.

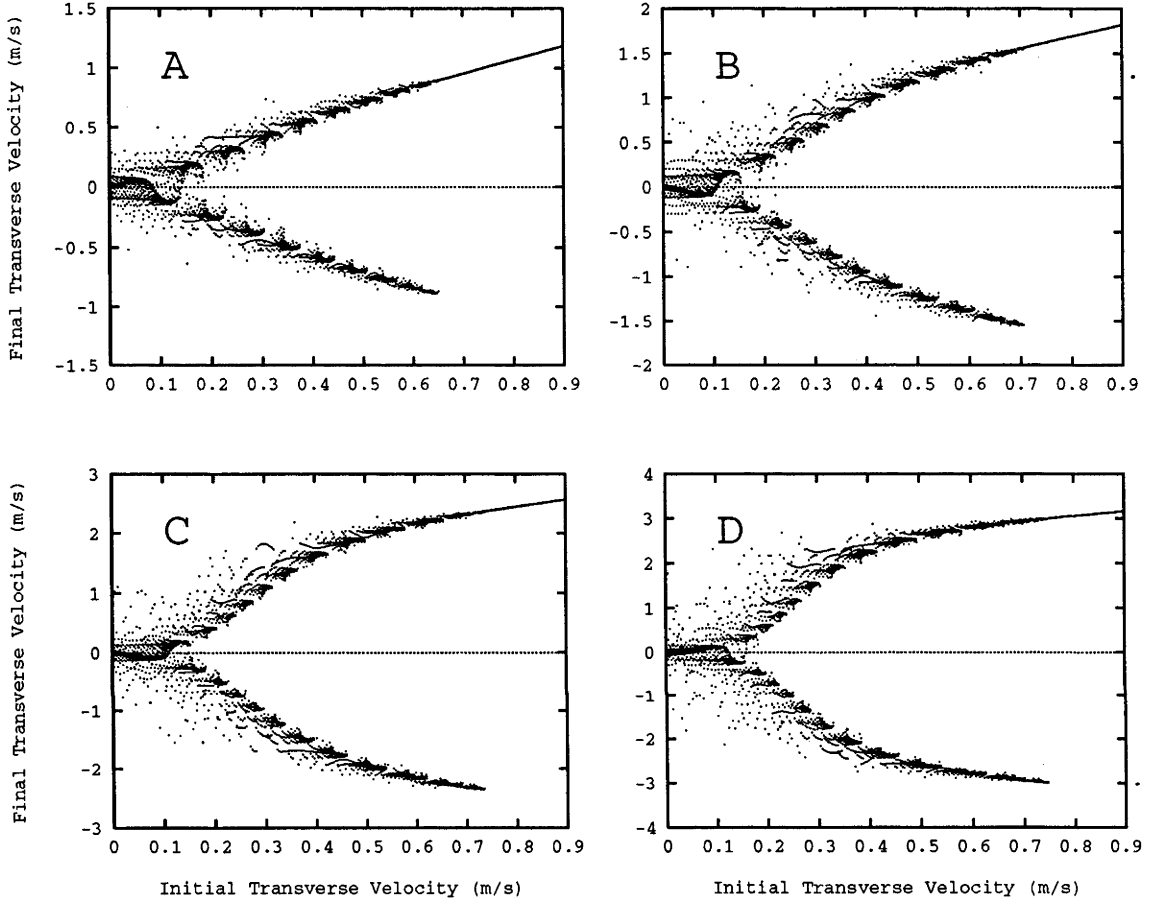


Figure 3.10: Plot of the final transverse velocity as a function of initial transverse velocity for a single source point for $v_l = 1000\text{m/s}$, $\Omega/2\pi = -75\text{MHz}$. A: $G_0 = 80$; B: $G_0 = 140$; C: $G_0 = 200$; D: $G_0 = 260$. Note: the scales of the final transverse velocity are different for these curves.

as $v_e = \sqrt{2U_{max}(z)/m}$ gave the result of $1.24m/s$ which is much larger than $0.7m/s$.

The difference between these two values is due to the heating force for small detuning. The atoms get accelerated in the transverse direction of motion and increase the kinetic energy, so atoms with much smaller initial transverse kinetic energy than the potential of the standing wave can escape. Fig.3.10 shows the final transverse velocity as a function of initial transverse velocity under different intensities of the standing wave. From this figure, it is apparent that when the intensity of the standing wave increases from $G_0 = 80$ to $G_0 = 260$, there is only a small increase of the escape transverse velocity. This is caused by the heating effect.

For atoms with initial transverse velocity significantly greater than the escape initial transverse velocity, the final transverse velocity invariably converges to the pure heating (spatially averaged) value due to the traversing of many standing wave periods.

Fig.3.11 shows an averaged plot of the magnitude of the final velocity versus initial velocity for the following force terms: dotted line—heating term F_0 only; dashed line— $F_0 + \text{gradient}$; solid line—continued fraction. The curves represent the average (over 250 source points in the $\lambda/2$ interval) of the magnitude of the final velocity for each initial transverse velocity.

We examine firstly the structure evident in these two figures. In fig.3.9 there is a pattern of modulations which are periodic with the initial velocity. The period of the modulations is found to be proportional to the laser wavelength. Furthermore, the modulations cease for initial transverse velocities greater than the escape initial transverse velocity ($\sim 0.7m/s$). It is therefore evident that the modulations are caused by the effect of the periodic potential on the atomic motion.

In fig.3.11 the modulations are manifested as ripples in the averaged curves for the two potentials which contain a periodic component ($F_0 + \text{gradient}$ and continued fraction). The pure heating term produces a smooth increase in the transverse velocity as expected.

We now examine the behavior of the final vs. initial velocity curves for various initial velocity regimes. Firstly, for transverse velocities very close to zero ($< 0.02m/s$), fig.3.11 indicates that both the gradient and continued fraction curves yield larger final transverse velocities than the pure heating term. This is because

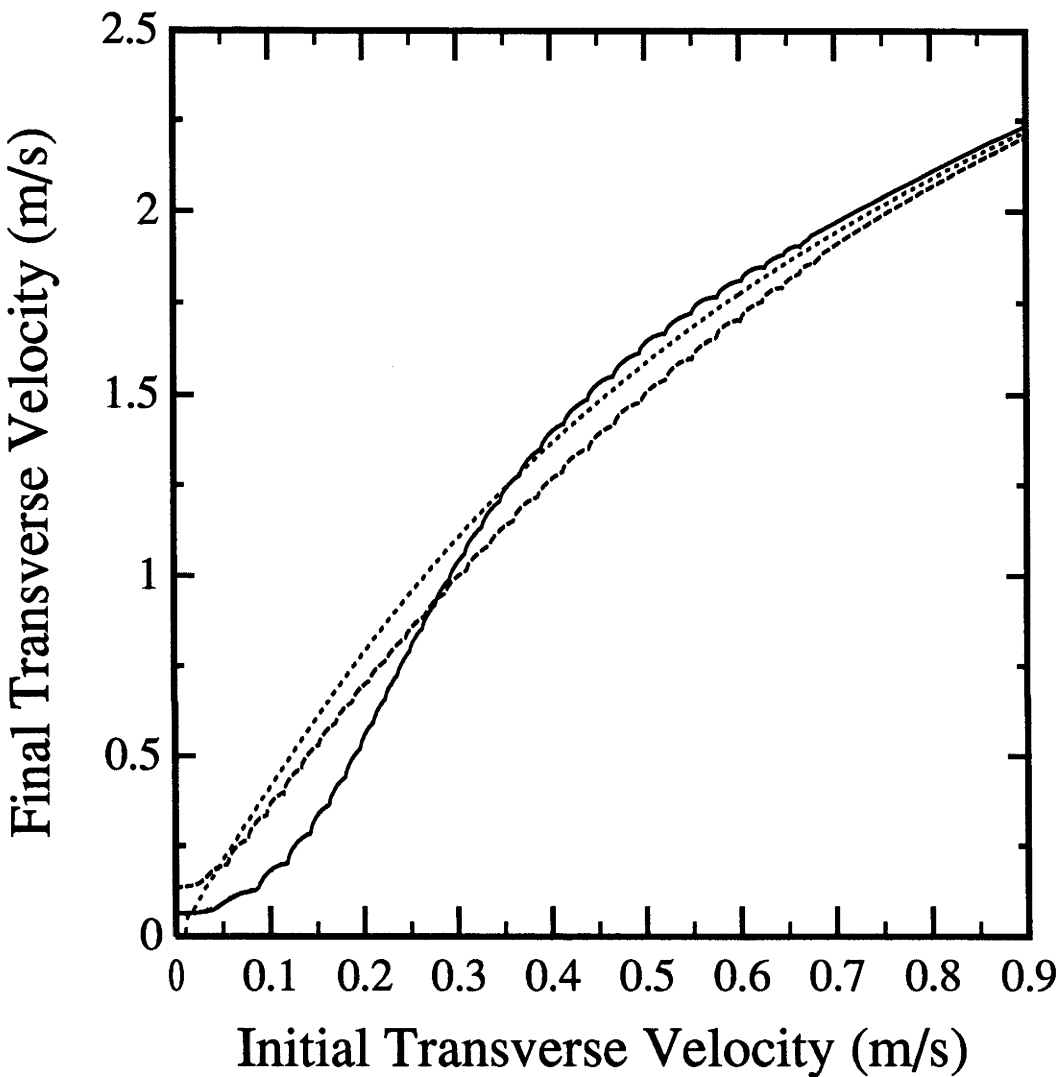


Figure 3.11: *Plot of final transverse velocity as a function of initial transverse velocity (for $G_0 = 140$, detuning = -75MHz and $v_l = 700\text{m/s}$). Dotted curve— heating (F_0) only; dashed curve— F_0 +gradient force; solid curve— continued fraction solution.*

only atoms with zero transverse velocity that travel through the valleys in the periodic potential remain undeflected. Since most atoms traverse regions of higher potential, they will experience some deflection and hence an increase in velocity. By contrast, the pure F_0 term will not accelerate atoms with zero transverse velocity.

Secondly, it is apparent from fig.3.9 that for atoms with an initial transverse velocity ($< 0.1m/s$) the magnitude of the final transverse velocity does not vary appreciably. A similar behavior is found in fig.3.11 for the averaged continued fraction calculation, and for a much smaller range of initial velocities for the $F_0 + \text{gradient}$ calculation. The result is that atoms which fall within this small initial transverse velocity range form a slowly diverging group which does not experience appreciable heating.

However, fig.3.9 shows that for initial transverse velocities larger than ($0.1m/s$), there is a marked bifurcation of final transverse velocities. This behavior indicates that following channelling, atoms either continue to move away from the atomic beam axis, or have a final velocity directed towards the atomic beam axis. In either case, the atoms are accelerated due to heating. Those atoms which have final velocities that are directed towards the atomic beam axis are in this sense “reflected”. (Note that reflection does not occur for atoms with greater than the escape initial velocity of $\sim 0.7m/s$). A similar reflection behavior has been reported experimentally by Esslinger et al. [47] for large detunings from resonance. These reflections result in the atoms crossing the center of the atomic beam axis at some point further downstream.

Another feature of the calculations shown in fig.3.11 is noticeable difference between the results for the $F_0 + \text{gradient}$ force, and the continued fraction solutions. It is clear that the addition of the (periodic) gradient force potential to the heating term F_0 reduces the final transverse velocity from that for the F_0 calculation alone. This reduction is even more marked for the continued fraction calculation, particularly at lower initial transverse velocities.

However, for transverse velocities larger than $0.35m/s$ a slightly higher final transverse velocity results for the continued fraction case than for the pure heating case. At very large transverse velocities, for which the exact nature of the periodic potential is less important, the two curves converge to the pure heating value. As a result, final transverse velocities greater than $4m/s$ were made equal to the value given by the heating term alone.

Given the similarity of the gradient and continued fraction forces (without F_0) in fig.3.2, the difference between the two cases in fig.3.9 may seem surprising. However, there are two factors which need to be considered. Firstly, as the transverse velocity of the atoms changes due to channelling in the periodic potential, it does not remain on a single continued fraction force curve (e.g. as shown in fig.3.2 for each standing wave period). Instead, the atoms experience a force which varies continuously from the higher to the lower transverse velocity force curves. Secondly, the effects of the very small differences in the two potential models are cumulative as the atom traverses the standing wave.

These cumulative effects are illustrated in fig.3.12, which shows the instantaneous transverse velocity vs. propagation distance for an atom with initial velocity $v_t = 0.08m/s$ (where the difference between the continued fraction and gradient force calculation is most marked in fig.3.11). As can be seen, the subtle differences in these forces result in a considerable difference in the instantaneous transverse velocities, with the final transverse velocities being very different in sign and magnitude.

As soon as the data of the output velocity as function of the input velocity are calculated, the transverse spatial profiles of the atomic beam can be calculated using the equation

$$y = y_0 + \frac{v_t^{in}}{v_l} \cdot x_1 + \frac{v_t^{out}}{v_l} \cdot x_2 \quad (3.16)$$

where y is new transverse position of the atom at the detector position, y_0 is the initial position of the atom at the oven nozzle, v_l is the longitudinal velocity of the atom traveling through the standing wave laser field, x_1 is the distance between the oven nozzle and the interaction position, and x_2 is the distance from the standing laser field to the detector plane. It is assumed here that the change in transverse position inside the standing wave is very small compared to $y - y_0$.

In the next chapters, most of the experimental results are simulated by using the $v_t^{in} \sim v_t^{out}$ data.

3.4.3 Effect of Longitudinal Velocity Change

In the above calculation, the longitudinal velocity change was ignored and in this section we will verify that it is a good approximation in our simulation.

The gradient forces caused by the Gaussian shape of the standing wave are much

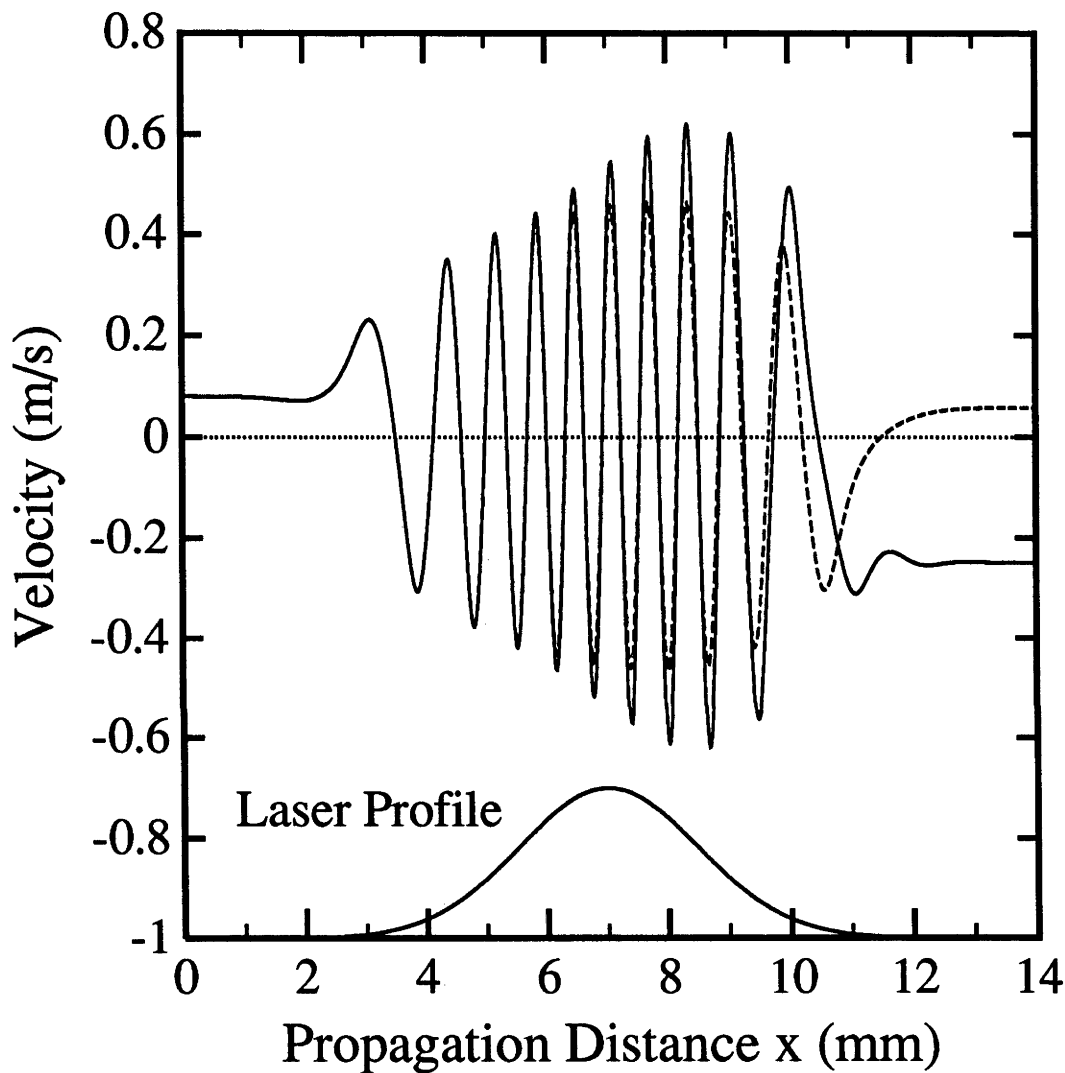


Figure 3.12: *Instantaneous transverse velocity as a function of propagation distance (x) for initial velocity $v_i = 0.08\text{m/s}$ (conditions as for fig.3.7). Solid curve—continued fraction solution; dashed curve—gradient force $+F_0$. The dotted line is the standing wave intensity profile.*

weaker (by $1/ka < 10^{-3}$, where a is the radius of the standing laser field) than the gradient forces along the standing wave potential (see Ref.[42]), so the maximum acceleration of longitudinal velocity in the standing wave is much smaller than the acceleration due to spontaneous emission for Na atoms ($\sim 10^6 m/s^2$). As the interaction time between the atomic beam and the standing wave is short (much shorter than $10\mu s$ in our situation), the maximum change of the atomic longitudinal velocity (moving in the first half of the Gaussian profile standing wave) is much less than $10m/s$.

We selected a worst situation where the acceleration of the longitudinal velocity was constant at $10^6 m/s^2$ for both spatial averaged and the first harmonic forces to calculate the transverse velocity change caused by the variation of longitudinal velocity. The effect on the transverse velocity is shown in fig.3.13 which shows that although there are small changes in detail, the overall effect on the atomic beam is negligible when v_l is assumed constant.

For large detunings ($\Omega/2\pi > 500MHz$), the spatial averaged force F_{\perp}^0 is almost zero. Within the velocity interval v_l and $v_l + 10m/s$, the force coefficients of sine and cosine harmonic terms that atoms experience in the standing wave are the same. Because the force in the first half of the Gaussian standing wave is almost the same as that, but with opposite sign, in the second half, the final result is that the positive and negative increases of the longitudinal velocity will cancel each other. So the final longitudinal velocity of atoms will be almost the same as the initial longitudinal velocity. Our calculation shows that the total change in v_l is less than $10^{-6}m/s$ for large detuning $\Omega/2\pi = 500MHz$. At these large detunings, the light force is conservative. Using conservation of energy, we find that the maximum transverse velocity change produced by this change in v_l is less than 10% for $v_l^{in} > 0.1m/s$.

For small detuning (e.g. $-75MHz$), there is energy exchange between the standing wave and the atoms, i.e. $v_{li}^2 + v_{lf}^2 \neq v_{li}^2 + v_{lf}^2$. The calculated maximum change of the longitudinal velocity is about $10^{-5}m/s$.

The longitudinal velocity of atoms only affects the interaction time. For atoms with large longitudinal velocity, the interaction time is shorter than atoms with small longitudinal velocity.

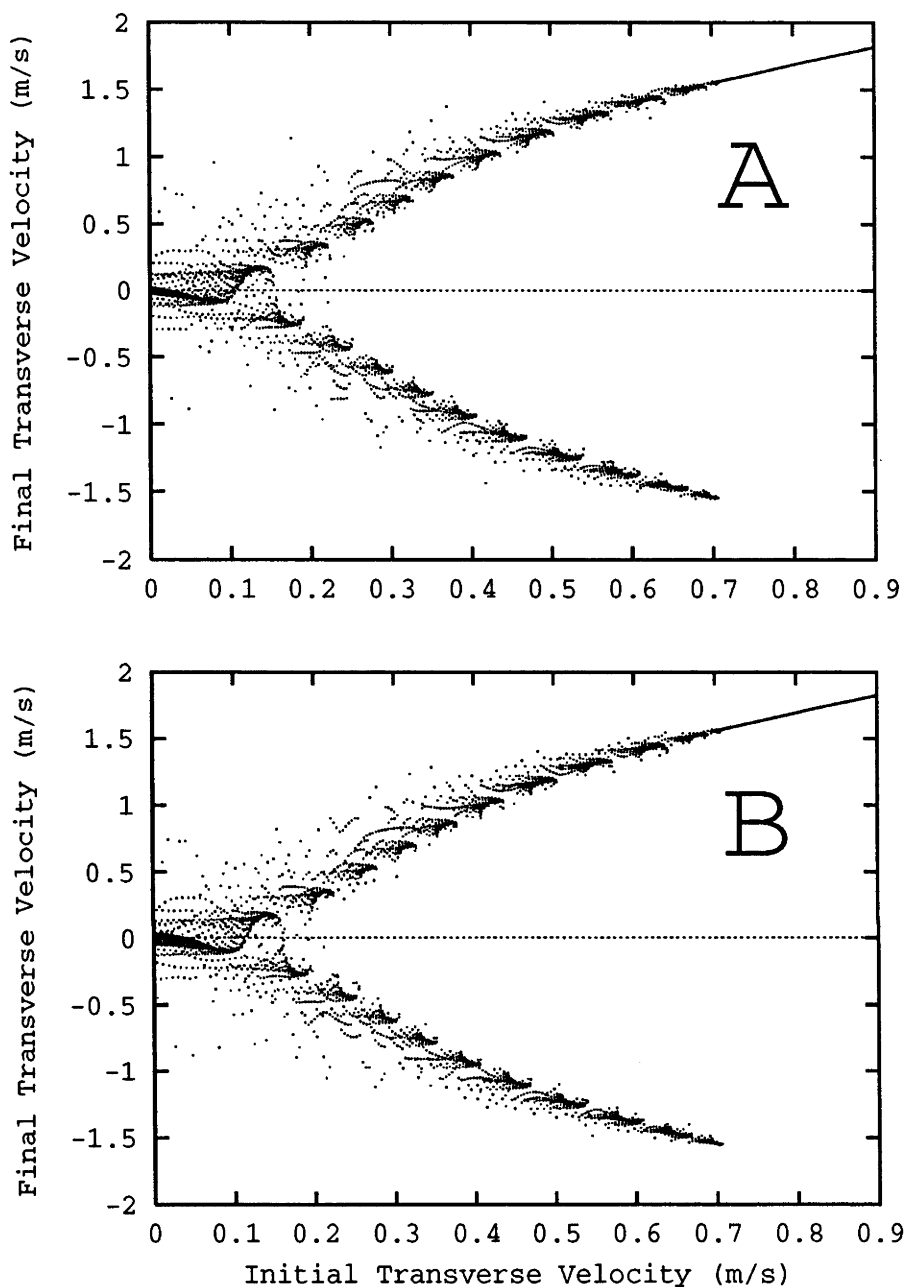


Figure 3.13: Examination of the influence of the change of the longitudinal velocity v_l on the transverse velocity v_t . A: fixed longitudinal velocity $v_l = 1000\text{m/s}$. B: variable longitudinal velocity $v_l^i = v_l^f + a \cdot dt$, where $a = 10^6[1 + \cos(2kz)]$ which is much larger than the maximum acceleration in the actual situation. The conditions are the same as in fig.3.9. The curves are almost exactly the same.

3.5 Diffusion Processes

The dipole force does not saturate at high intensity, so it is potentially more efficient for slowing atoms than 'Doppler' cooling, which does saturate[68, 24, 61]. However, the dipole force can have large fluctuations[62, 19, 22, 40]. These fluctuations, which lead to momentum diffusion, are predominately caused by the randomness in the direction of momentum recoil from stimulated transition for a high-intensity standing wave. An atom can absorb a photon from either counterpropagating traveling-wave component of the standing wave and can be stimulated to emit a photon by either wave. As a result, the atom will random walk in momentum space, similar to the Brownian motion of a particle which random walks in real space as the result of collisions with surrounding particles. Also, the spontaneous emission of photons in random directions can cause the atomic momentum to fluctuate. In an intense standing wave laser field, the dominant fluctuation mechanism is due to stimulated processes since the stimulated transition rate is proportional to the intensity of the standing wave and does not saturate, while the spontaneous emission will be saturated.

The diffusion coefficients $2D = \langle dp^2 \rangle / dt$ characterizing the rate of build-up of the mean square of momentum fluctuation from its mean value is given, according to Refs.[22, 60], by the following relations:

$$\begin{aligned} 2D_i &= 2\hbar^2 k^2 \Gamma G \cdot \frac{(1 + 4\Omega^2/\Gamma^2)^2 + 4(3 - 4\Omega^2/\Gamma^2)G + 48G^2 + 64G^3}{(1 + 4\Omega^2/\Gamma^2 + 4G)^3} \cdot \tan^2(kz) \\ 2D_{sp} &= 2\hbar^2 k^2 R = \frac{4\hbar^2 k^2 \Gamma G}{1 + 4\Omega^2/\Gamma^2 + 4G} \end{aligned} \quad (3.17)$$

Where $2D_i$ corresponds to the diffusion caused by induced emission and absorption of photons by an atom, whereas $2D_{sp}$ is due to spontaneous emission of photons, R has the same expression as in Eq.2.43. For a monochromatic standing light wave, the saturation parameter is $G = 4G_0 \cos^2(kz)$, G_0 is the single beam saturation parameter.

From Eqs.3.17, we can see that the diffusion coefficients $2D = 2D_i + 2D_{sp}$ is very sensitive to the detuning (Ω) of the laser field. Fig.3.14 and fig.3.15 give examples of how the momentum diffusion coefficients are dependent on the laser intensity and detuning. For large detunings (greater than $150MHz$, see fig.3.16), both induced and spontaneous momentum diffusion coefficients are almost equal to zero.

The diffusion processes will broaden the spatial transverse distribution of the atomic profile and are very important in explaining our experimental results in the next chapters. Because of the complexity and randomness properties of the diffusion, it is very difficult to include the diffusion processes in the simulation model. However, estimates of the effects of diffusion are given in the simulations where diffusion is likely to be important.

In summary of this chapter, the details of the simulation method were presented and the diffusion processes which are significant in small detuning were discussed.

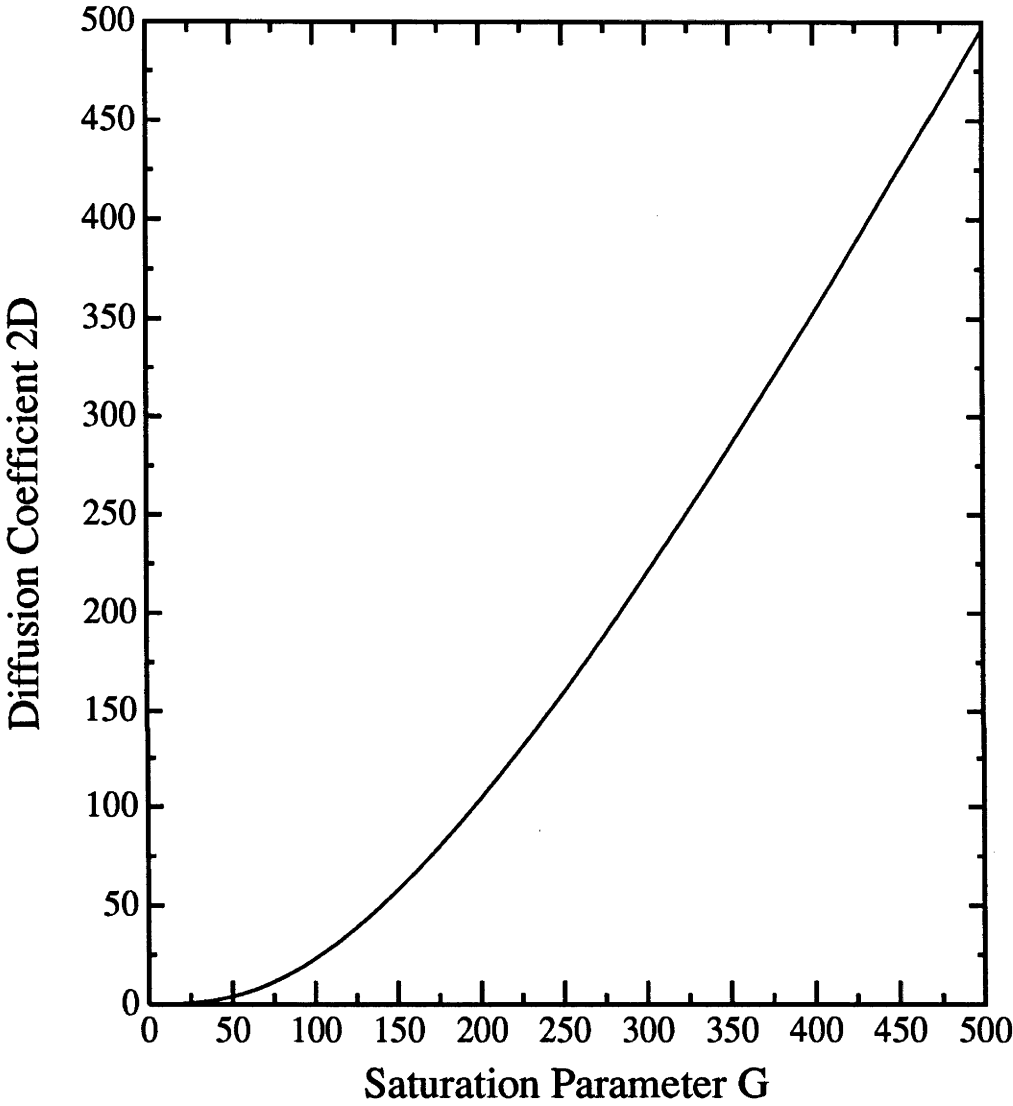


Figure 3.14: *Diffusion coefficients $2D = 2D_i + 2D_{sp}$ as a function of single laser saturation parameter G of standing wave ($\Omega/2\pi = -75\text{MHz}$).*

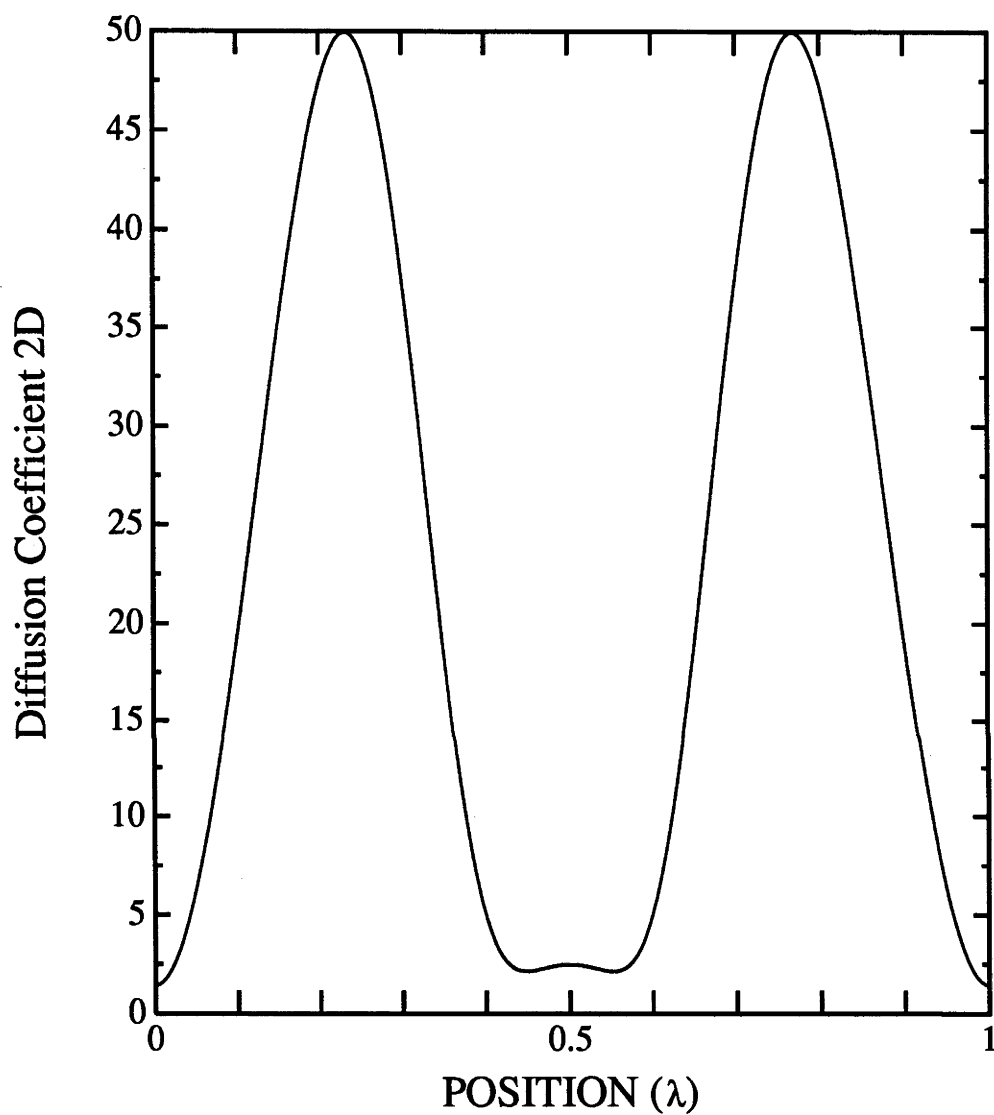


Figure 3.15: *Diffusion coefficient $2D$ as a function of position in a standing wave field. ($\Omega/2\pi = -75\text{MHz}$, $G_0 = 140$).*

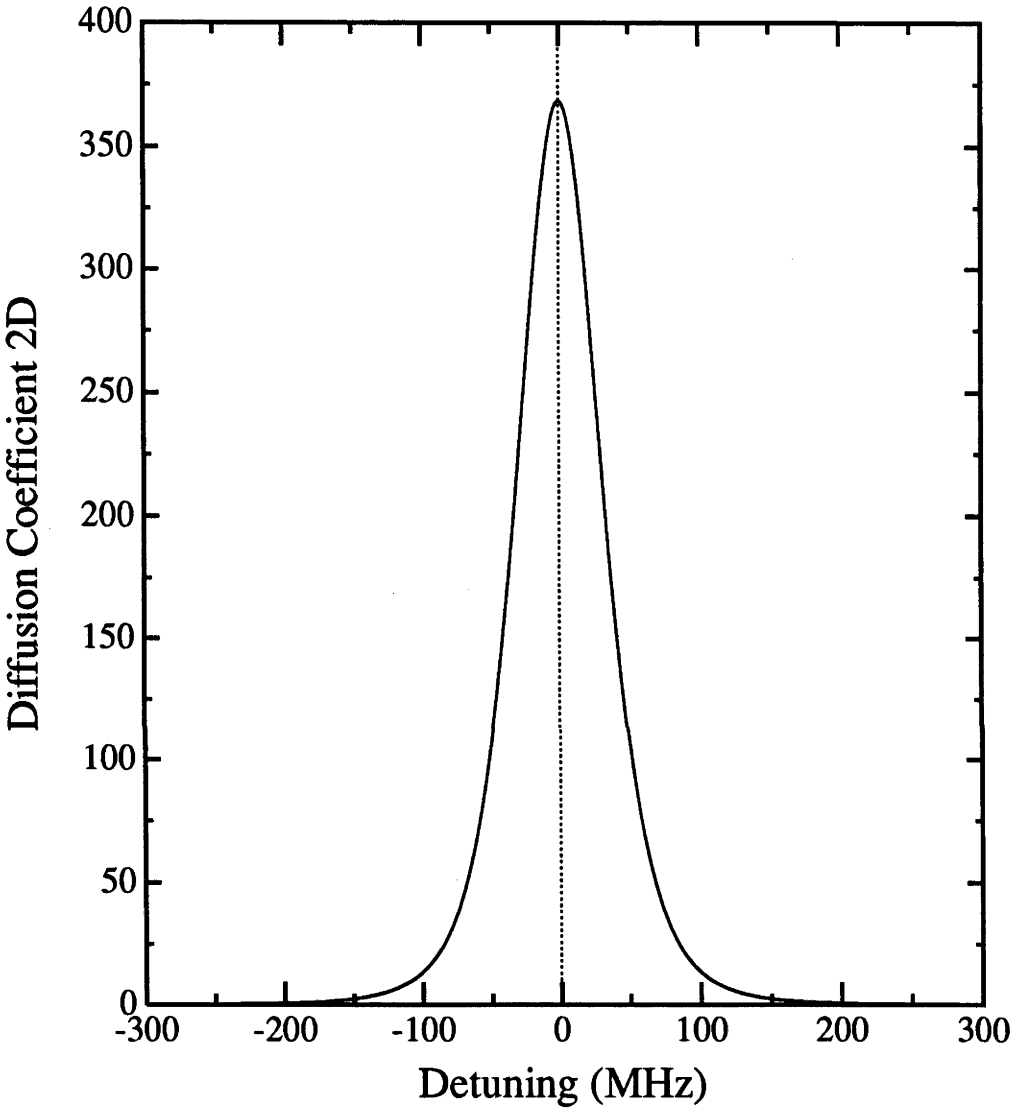


Figure 3.16: *Diffusion coefficient 2D as function of detuning in the antinode of standing wave laser field. ($G_0 = 140$).*

Chapter 4

Experimental Arrangement

In this chapter, we will present the details of experimental arrangement for performing the experiments on the interaction of an atomic beam with a strong standing wave laser field.

4.1 Formation of a Two-Level Atom System

In our experiments, the interaction time of atoms with the standing wave laser field is much longer (normally over 100 times larger) than the lifetime of the excited state of sodium atoms which means that the optical pumping could reduce the population of atoms dramatically in the interested level. In order to decrease the optical pumping effect, the experimental realization of multiple cycle interaction of atoms with laser radiation is essential in this work.

The *Na* atom energy level diagram is shown in fig.4.1 and it has many hyperfine levels. Using the optical pumping process, the atom can be transferred to a certain state of hyperfine structure from where the atoms will multiply interact with radiation of certain polarization. In this case the corresponding sublevels of hyperfine structure are a two-level system. One of such transitions of *Na* atom that satisfies the condition of multiple cycle interaction using σ^+ polarized laser field (two-level system) is $3^2S_{1/2} (F = 2) \rightarrow 3^2P_{3/2} (F' = 3)$, i.e. according to the selection rules the atom can decay back from the state $F' = 3$ only to the lower state with $F = 2$. Such cycle interaction can be realized by a CW single-mode dye laser, but in this case inevitable transitions occur into the higher state with $F' = 2$ due to the wing of absorption line, from where the atom may pass into the lower state with $F = 1$. In this state the atom cannot interact at all with the laser radiation because of a

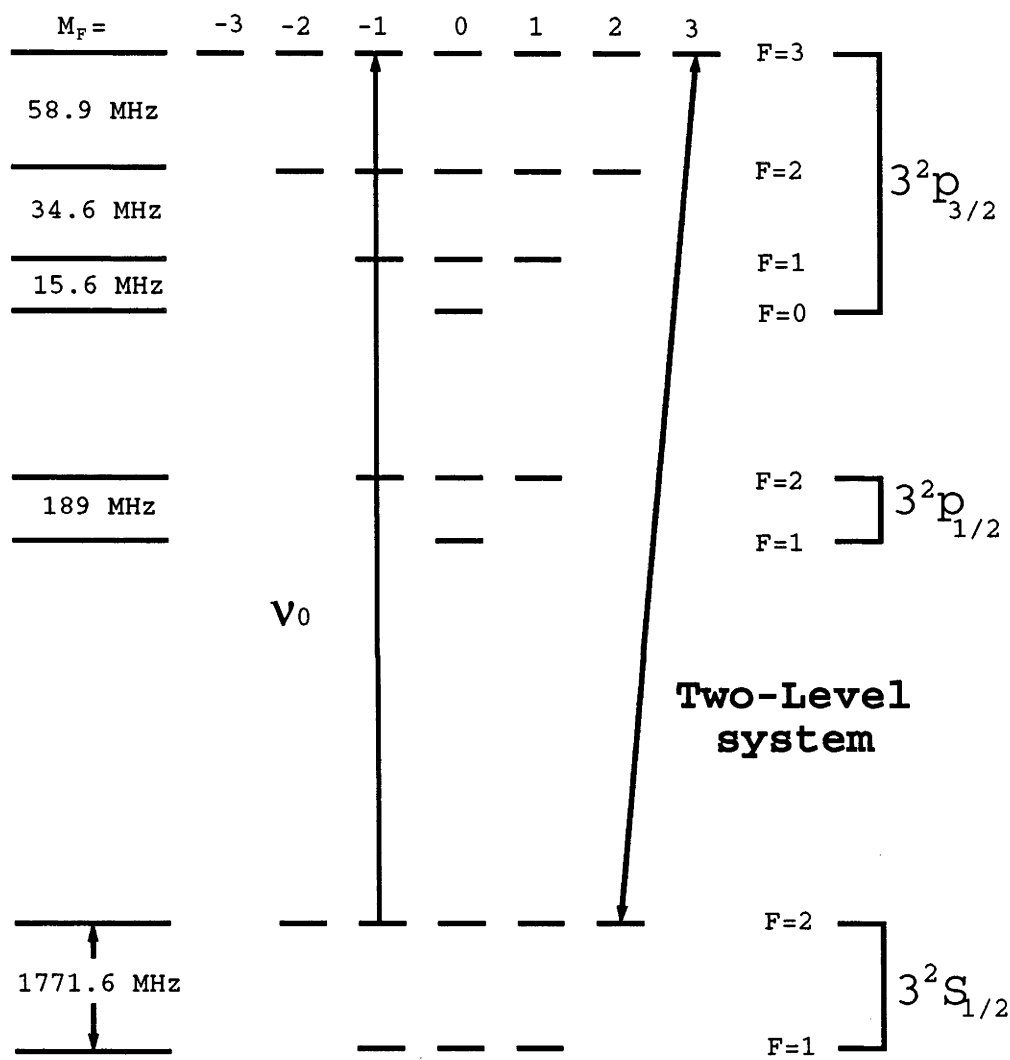


Figure 4.1: Energy-level diagram of sodium atoms.

great frequency shift between the components $F = 1$ and $F = 2$, i.e. there is a loss in the number of cycles in the atom-radiation interaction.

Using circularly polarized laser radiation tuned in resonance with the transition $F = 2 \rightarrow F' = 3$, there are transitions coming only with variations in the magnetic quantum number $m = +1$. This process results in optical orientation of the Na atom into the state $F = 2, m_F = 2$ from which it can be excited only into the higher states with $F' = 3, m'_F = 3$. The transition to the rest of the states are forbidden according to the selection rules in a dipole approximation. Thus, the atom in a state with $F = 2, m_F = 2$ and an excited state $F' = 3, m_F = 3$ may be considered as a two-level system in which cyclic interaction with laser radiation is possible.

Using prepumping of the atoms, the atoms could be optically prepumped to the $^2S_{1/2}$ ($F = 2, m_F = 2$) sublevel and therefore improving the SNR, especially for small detunings. The experimental requirement for prepumping is either using an extra dye laser or using an $1.77GHz$ AO modulator. The $1.77GHz$ EO modulator can not effectively prepump the atoms to ($F = 2, m_F = 2$) state because it is impossible to separate the side bands from the central frequency component. At present experimental facility conditions, it was impossible for us either to get an extra dye laser or to get an AO modulator to do the prepump. Therefore prepumping was not used.

4.2 Experimental Setup

The experimental setup is shown in fig.4.2. Two ring dye lasers were used in the experiment. The strong standing wave field was produced by *Coherent* – 699 which was pumped by an Ar^+ ion laser model 2030 manufactured by Spectra-Physics company. Using attenuator, we could change the intensity of the standing wave field and the isolator prevented the feedback of reflected laser beam into laser cavity which would affect the stabilization of both intensity and frequency of the laser. The laser beam was collimated to a smaller diameter using lens L_1 and L_2 . The total reflection mirrors, R_2 and R_3 were used to change the angle of the standing wave laser in respect to the atomic beam. Both LP (linear polarizer) and $\lambda/4$ plate were introduced to produce σ^+ circular polarized laser field.

The second ring dye laser used for detecting the atomic spatial profile was a commercial *Spectra – Physics* 380 pumped by another Ar^+ ion laser modeled 2020.

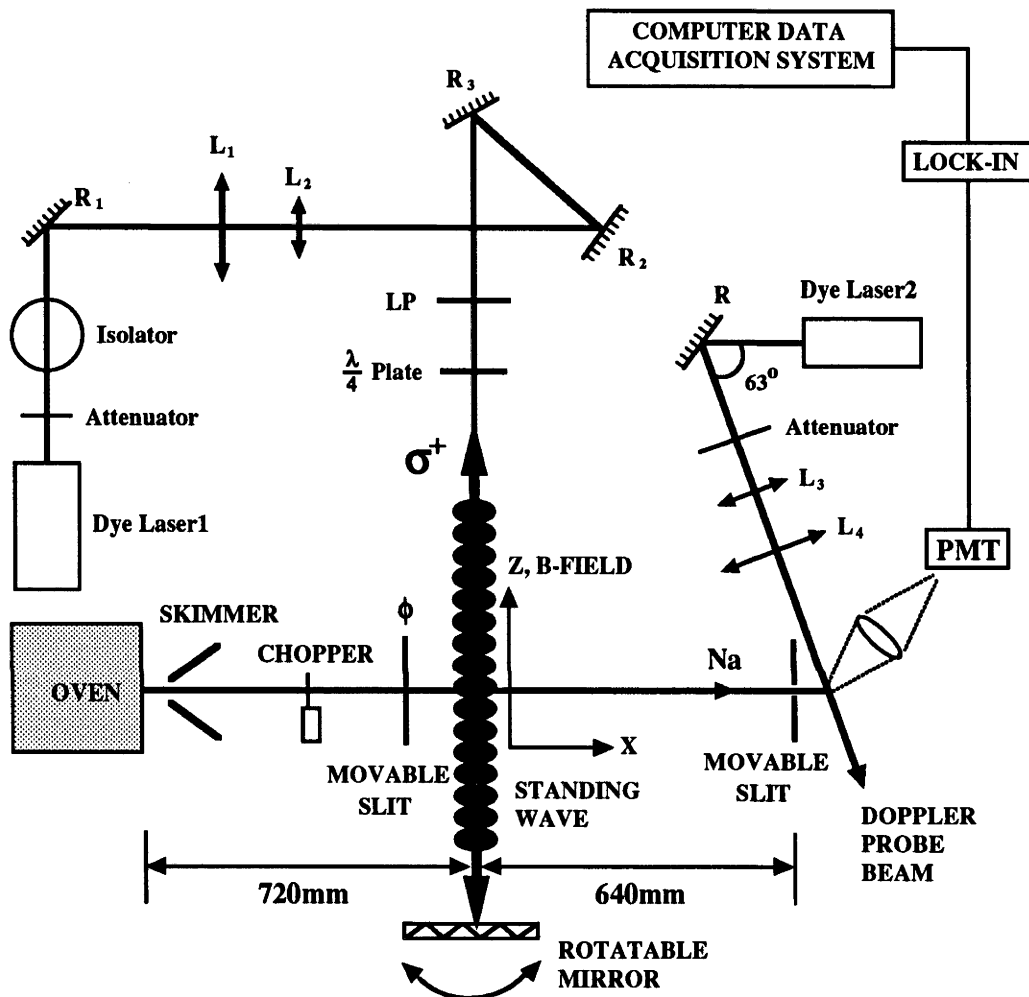


Figure 4.2: *Experimental arrangement. A thermal beam of Na atoms is intersected by an intense standing wave, which is formed by retroreflecting a laser beam from a CW ring dye laser. The transverse spatial distribution downstream of the standing wave is probed by detecting the fluorescence induced by a second ring dye laser which is placed in 63° to the atomic beam. The $60\mu\text{m}$ translatable slit defines the light induced fluorescence detector's spatial resolution. LP: linear polarizer. L_1 , L_2 and L_3 , L_4 are collimation lenses.*

This laser beam was expanded by using L_3 and L_4 collimation system and the intensity was reduced using another attenuator. The angle between the detecting laser beam and the atomic beam was set to be 63 degree to form a velocity sensitive detector system.

The atomic beam was chopped using a mechanical chopper and the reference signal from the chopper was sent to the lock-in amplifier. The lock-in amplifier was connected to a computer data acquisition system and the data were displayed and recorded by the computer (IBM-286).

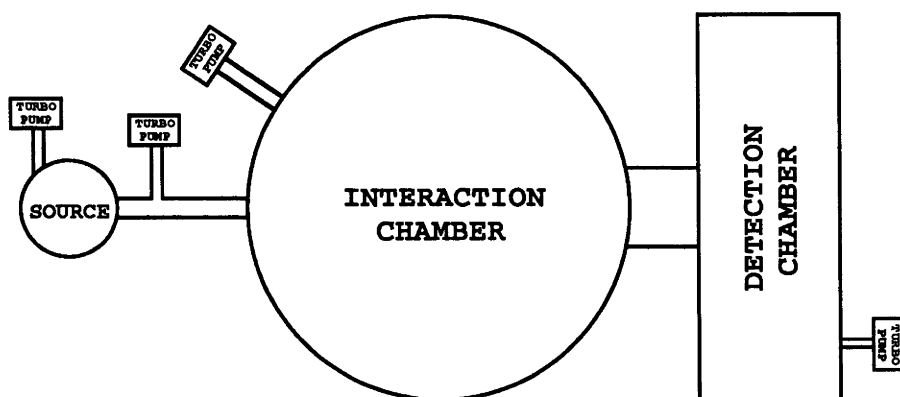


Figure 4.3: Schematic diagram of the three chambers of the atomic beam facility.

The entire atomic beam system was separated into three parts (see fig.4.3): the oven chamber (source), the interaction chamber and the detection chamber. Most of the vacuum system was designed by B.Brown and Bruce Stenlake [53] and most of the parts were manufactured by the Mechanical Workshops of Research School of Physical Science and Engineering, and Department of Physics & Theoretical Physics, the Australian National University.

The detailed diagrams of the oven and detection system are shown in fig.4.4 and fig.4.5. In the oven chamber, a sodium atomic beam was produced by a thermal oven source which can be operated at different temperature by changing the input heating current of the power supply. The oven nozzle was made using a 0.35mm diameter drill which was the smallest that we could be obtained. When the oven was operated at about 500°C and pumped by a turbomolecular pump, the pressure in the oven chamber was typically 2×10^{-5} mbar. The oven chamber was connected

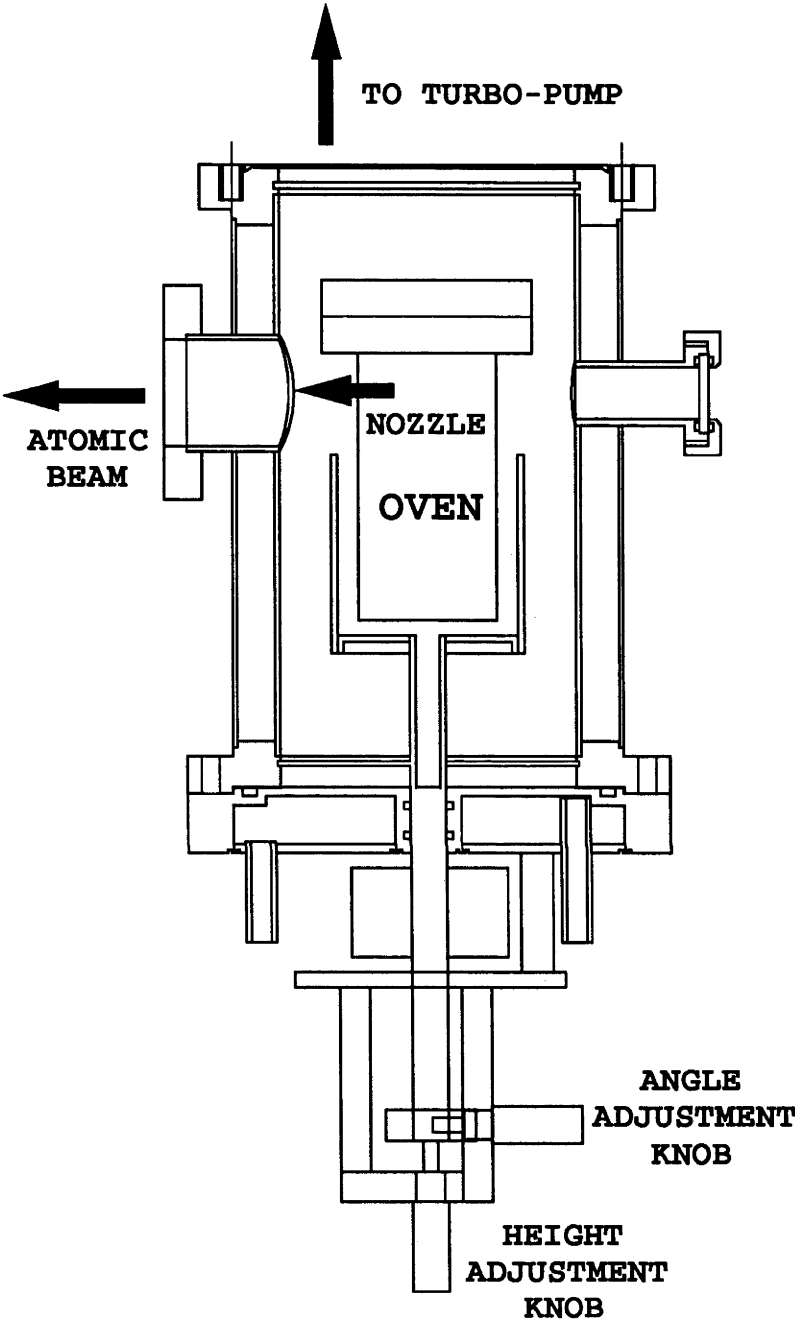


Figure 4.4: *Details of the oven chamber. The height and the angle of the oven could be adjusted using the external knobs.*

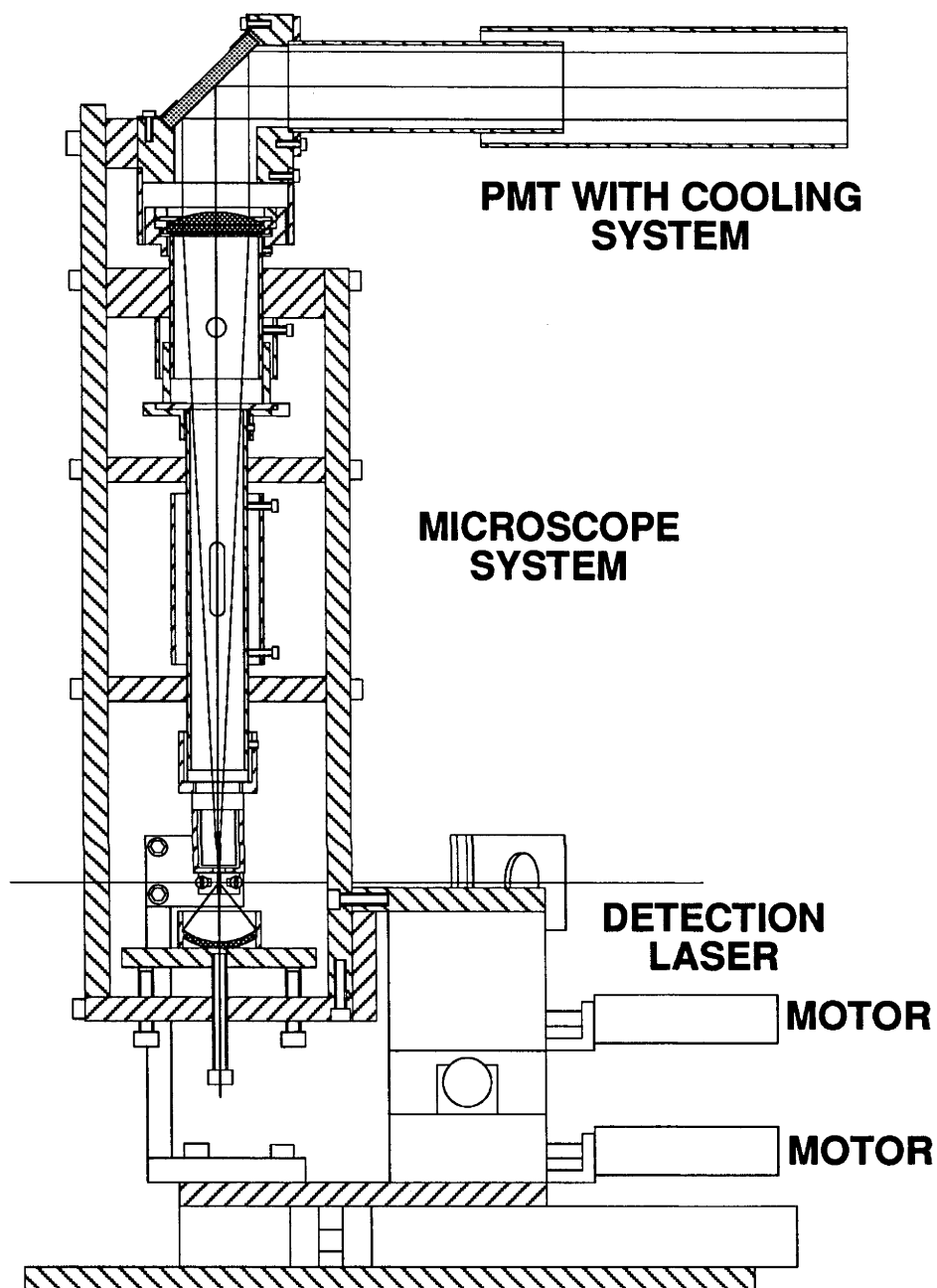


Figure 4.5: Details of the detection chamber. The laser induced fluorescence was collected by a microscope system and directed to a photo-multiplier which was cooled to -27°C to reduce the dark current noise.

to the standing wave interaction chamber by a differentially pumped region (it is a stainless steel tube with 30mm diameter and 370mm length) which was evacuated by a second turbo-molecular pump. Isolation of the differentially pumped region from the oven chamber was achieved using a 1mm diameter skimmer located about 10mm in front from the oven nozzle. To avoid the deposit of sodium atoms on the skimmer, a heating coil was used to heat the skimmer. The stainless steel wall of the oven chamber was cooled by water. In the next two sections, we will present the details of the interaction region and the detection area.

4.3 Interaction Region

The interaction chamber was a stainless steel round tank with diameter of 620mm. The interaction chamber was connected to the oven chamber via the tube described above. In order to reduce the background atoms in the interaction chamber, another $4 \times 6\text{mm}$ skimmer which can form a large enough atomic beam to interact with the standing wave laser field was used in the end of the tube. From our experience, the two skimmers in the both ends of the tube can dramatically reduce the background atoms in the interaction region. The interaction chamber was maintained at a pressure of about 5×10^{-6} mbar by a third turbo pump, yielding a mean free path many times the chamber diameter.

The atomic beam was then apertured to different sizes by using different skimmers placed just in front of the standing wave interaction region (about 10mm away from the standing wave). The maximum angle of the atomic beam divergence was determined by both the skimmer and the nozzle of the oven. From the book by Ramsey[54], the maximum angle (half width) can be calculated as $\theta = (r_n + r_s)/x_1$, where r_n is the radius of the oven nozzle, r_s is the radius of the skimmer in front of the standing wave and x_1 is the distance from the oven nozzle to the skimmer. A mechanical chopper could be put either in front or in the back of the standing wave. All components (including the high reflectivity mirror, the skimmer, the magnetic coil), except the chopper, were mounted in a stage with which the height and the angle between the atomic beam and the standing wave could be adjusted. This stage could be put at three different positions in the interaction chamber and, hence we could change the distance between the oven nozzle and the interaction region. (The distance from the oven nozzle to the detector was fixed to be 1360mm in the present experimental conditions). The three positions, under the present

experimental facility limitation, are fixed to be 650mm , 720mm and 780mm downstream from the oven nozzle. The standing wave was formed by retroreflecting the laser from a rotatable mirror located inside the interaction chamber.

A frequency stabilized commercial CW ring dye laser (Coherent 699-21 operated with R6G) formed the interaction standing wave, and could intersect the atomic beam in these three different positions in the interaction chamber. The laser beam could be collimated by a telescope system and the diameter could be changed by using the combination of lens with different focal lengths and also the interaction laser intensity could be changed by using a rotatable attenuator plate.

The interaction of the atoms with the standing wave defines the quantization axis, since this interaction is stronger than that due to any other fields, including the Earth's magnetic field. To further eliminate the background magnetic field and form a quantum axis for the interaction, a coil producing a magnetic field of $10 - 20\text{Gauss}$ was placed around the interaction region and the magnetic field was parallel to the interaction standing wave laser axis.

An effective two-level cycling system was realized using a quarter-wave plate to circularly polarize the standing wave so that atoms in the $F = 2, m_F = 2$ ground state can only be excited to the $F' = 3, m_F = 3$ excited state. Atoms not initially in the $F = 2, m_F = 2$ ground state will be optically pumped either into this state from which they can participate in the two-level cycling process, or into the $F = 1$ ground state hyperfine level and not interacting with the standing wave anymore (also could not be detected). As discussed earlier, optical prepumping of the atoms was not required as the detection method was state selective, detecting only those atoms which interacted with the standing wave.

4.4 Detection System

The detection region was housed in a separate chamber which was evacuated by a fourth turbo pump that maintained the pressure below 2×10^{-6} mbar. The detection chamber was connected to the interaction chamber through another stainless steel tube with 90mm diameter and 170mm length. In order to get better SNR, it is very important to reduce the background atoms in the detection chamber as low as possible and hence another $3 \times 35\text{mm}$ skimmer in one end (attached to the interaction chamber) of the tube was used allowing the atomic beam to reach the

detector and also to further reduce the background atoms in the detection chamber.

The velocity selective detection system consisted of a second, independently tunable laser (commercial Spectra-Physics 380D CW ring dye laser with R6G) which was tuned to the transition between the $^2S_{1/2}(F = 2)$ hyperfine ground state and an excited state to detect atoms only in the $^2S_{1/2}(F = 2)$ ground state. The laser induced fluorescence (LIF) produced as the atoms decayed into both $^2S_{1/2}(F = 2)$ and $^2S_{1/2}(F = 1)$ states yielding a signal proportional to the number of atoms in the $F = 2$ ground state. Strictly speaking, from the selection rule of interaction of atoms with light, there are 3 accessible upper hyperfine levels that can be detected due to the Doppler shift. Each upper hyperfine level corresponding to atoms with different longitudinal velocity. As there are more sublevels in the $F' = 3$ than the other two levels ($F' = 2$ and $F' = 1$), the fluorescence signal was dominated by the $F' = 3 \rightarrow F = 2$ transition.

The weak detection laser beam was set to be parallel to the $x - z$ plane and crossed the atomic beam at 63 degrees to the propagation axis of the atomic beam at a point 1360mm downstream from the oven nozzle. The LIF was detected by a photomultiplier via a microscope imaging system whose optical axis was in the y direction which was perpendicular to the plane formed by the atomic beam and the detection laser ($x - z$ plane). In our experiments, the detection laser power was about 0.3mW and the diameter was about 3mm and yielded a saturation parameter $G = 0.6$ which is close to 1 and could produce maximum fluorescence and not broaden the linewidth. The longitudinal velocity resolution was determined by the atomic linewidth (10MHz) which was much greater than the laser bandwidth (about 1MHz). The combination of intersection angle and detection bandwidth yielded a longitudinal velocity resolution of $\pm 6.5m/s$ ($= \Gamma/k \cos 63^\circ$). Different groups of atoms with different longitudinal velocities could be detected by changing the frequency of the detection laser. Because of the Doppler shift $\Omega_D = kv_l \cos 63^\circ$, where Ω_D is the detuning of the detection laser and v_l is longitudinal velocity of atoms, $\Omega_D = 100MHz$ frequency change of the detection laser corresponding to 130m/s change of the longitudinal velocity of atoms.

The detection chamber was separated from the tube by a movable slit which determined the spatial resolution of the apparatus. The slit width was 60 μm and was located 1360mm downstream from the oven nozzle. This defined the angular resolution of the detection system (assuming a point source at the standing wave)

to be $90\mu\text{rad}$, corresponding to a transverse velocity resolution of 0.09m/s ($3\hbar k$) for a longitudinal beam velocity of 1000m/s . The slit was mounted on a translation stage with a digital displacement encoder which allowed the atomic beam profile to be measured with a positional reproducibility $< 1\mu\text{m}$, which was much smaller than the spatial resolution. (In fact in the actual experiments, the position error in the acquired data traces was about $10\mu\text{m}$, because we had to turn on the slit driver and the computer by hand and it is very difficult to make them start simultaneously).

4.4.1 Adjustment of the Interaction Angle

The physics of the focusing experiments of atoms (see Chapter 6) produced an ideal method to adjust the angle between the atomic beam and the standing wave laser field. The standing wave was aligned perpendicular to the atomic beam axis by ensuring that the center of the focused velocity distribution using larger detuning (normally the detuning was selected around 1.0GHz in the experiments) coincided with the center of the atomic beam profile without the standing wave laser (the details of the focusing of the atomic beam will be discussed in Chapter 6). Because the focusing spot size of the atomic beam was almost the same size as the atomic oven nozzle, the error of the angle adjustment using this method was within $0.35/(2 \times 1400) = 0.13\text{mrad}$, here 0.35mm is the oven nozzle diameter and 1400mm is the distance from the oven nozzle to the detector.

The stability of the standing wave pattern was monitored by a Michelson interferometer to ensure that there was no movement of the standing wave pattern during the time required for an atom to traverse the interaction region (The maximum interaction time was shorter than a few milli-seconds in our experiments).

4.4.2 Determination Of The Detuning

The frequency of the standing wave laser field was tuned by a simple external power supply which using two batteries to produce a changeable voltage from -5 to 5volts , see fig.4.6. Coarse voltage changes were achieved by changing the resistance r_c , whereas fine voltage changes were achieved by alternating r_f . The changing of the voltage could be monitored by a multimeter (accurated to 0.01volt which corresponds to a frequency accuracy of $\nu_{scan}/1000$, where the ν_{scan} was the setting of the scan range of Coherent-699 and in units of GHz). By using this method,

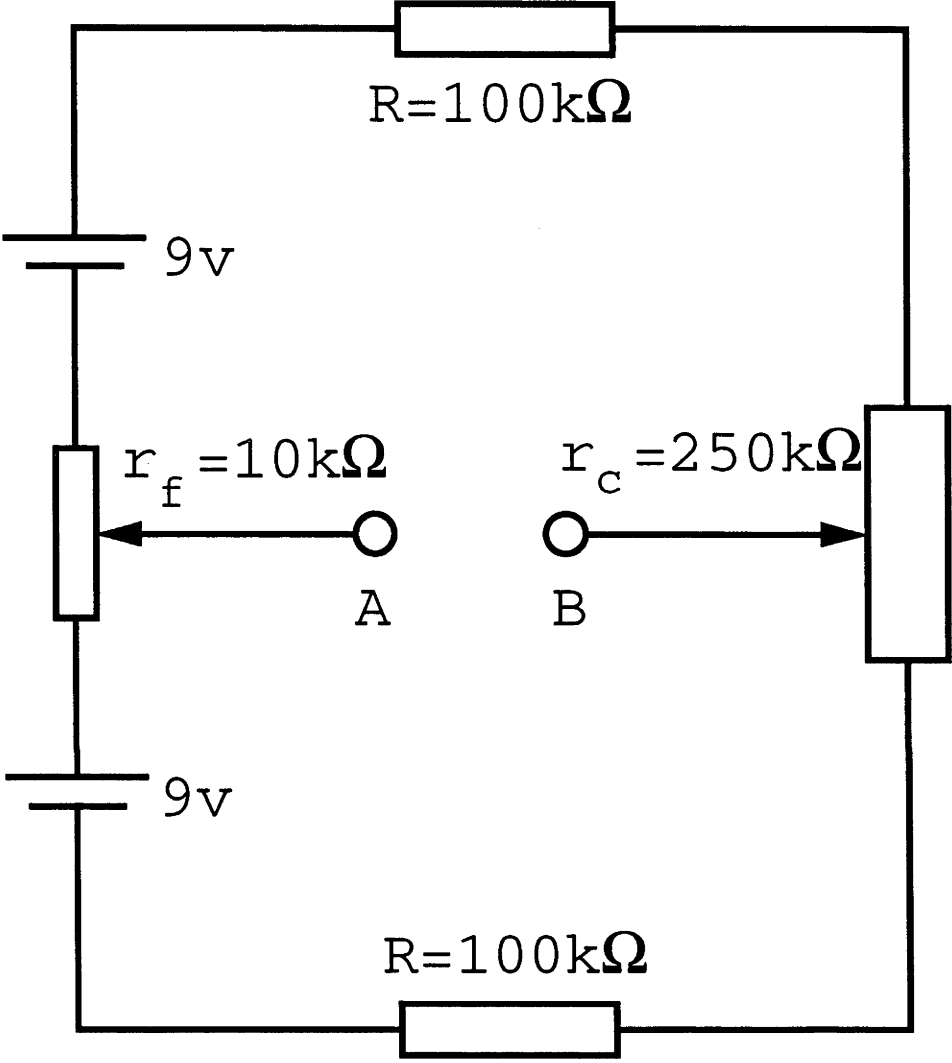


Figure 4.6: Circuit producing output voltage from -5v to 5v for changing the frequency of Coherent 699. r_c is the resistor for coarse adjustment and r_f for fine adjustment of the output voltage.

the accuracy of the frequency was around 4MHz for a 4GHz frequency scanning range.

In order to determine the detuning of the standing wave laser field from the atomic transition frequency, the zero detuning frequency of the standing wave laser had to be calibrated. The method applied in the experiments to determine the zero detuning was using the optical pumping process of the atoms. In a first stage, the power supply of the small magnetic field was turned off and therefore there was no separation between the magnetic sublevels of the atoms. Secondly, the standing wave laser intensity was reduced to about 10mW and the diameter of the standing wave expanded to about 1cm which could give a saturation parameter ($G_0 = 3$) (The power broadening of the atomic linewidth was about 2 times larger than the natural linewidth of the atoms). Then move out the quarter-wave plate from the optical path to let the atoms interact with the linear polarized beam. Under such conditions, when the detuning was zero, from the measurement, the output of the lock-in amplifier was almost zero which means that almost all of the atoms in the $3s\ ^2S_{1/2}(m_F = 2)$ state were pumped to $3s\ ^2S_{1/2}(m_F = 1)$ hyperfine state. Then the voltage of the external driven field of the Coherent-699 ring dye laser was recorded. By changing the voltage of the power supply exerting on the Coherent 699, we can calculate the detuning of the standing wave laser field. The linewidth of the atomic transition was 10MHz for sodium and the error caused by the uncertainty of the voltage of the power supply on 699 was less than 5MHz . So the total uncertainty of the detuning from the central frequency (zero detuning) was better than $\pm 20\text{MHz}$ in our experiments. As the forces that the atoms experienced would not change abruptly, within this error, there was not too much change in the atomic beam profile and hence there was no need to further control the frequency of the lasers.

The detuning of the standing wave was calibrated using a $300 \pm 1\text{MHz}$ free spectral range etalon before and after each experiment. Normally, each scan took 100 to 120 seconds and a series of experimental data (10 to 20 scans) took 20 to 40 minutes and the standing wave laser frequency drift during this time was normally about 40MHz . This drift was probably due to thermal variation in the length of the reference cavity to which the frequency of the standing wave was locked. Any laser mode hop would result in frequency change of larger than 500MHz and made the signal change dramatically.

4.4.3 Determination of D_2 Line of Sodium

Two methods were used in our laboratory to set the laser frequency to the D_2 (5890Å) line of the sodium atoms. The first and simple method was using a He-Ne wave-meter built by the former Ph.D. student in the Department. The second method was from the optical molasses experiments in the same laboratory (see the Appendix) by observing the bright spots (trapped atoms) in the center of the glass molasses cell, because there would be no bright spot in the cell for D_1 line and the optical molasses appears only for D_2 line. (for the details of optical molasses, please see [55]).

4.5 Measurement of the Standing Wave Laser Beam Diameter

The diameter of the strong standing wave laser beam at the interaction region was measured by using a narrow slit and recording the intensity behind the slit as a function of the slit position. The size of the slit was determined using diffraction of laser from a small slit and calculated $b = \lambda/\theta$, where λ was the wavelength of the laser beam and θ was the diffraction angle which was derived by measuring the width of the diffracted laser beam and the distance from the slit to the screen. In our measurement, the size of the slit was set to be 0.01mm.

The apparatus used for this beam diameter measurement is shown in fig.4.7. The photo-diode behind the movable slit had an active area sufficiently large to record all of the diffraction pattern caused by the small slit. The output of the photo-diode was recorded by the computer data-acquisition system.

A comparison between the experimentally measured beam profile of the strong standing wave laser field and the fitted curve $f(x) = \exp(-x^2/0.8^2)$, (where the unit for x is mm), is shown in fig.4.8. From this figure, the $1/e$ intensity diameter of the strong standing wave laser beam was found to be $1.6 \pm 0.1\text{mm}$ at the interaction region for this particular experimental configuration.

4.6 Experimental Procedure

Here we will present some experimental procedures common to all of the experiments described in this thesis. The detailed experimental procedure for each experiment will be provided in the chapters related to the experiments. It is very important in the first instant to make sure that the atomic beam traverses the standing wave laser beam at correct position (the maximum standing wave laser intensity region). The interaction position alignment of the standing wave laser beam and the atomic beam was carried out in two steps. The first step was to observe the fluorescence emitted by atoms interacting with the standing wave which was tuned to zero detuning and to make coarse adjustment of the standing wave position until the brightest fluorescence was seen by eye in the interaction region. Then the detuning of the standing wave was set around 1GHz and the standing wave position was finely adjusted to make sure that the focused narrow central peak (see Chapter 6) in the transverse atomic profile was at a maximum.

In the next chapters, experimental results using the experimental setup described in this chapter will be given.

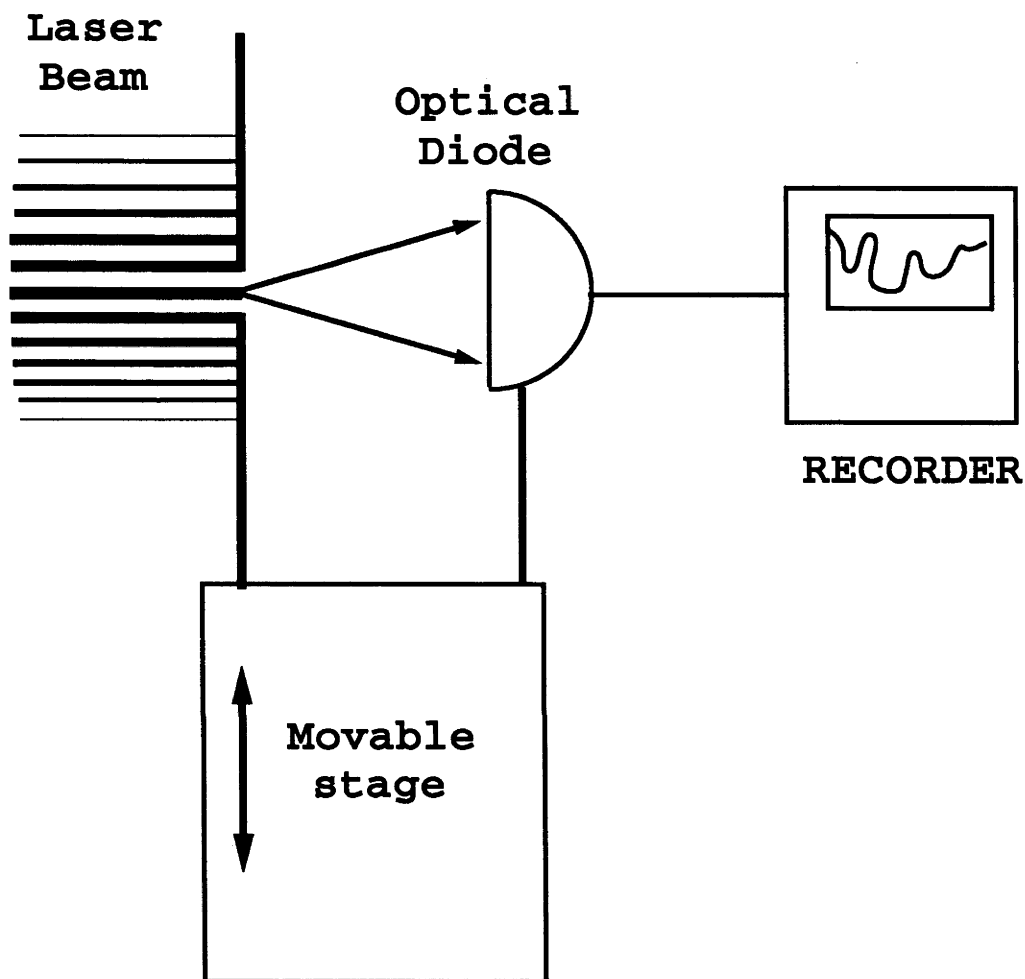


Figure 4.7: Schematic diagram of the apparatus used to measure the beam diameter of the standing wave laser.

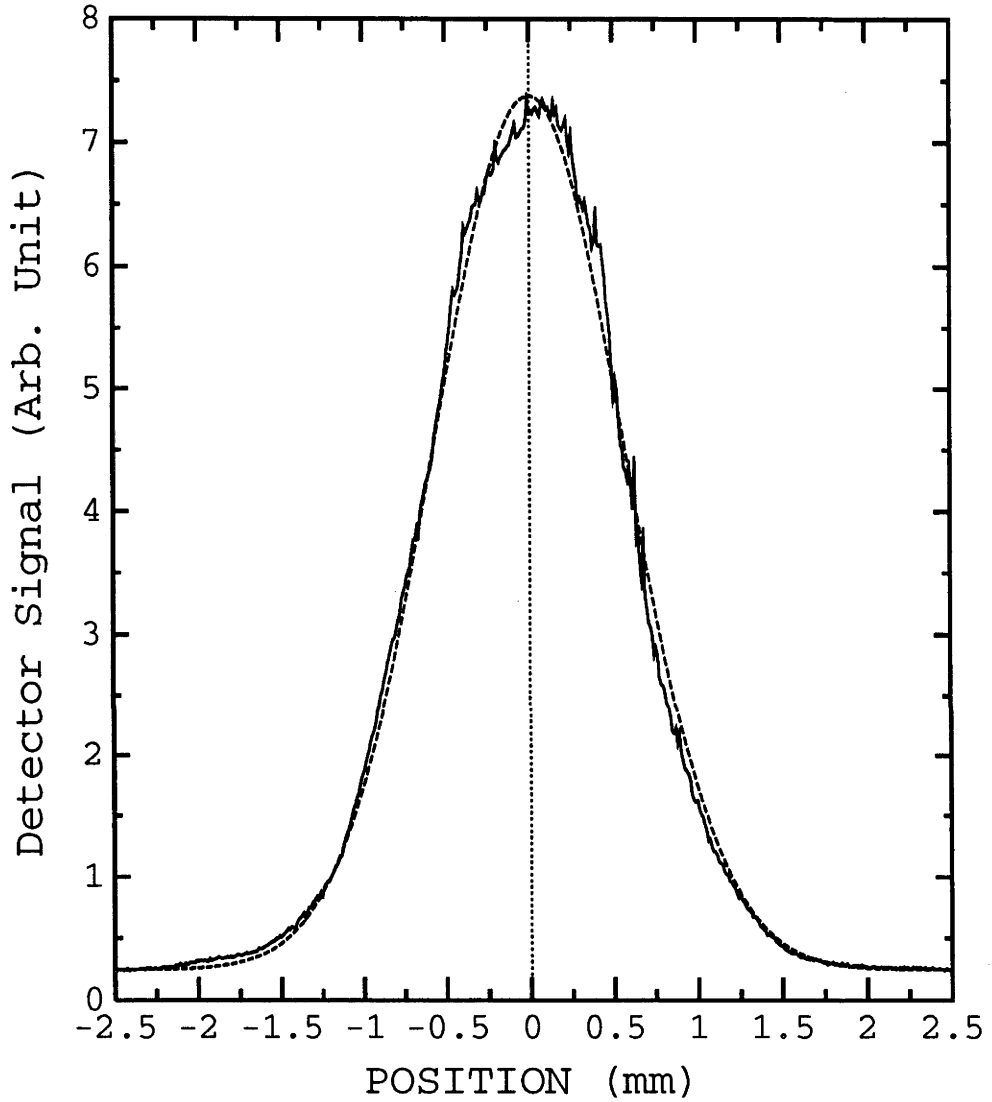


Figure 4.8: Comparison between the measured (solid line) and the fitted curve $f(x) = 7.3\exp(-x^2/0.8^2)$ (dashed line) for one Gaussian standing wave laser diameter measurement. The resulting diameter was $1.6 \pm 0.1\text{mm}$ in this configuration.

Chapter 5

Heating Effects with Stimulated Emission

In the former chapters, we presented the details of the force calculation and the simulation of the interaction of an atomic beam with a strong standing wave field using the continued fraction solution. In this chapter, we will present the experimental results of an atomic beam interacting with a strong perpendicular standing wave laser field. We use the method described in the former chapters to simulate the interaction. Heating of atoms with small transverse velocities for small negative detuning was observed and was in good agreement with the simulation results.

5.1 Experimental Arrangement and Parameters

The schematic of the experimental setup was mentioned in Chapter 4. In this experiment, the distance between the oven nozzle and the standing wave was set to be $720 \pm 5mm$ and the distance from the standing wave to the detector was $640 \pm 5mm$. The diameter of the oven nozzle was $0.35 \pm 0.02mm$ and the diameter of the Gaussian laser beam ($1/e^2$ point of the maximum intensity) was $4.2 \pm 0.5mm$. There was a $1.0mm$ diameter skimmer just in front of the interaction region to allow a maximum transverse divergence angle (full width) of $1.90mrad$ [= $(0.35 + 1.0)/720$]. The laser output power was $108 \pm 20mW$, giving a peak intensity in the standing wave of $780 \pm 145mW/cm^2$. The saturation intensity (i.e. $\omega_R = \Gamma/\sqrt{2}$) of the $F = 2, m_F = 2 \rightarrow F' = 3, m_F = 3$ transition using circularly polarized light is $I_s = 6.4mW/cm^2$, yielding a peak saturation parameter $G_0 = 120 \pm 30$. The saturation intensity I_s was calculated using the following definition of the light

intensity

$$I_s = \frac{1}{2} c \epsilon_0 E_s^2 \quad (5.1)$$

where c is the light speed in free space and ϵ_0 is the permittivity. From the definition of the saturation parameter, the saturation amplitude of the electrical field of light E_s has the form $E_s = \hbar \Gamma / \sqrt{2} \mu$. The dipole moment μ can be calculated using Einstein spontaneous emission coefficient which has the form (see, for example, the book *Introduction to Quantum Theory*[65])

$$\Gamma = A = \frac{\omega_0^3 \mu^2}{3\pi \hbar \epsilon_0 c^3} \quad (5.2)$$

From this equation

$$\mu^2 = \frac{3\pi \hbar \Gamma \epsilon_0 c^3}{\omega_0^3} \quad (5.3)$$

Then the saturation intensity, from Eq.5.1, has the form

$$\begin{aligned} I_s &= \frac{1}{2} c \epsilon_0 \cdot \frac{\Gamma^2 \hbar^2}{2\mu^2} = \frac{c \epsilon_0 \Gamma^2 \hbar^2}{4} \cdot \frac{1}{\mu^2} = \frac{c \epsilon_0 \Gamma^2 \hbar^2}{4} \cdot \frac{\omega_0^3}{3\pi \hbar \Gamma \epsilon_0 c^3} \\ &= \frac{c \pi \hbar \Gamma}{3\lambda^3} \end{aligned} \quad (5.4)$$

For sodium atom, $\Gamma = 2\pi \times 10^7$, $\lambda = 5890 \text{ \AA}$ and the saturation intensity has the value of $I_s = 6.4 \text{ mW/cm}^2$.

For a Gaussian laser beam, the amplitude of the electrical field has the form

$$E(r) = E_0 \exp\left[-\frac{r^2}{2a^2}\right] \quad (5.5)$$

and the intensity of the beam has the form

$$I = I_0 \exp\left[-\frac{r^2}{a^2}\right] \quad (5.6)$$

From this equation, the power of the Gaussian laser beam can be calculated

$$P = \int_0^\infty I_0 \exp\left[-\frac{r^2}{a^2}\right] ds = \int_0^\infty I_0 \exp\left[-\frac{r^2}{a^2}\right] 2\pi r dr = \pi a^2 I_0 \quad (5.7)$$

So the peak saturation parameter G_0 can be calculated

$$G_0 = \frac{I_0}{I_s} = \frac{P}{\pi a^2 I_s} \quad (5.8)$$

5.2 Experimental Results

Fig.5.1 shows the experimental results of the atomic beam transverse spatial distri-

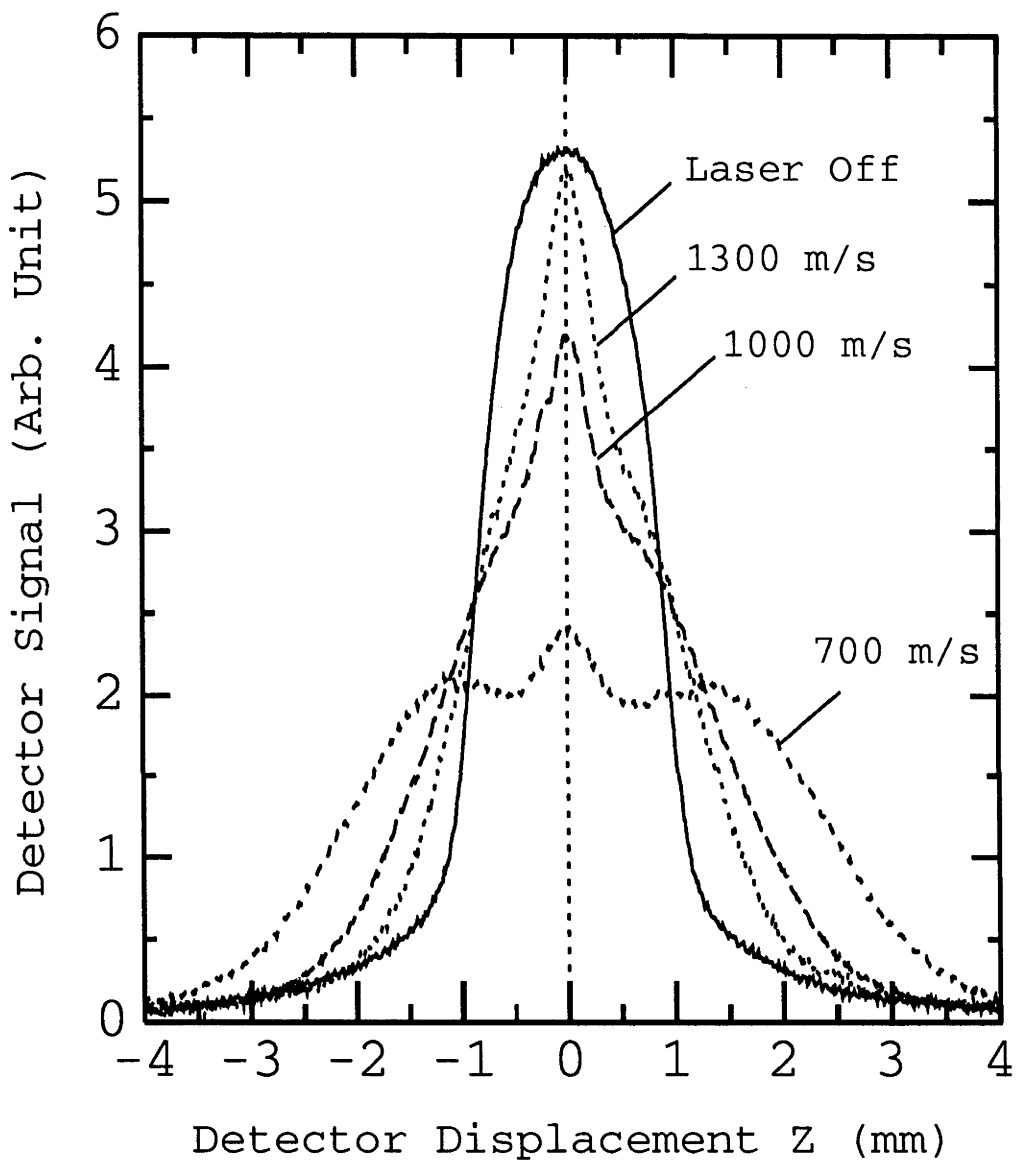


Figure 5.1: Variation of the experimental transverse atomic beam spatial distribution with three different longitudinal velocities for $\Omega/2\pi = -75\text{MHz}$, $P = 100\text{mW}$ and diameter of the standing wave laser = 4.2mm . Also shown is the atomic beam distribution with the standing wave laser off. All spatial profiles are normalized by area.

butions for three different longitudinal velocity groups in the presence of a standing wave with a fixed detuning. Also shown is the experimental far field spatial distribution for the initial atomic beam in the absence of the standing wave, which was approximately the same for all longitudinal velocity groups. Except where stated otherwise, all spatial profiles (both experimental and theoretical) are normalised by area to allow direct comparison of the shape of the final distribution, obviating the need to correct for changes in the beam density as a function of longitudinal velocity.

The main feature of the experimental profiles is the heating of the atoms for negative detuning. There are two broad, symmetric peaks produced by higher initial transverse velocity atoms. These atoms traverse a number of wavelengths and are heated by the spatially averaged zeroth order force, and emerge directed away from the atomic beam axis. Fig.5.1 indicates that the heating of the atomic beam increases as the longitudinal velocity decreases. This behavior is consistent with the integrated heating effect being greater for the longitudinal velocity group which experiences the longest interaction time in the standing wave.

In fig.5.2 the spatial distribution for one longitudinal velocity (1000m/s) and three different intensities is shown for the same conditions as fig.5.1. The variation of the atomic beam profile with the interaction laser intensity is very similar to the variation with longitudinal velocity. To a first approximation, at the transverse velocities employed in these experiments, the relative magnitudes of the Fourier components are similar over this variation in intensity, while the total force increases uniformly with intensity. Thus, a similar degree of heating of the atomic beam results either by altering the interaction strength (intensity) or the interaction time (longitudinal beam velocity).

It should be noted that the transverse crossover velocity from heating to cooling for the zeroth order force F_0 in fig.3.1 (at which point atoms accumulate given a sufficiently long interaction time) is about 6m/s . The maximum transverse velocity for which there was measurable change in signal due to heating in the experiment was 5m/s , and hence the great majority of atoms were not accelerated to the crossover velocity. This indicates that the interaction times in this experiment were too short for the accelerated atoms to have reached an equilibrium transverse velocity distribution, consistent with the strong dependence of the spatial beam profiles on the interaction time and intensity.

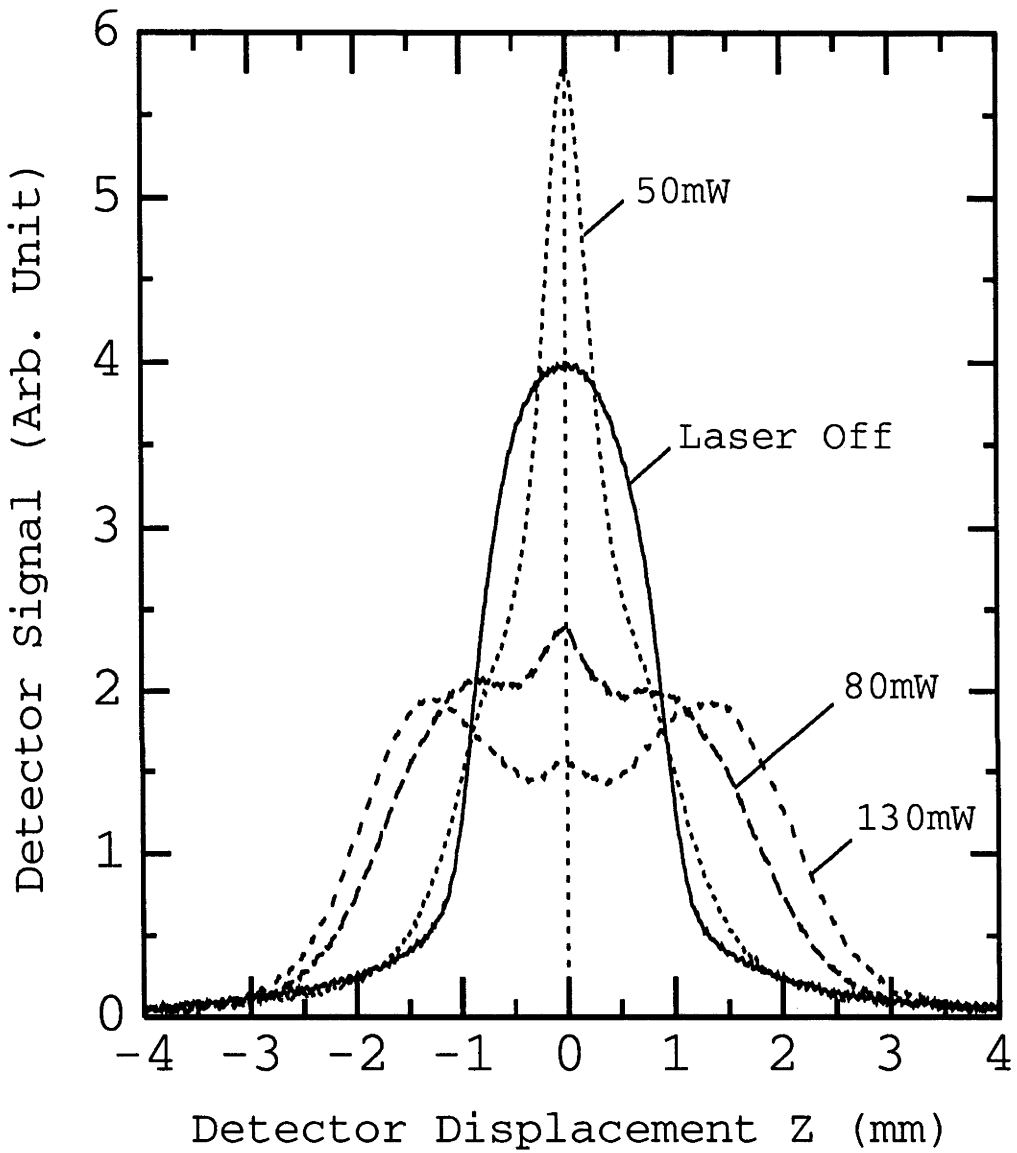


Figure 5.2: Variation of the experimental transverse spatial distribution with different interaction standing wave laser power for one longitudinal velocity (1000m/s). Other conditions are the same as for fig.5.1.

Another important feature is the small peak in the center of the spatial distribution lying between the two broad heating peaks. This central peak may be due to the two effects: collimation and focusing.

(1) The collimation is due to the channelling of atoms in the bottom of the standing wave potential for low initial transverse velocity atoms ($< 0.1m/s$), in which the heating is small for these atoms. From the force's diagram, we can see that, for small transverse velocity atoms, the smaller the velocity, the smaller the heating force. The net result is the peak in the spatial distribution which is centred about the atomic beam axis in the middle of a distribution of heated atoms.

(2) For atoms with large initial transverse velocity ($> 0.1m/s$ and $< v_c$), there is a large increase of the transverse velocity within the standing wave potential and the heating force becomes more important than that of atoms with small transverse velocity. As soon as the transverse kinetic energy of the atoms is larger than the potential energy of the standing wave, the atoms will escape and keep the sign of the transverse velocity. So the atoms can have two output directions: v_e and $-v_e$. The atoms with transverse velocity $-v_e$ will be focused to the atomic beam axis. The details of the focusing of atoms onto the atomic beam axis will be discussed in Chapter 6.

These central peaks are much more pronounced in the longitudinal velocity resolved profiles presented here than were the peaks observed in the longitudinal velocity integrated profiles in Refs[66, 67, 68, 69].

5.3 Simulation of The Experimental Results

The atomic beam was represented by an one-dimensional ensemble of atoms with identical longitudinal velocity originating from a source with width equal to the oven diameter (In our experiment, the diameter of the oven nozzle was $0.35mm$). This width was in turn divided into a series of sources one half wavelength in extent to make use of the repetitive structure provided by the standing wave. It was found that 250 source points per $\lambda/2$ were required to give sufficient statistical smoothness to the results. The results of calculations for the $\lambda/2$ sources could then be summed, allowing for the displacement of each $\lambda/2$ source in the transverse (z) direction. The resulting spatial distribution was then convoluted with the $60\mu m$ instrumental resolution of the detection system to allow comparison with the

experimental profiles.

The experimental beam divergence was simulated by calculating a range of transverse velocities which were weighted so that the spatial distribution at the detector position exactly matched the experimental spatial profile in the absence of the standing wave. The weighting used for each source point are the same.

Both the continued fraction model (see subsection 2.7.2) and the $F_0 + \text{gradient}$ ($F_0 + \text{Eq.2.81}$) force model are used to simulate the spatial profiles. The simulation results were compared with the experimental results.

The simulation was performed for two regimes. The first regime was to simulate the behavior of atoms in a strong standing wave with small detuning ($\leq 100\text{MHz}$) and the other regime was for large detuning ($\geq 500\text{MHz}$).

5.3.1 Small Detuning $|\Omega|/2\pi \leq 100\text{MHz}$

The simulation of the atomic profiles was using the v_t^{in} and v_t^{out} velocity tables (e.g. fig.3.9) and Eq.3.13, the final transverse spatial distribution can then be calculated. The Experimental results are compared in detail in fig.5.3 with the theoretical models, with separate calculations being presented for each of the velocity groups shown in fig.5.1.

In these calculations, the value of G_0 used is that which best fits the qualitative appearance of the experimental spatial profiles (full width and shoulder height). Under the circumstances, the experimental ($G_0 = 120 \pm 30$) and the model ($G_0 = 140$) values are not significantly different. Note that at the intensities used, the Rabi frequency is large compared to the hyperfine level separations. If the standing wave is not perfect circularly polarized beam, the standing wave laser can interact with a lot of other hyperfine levels of sodium atoms which will increase the discrepancy between the experimental and simulation results.

It is clear from fig.5.3 that the $F_0 + \text{gradient}$ force model is able to reproduce the effects of heating, but not the central peak caused by channelling (except for a small effect at 1300m/s). On the other hand, the continued fraction calculations predict both the heating and the formation of a central peak. Although the central peak in the experimental curves is not as large as the continued fraction simulation suggests, it is clear that the $F_0 + \text{gradient}$ force model alone is insufficient to explain

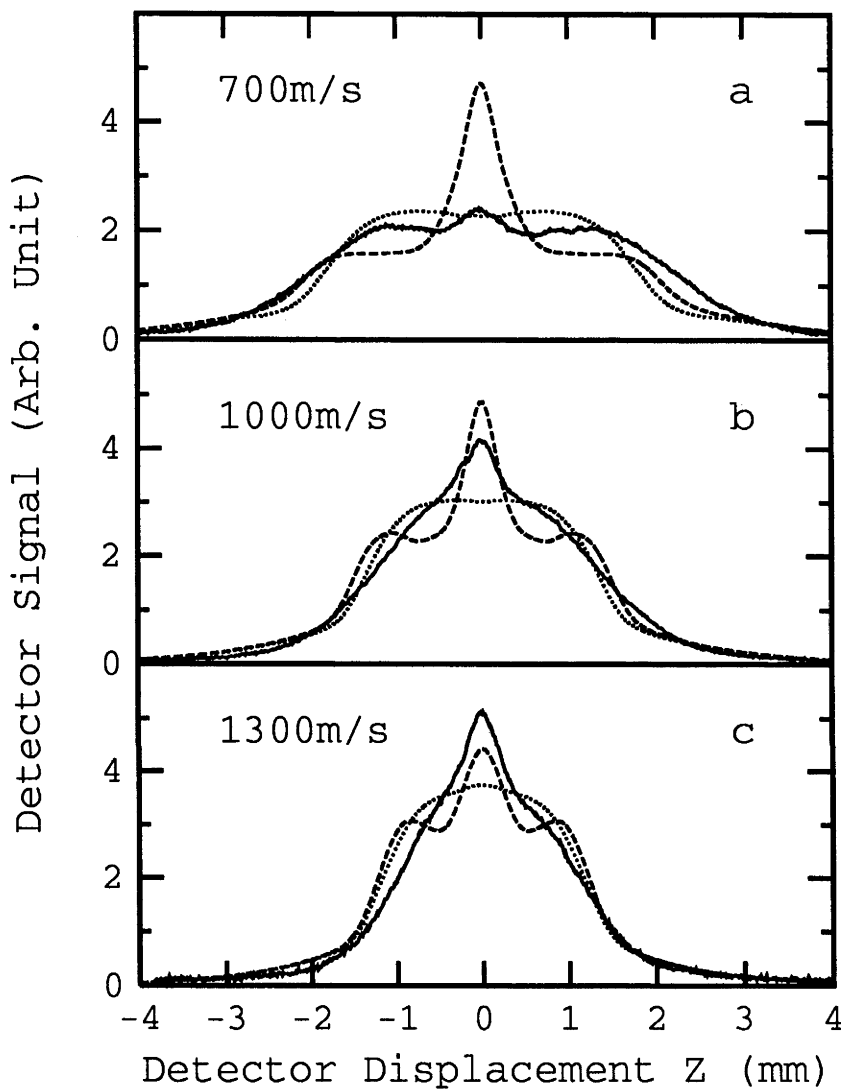


Figure 5.3: Comparison of the experimental spatial profiles (solid lines) for the three velocity groups and conditions the same as in fig.5.1, with the continued fraction model (dashed lines), and the F_0 +gradient force model (dotted lines). The value of G_0 used in the calculations was 140 (c.f. 120 ± 30 in the experiment) to give the best fit to the experimental profiles.

the form of the observed results. The different results from the two models may be expected from the velocity calculations presented in fig.3.11, which indicates the significantly lower average final velocities for small initial velocities predicted by the continued fraction model.

However, it is clear that the size of the central peak in the experiments is not as great as would be expected from the continued fraction method. This discrepancy is particularly evident for the low velocity case in fig.5.3a, while the continued fraction model simulates the experimentally observed peak much better at higher velocities. This effect cannot be explained by smoothing of the spatial distribution by the finite spatial resolution, source size or velocity resolution, which yield an instrumental resolution that is negligible on the transverse distance scale shown on the experimental spatial profiles. Neither can it be explained by rapid motion of the standing wave position, whose vibration frequency was monitored using the Michelson interferometer and a spectrum analyzer.

On the other hand, the effects of diffusion [59, 72, 22] have been omitted in these simulations due to limitations in computation time and the complexity of the diffusion processes. Diffusion is important at small detunings for atoms with small transverse velocities[72] which would normally be channelled. For our experimental parameters, the diameter of the standing wave was 4.2mm which corresponding to about $5\mu\text{s}$ transit time through the standing wave for atoms with 1000m/s longitudinal velocity. There were about 300 spontaneous emissions during this time and the transverse velocity spread due to the spontaneous diffusion was about $\sqrt{300}v_r = 0.5\text{m/s}$ which corresponding to $0.5 \times 710/1000.0 = 0.35\text{mm}$ spread on the spatial distribution for a particular $v_l = 1000\text{m/s}$, where $v_r = 0.03\text{m/s}$ is the recoil velocity of atoms. This transverse spatial distribution spread was smaller than the width of the central peak region in our results (about $0.7 \sim 1.0\text{mm}$). The stimulated diffusion is larger than the spontaneous emission diffusion (see earlier discussion on section 3.5) and if the stimulated diffusion process was taken into account, the transverse spatial distribution spread may be much larger than 0.35mm which could account for the width of the experimental peak.

Furthermore, the spread in velocity space due to diffusion will be accelerated by the heating process. Diffusion would also be expected to play a more important role over longer interaction times[72], which is consistent with the greater discrepancy between the experimental and continued fraction results at lower longitudinal

velocities. Hence the diminished magnitude of the central peak in the experiments compared to the continued fraction model is most likely the result of diffusion processes.

5.3.2 Large Detuning $|\Omega|/2\pi \geq 500\text{MHz}$

Diffusion would be expected to play a less significant role at larger detunings[59, 72]. In addition, transverse heating would also be expected to be negligible as illustrated by fig.3.6, where the spatially averaged heating term F_0 is extremely small compared to the first order term F_1^s . To investigate this, a series of spatial profiles for large detunings ranging from -0.5GHz to -5.5GHz in steps of -1.0GHz is shown in fig.5.4 for a fixed longitudinal velocity (1000m/s) and intensity ($I = 100\text{mW}$). Note that the experimental profiles in fig.5.4 have not been normalised by area, having been measured during one experimental run under the same conditions.

Central peaks in the spatial distribution were again observed, but were much more pronounced than the peaks shown for smaller detunings in fig.5.1 and fig.5.2. In particular, for a detuning of -0.5GHz , the central peak is nearly twice the size of the peak of the distribution at -5.5GHz (which at such a large detuning approximates the spatial distribution with the laser off).

A model calculation using the continued fraction solution yields the theoretical curve shown in fig.5.4 and produces close agreement with the experimental data. The first step in the simulation was to calculate the output transverse velocity of atoms from the standing wave as a function of input transverse velocity with the longitudinal velocity fixed to be 1000m/s . The $v_{in} - v_{out}$ results for a single source point are shown in fig.5.5. Apparently, when the detuning is increased, the potential of the standing wave decreases and the escape velocity decreases. At these large detunings, the continued fraction model is dominated by the first order sine term (see fig.3.6), with negligible contribution from the heating term F_0 (Note the straight line for velocities greater than the critical velocity in fig.5.5). Since the spontaneous emission rate would be expected to be extremely low, and consequently “Sisyphus” heating would be expected to be negligible. Consequently, a calculation (not shown) using the gradient force alone yields identical results to the continued fraction model, since at these large detunings $F_0 \approx 0$ and both models can be approximated by a purely sinusoidal potential.

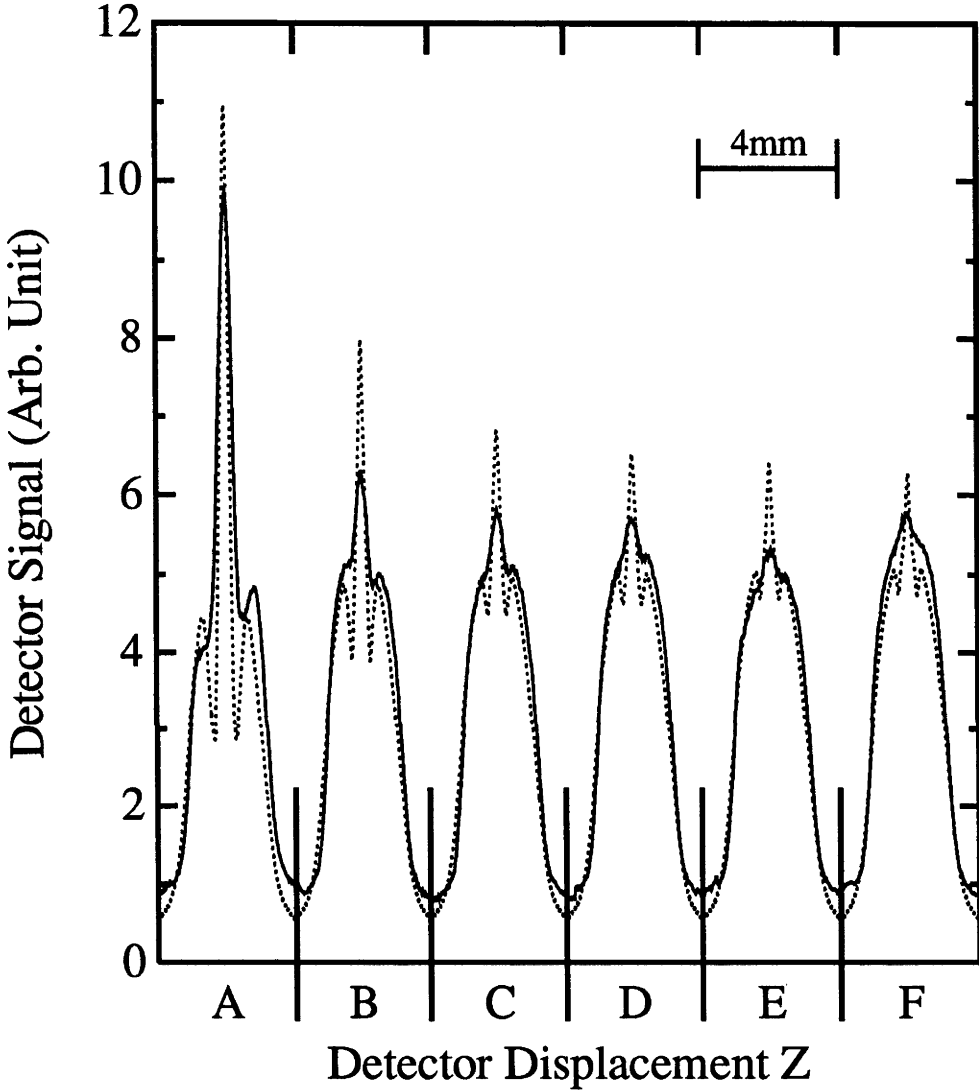


Figure 5.4: *Experimental transverse spatial profiles (solid lines) for detunings from $A = -0.5\text{GHz}$ to $F = -5.5\text{GHz}$ in -1.0GHz increments, compared with the continued fraction model (dashed line; the same simulated result was produced using the gradient force model). Here $v_l = 1000\text{m/s}$, $P = 100\text{mW}$, and $G_0 = 140$ in the model calculations. The model profiles have all been scaled vertically by the same amount to yield the best fit with the experimental profiles.*

The improved agreement between the experimental and simulated profiles at the large detunings in fig.5.4 (when compared with the small detuning used in fig.5.3) suggests that the discrepancy at small detunings is most likely the result of diffusion. The lower spontaneous emission rate at large detunings reduces the effect of spontaneous diffusion, which in any case is negligible (due to saturation) when compared to fluctuation of the dipole forces at large G . The stimulated diffusion coefficient for $\Omega \gg \omega_R$ is proportional to Ω^{-2} [59] (or see Eq.3.17), and also diminishes in importance at the large detunings used in fig.5.4, yielding much better agreement between the simulations and experiment. It is this systematic qualitative improvement in the agreement between the simulations and experiment under conditions where diffusion would be expected to be less important (both for small and large detunings) that suggests any discrepancy is due to diffusion processes. (see fig.3.14, fig.3.15 and fig.3.16).

5.4 Summary

An experiment was performed to study the effect of a strong, near resonant, standing wave laser light field on the transverse velocity distribution of a sodium atomic beam. The laser field was detuned negatively with respect to the atomic transition in order to distinguish the effects of light forces which lead to transverse heating and channeling/focusing of the atoms. (For positive detuning, the effects of cooling, channeling and focusing were mixed and only one central peak was observed). In order to separate the contributions of the longitudinal and transverse velocity contributions to the far field spatial beam profile, a velocity sensitive detection system was used to select particular longitudinal velocity groups with high resolution.

It was shown that at low detunings, the experimental spatial distribution caused by the interaction of the atomic beam with the standing wave could best be explained using the full continued fraction model. Although both models reproduced the heating of the beam for atoms with higher transverse velocities, the observed central peak of atoms with lower transverse velocities is not reproduced by the (zero velocity) gradient force model. The systematic improvement in agreement between the continued fraction model and the experimental spatial profiles under conditions where the effects of diffusion would be expected to be less important suggests that diffusion was responsible for the differences between simulation and experiment which were more noticeable at small detunings.

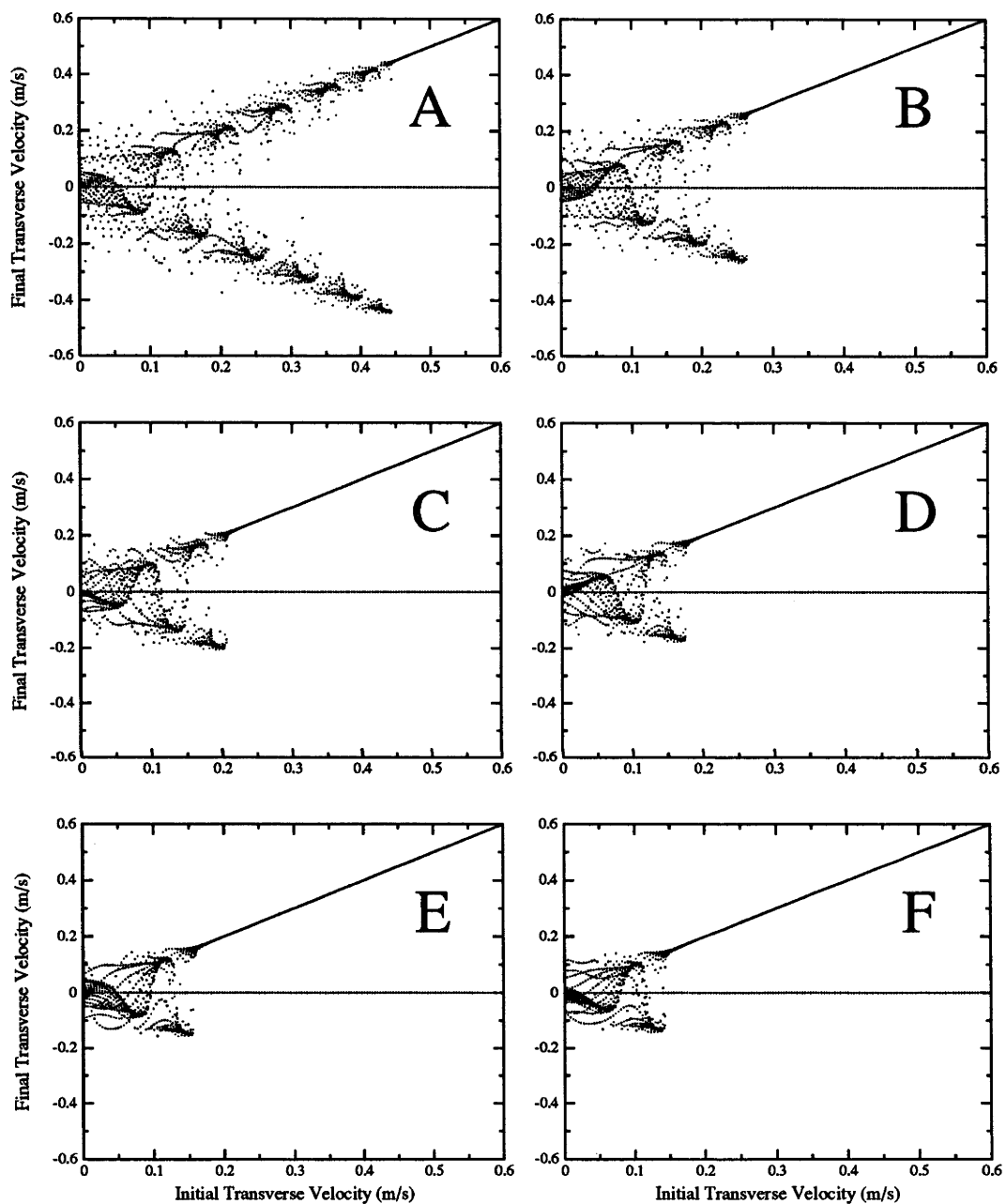


Figure 5.5: Plot of the final transverse velocity as a function of initial transverse velocity for a single source point under condition of $G_0 = 140$, $v_l = 1000 \text{ m/s}$ for detuning from A = -0.5 GHz to F = -5.5 GHz in increments of -1.0 GHz .

In the next chapter, the emphasis will be put on the channeling/focusing of an atomic beam interacting with a strong standing wave laser field.

For higher velocities ($kv_t \gg \Gamma$), the force on the atom no longer has a simple velocity dependence, and Doppleron resonances become important. This effect will be discussed in Chapter 7

Chapter 6

Focusing (Zoom-Lens) and Collimation of Atoms

In Chapter 5, we found from the experiments that there was a large peak in the center of the transverse atomic beam profile. In this chapter we will investigate this central peak in details and compare the experimental results with the theoretical simulation.

6.1 Review

Considering the perpendicular interaction of atoms with a standing wave, under the condition that the transverse kinetic energy component of the atoms along the standing wave axis is lower than the maximum potential energy (channelling condition), they will be forced to execute oscillating trajectories along the nodes of the potential (see fig.3.7 and fig.3.8). These atoms will leave the potential either forward scattered or specularly reflected with respect to the nodal planes, leading to the focusing of the reflected atoms which we can see easily from fig.3.9. In case the force is conservative (for example, at large detunings) which can be described using the simple gradient expression (Eq.2.81), the magnitude of the output velocity will be the same as that of the input velocity. Atoms with a transverse kinetic energy component higher than the maximum potential energy of the standing wave will leave the potential undeflected. The atoms which are channelled and reflected (i.e. the negative branch in fig.5.5A) will be focused to one point on the atomic axis located at a distance from the standing wave equal to the distance from the atomic source. The standing wave acts like a 1 : 1 imaging system for these atoms. This

1 : 1 imaging phenomenon was observed experimentally in Ref.[47].

When the detuning is reduced, from fig.3.6 and fig.3.7 we can see that the force can no longer be described by the conservative gradient force Eq.2.81. The spatial averaged force of the continued fraction solution becomes important and this force depends strongly on the transverse velocity and is no longer conservative which means that the absolute value of the output transverse velocity will be different to the input transverse velocity. Fig.3.9 shows the output transverse velocity as a function of input transverse velocity and from this figure we can see some remarkable results: the output velocity is certainly increased in magnitude (heating for negative detuning) and oscillates between positive and negative values. Almost half the atoms experience heating and are accelerated away from the atomic axis. The other half are accelerated towards the atomic beam axis. Since v_{out}/v_{in} is only roughly constant, the image is spread along the z axis, due to the range of v_{in} . Thus the focusing of atoms is **chromatic**. The atoms are again focussed as in the conservative potential case, but this time with an image ratio less than 1 : 1 for small negative detunings (for small positive detuning, this ratio will be larger than 1 : 1). One could describe this as an atomic lens with variable focal length, determined by the detunings and the intensity of the standing wave laser field.

This kind of zoom-lens focal property of the imaging of atoms had not been reported before. In our experiments, we have, for the first time, observed evidence which shows the changing of the focal length of the atoms under different conditions (detuning, intensity and different interaction position). In this chapter, we will present the experimental results related to such kind of focus property of an atomic beam and the theoretical simulation using the continued fraction solution of the results will be given.

6.2 Experimental Arrangements and Procedures

The experimental arrangements are almost the same as presented in Chapter 4 (fig.4.2). However, here the intensity of the standing wave was increased. The higher the intensity of the standing wave, the higher the force, the larger the capture transverse velocity and the higher the central peak. In this experiment, in order to increase the peak intensity of the standing wave laser field, the standing wave laser beam was collimated by a telescope system and the diameter ($1/e$ point of the

maximum intensity) of the laser beam was collimated to $1.6 \pm 0.2\text{mm}$.

This time, the 1mm diameter circular skimmer just in front of the standing wave field was substituted by a rectangular mask (see fig.6.1). This rectangular mask was formed by two slits: one slit was placed vertical and the other was placed horizontally. The size of the fixed vertical slit was about 0.3mm allowing the atomic beam to only interact with the central uniform region of the standing wave laser beam (The diameter of the standing wave laser beam in the experiment was 1.6mm which allowed 3.6% change in the standing wave laser intensity).

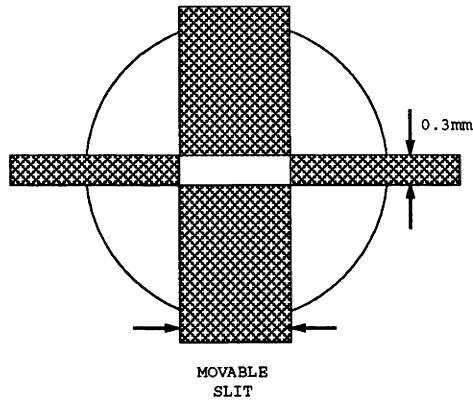


Figure 6.1: The shape of the atomic beam interacting with the standing wave was defined by a rectangular mask which was formed by two slits.

The maximum atomic beam divergence was defined by a second movable horizontal slit just in front of the standing wave. There were three horizontal slits with different sizes on a plate which was driven by a DC motor to select different maximum atomic divergence angles. The slit was movable parallel to the standing wave laser field and, in this way, we could change the angle of the atomic beam in respect to the standing wave. The simplest way to measure the focal length change of the atoms would have been to move the detector to different positions at the atomic axis to measure the spatial atomic distributions and then compare the width and peak of these measured atomic profiles. However, under present experimental conditions in our laboratory, the distance from the oven nozzle to the detector was fixed and we could not move the detector along the atomic axis, we had to perform the experiments in other ways.

The method we employed to perform this experiment was to change the interac-

tion position of the standing wave in respect to the oven nozzle in the interaction chamber. There were only three different interaction positions we could use and the distances to the oven nozzle were given in chapter 4 which were $650mm$, $720mm$ and $780mm$ downstream from the oven nozzle.

The first step in the experiment was to tune the lasers (both standing wave and detection lasers) near 5890\AA using the $He - Ne$ wavemeter in order to excite the $3^2S_{1/2} \rightarrow 3^2P_{3/2}$ resonance transition. Next, the standing wave laser wave was adjusted roughly perpendicular to the atomic beam just by eye. The largest movable slit was then placed in the atomic axis and this allowed the maximum spatial transverse atomic beam profile to be detected which made it easier to find the exact perpendicular position. The detuning of the standing wave was set about to $1GHz$ and the profile of the atomic beam in the detection chamber was monitored using the detection system. The angle of the standing wave laser field with respect to the atomic beam was changed until the narrow peak appeared at the center of the (laser off) atomic beam profile. A line between the central peak at the detector and the atomic source forms the normal to the standing wave. Then the slit was moved so that it was centered around the central peak with atomic profile. At this stage, the laser beam was assumed in the near exact perpendicular position to the atomic beam and the error was within $0.13mrad$ (see Chapter 4).

6.3 Experimental Results

Fig.6.2 shows a series of the experimental traces obtained by moving the horizontal slit in front of the standing wave. It is clear from this diagram that with the atomic beam moves from one side to another side, the central peaks stay at almost the same point. In order to observe the central peak clearly, a large slit ($3mm$) in front of the standing wave was used. From the diagram, we can see that the width of the atomic beam is about $6mm$ which is just double the width of the slit, since the distance from the oven nozzle to the detector was almost double the distance from the nozzle to the standing wave ($720 : 640mm$). The width of the slit was deliberately made large, so that the focusing effect of atoms could be observed at large angles to the standing wave.

The intensity of the laser beam forming the standing wave was $150mW$ which gives a maximum intensity parameter $G_0 = 1166$. The detuning of the standing

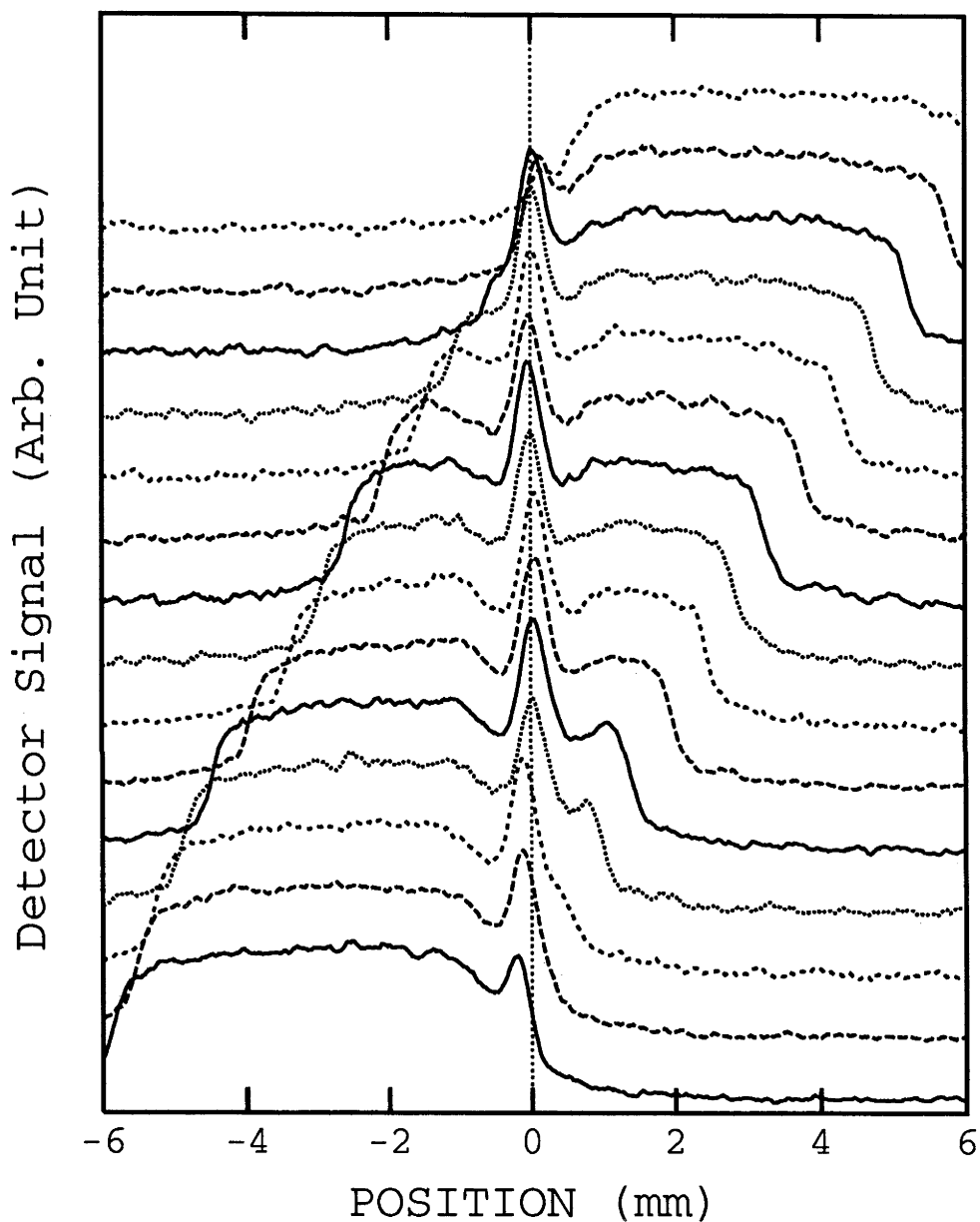


Figure 6.2: A series of the experimental traces obtained by moving the horizontal slit in front of the strong standing wave laser field. It is clear that the central peaks stay almost at the same position in the plane of the detector. The power of single beam of the standing wave was $P = 150\text{mW}$ and the detuning was $\Omega/2\pi = -1.23\text{GHz}$.

wave was set to be -1.23GHz . The distance from the oven nozzle to the standing wave was 720mm and the distance from the standing wave to the detector was 640mm . For -1.23GHz detuning, the spatial averaged force almost equals zero and only the periodic dipole force is important.

In order to observe these central peaks which appeared in the atomic-beam profiles in more detail, the expanded atomic beam profiles around the central peaks from -2mm to 1.5mm were presented in fig.6.3.

The mask of the atomic beam was moved to one side of the central focusing position (defined as ‘zero point’) in the tail of the atomic beam profile. Fig.6.4 shows the moving of the atomic-beam profiles to one side with the standing wave laser off.

Comparing this with fig.6.3 we can see that some atoms were reflected to the zero point. Initially, when the standing wave laser beam was off, there were no atoms at zero point when the mask did not cover the central focusing position. With the standing wave on, and with the mask shifted well to the left, only atoms with large transverse velocity ($v_t > 0.1\text{m/s}$) can interact with the standing wave laser field. From the negative branch of the $v_{in} - v_{out}$ curve in fig.5.5, we understand that for large detuning and large transverse velocity, the central peak was caused by the focusing of atoms. If the absolute value of output velocity v_{out} is equal to the absolute value of input velocity v_{in} , the focusing point should be the 1 : 1 image of the atomic source. From fig.6.3, the width of the peaks were almost the same as the size of the oven nozzle (0.35mm) as expected, since the nozzle and the detector distances from the standing wave are nearly 1 : 1 (720 and 640mm respectively).

It appears that the small central peak at the zero point in fig.6.3 was shifted a little to the left when the mask was moved to the left from the central zero point. This small shift was due to the size of the oven nozzle and can be explained using fig.6.7. From this figure, we can see that it is clear that when the mask is moved to one side, the peak of the atomic beam measured at the detector would also move in the same direction as the mask. Because, for fixed standing wave intensity and detuning, there was a cut-off velocity in the $v_{in} - v_{out}$ diagram, the peak height would decrease as the mask is moved away from the central focusing position and approaches the region where atoms with cut off velocity are reflected.

When the mask covers the central position, both effects: collimation and focus-

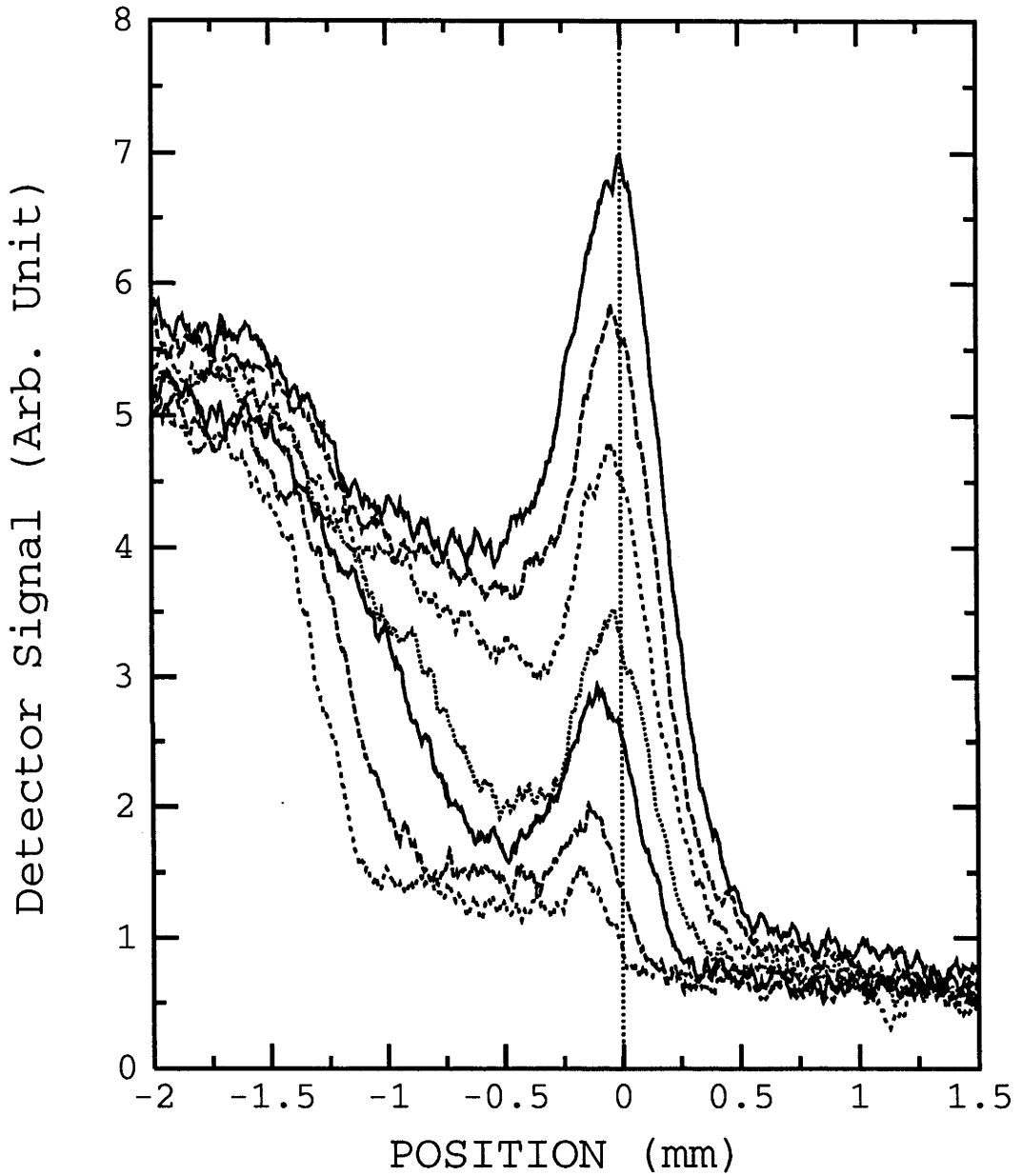


Figure 6.3: *The expanded central peaks in the tail of the atomic beam. The slit in front of the strong standing wave was moved in the negative direction. There is a small shift of the peaks to the negative direction, toward the main atomic beam. $P = 160\text{mW}$, $\Omega/2\pi = -1.3\text{GHz}$.*

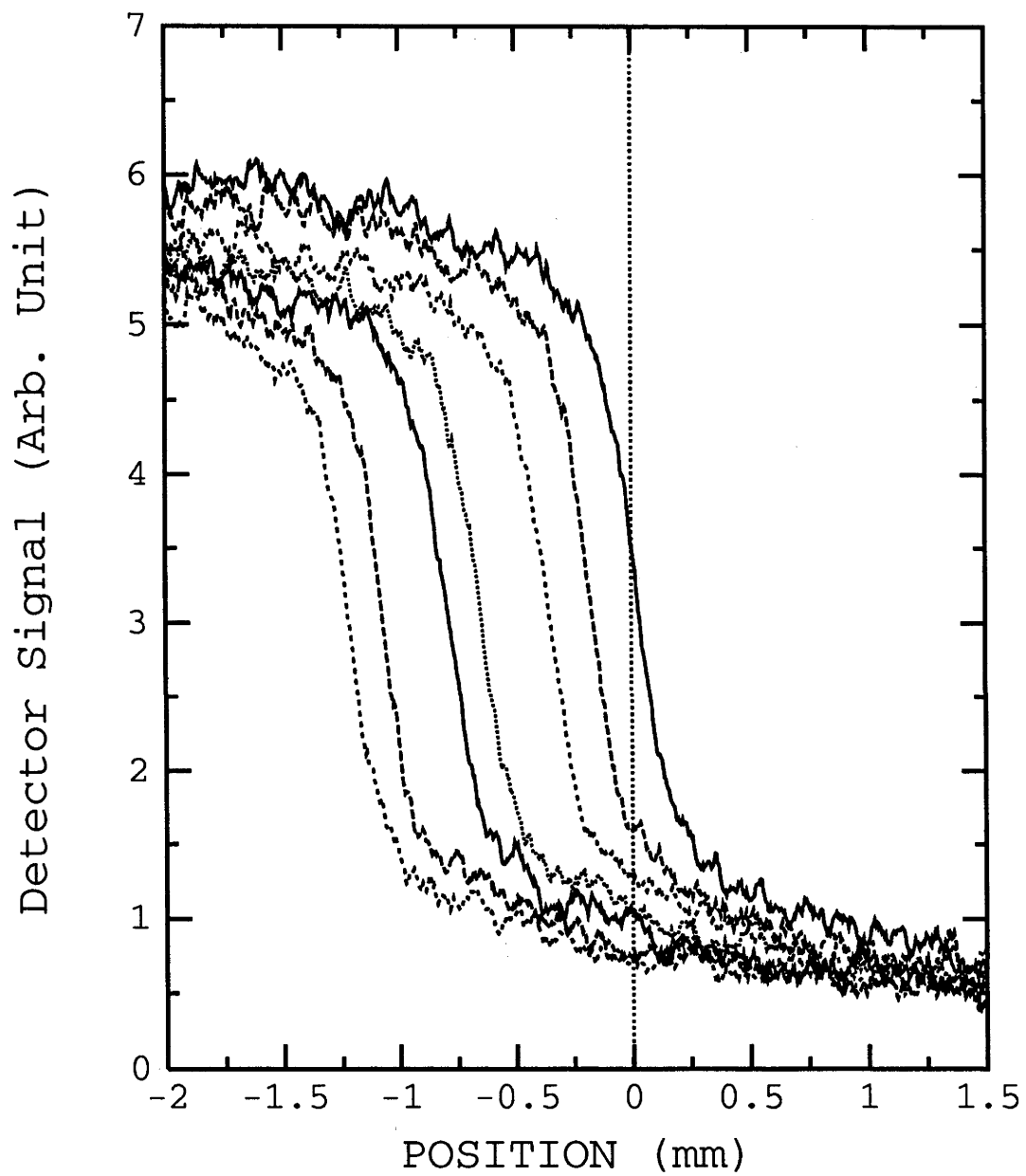


Figure 6.4: *The same measurements as in fig.6.3 with the standing wave laser beam turned off.*

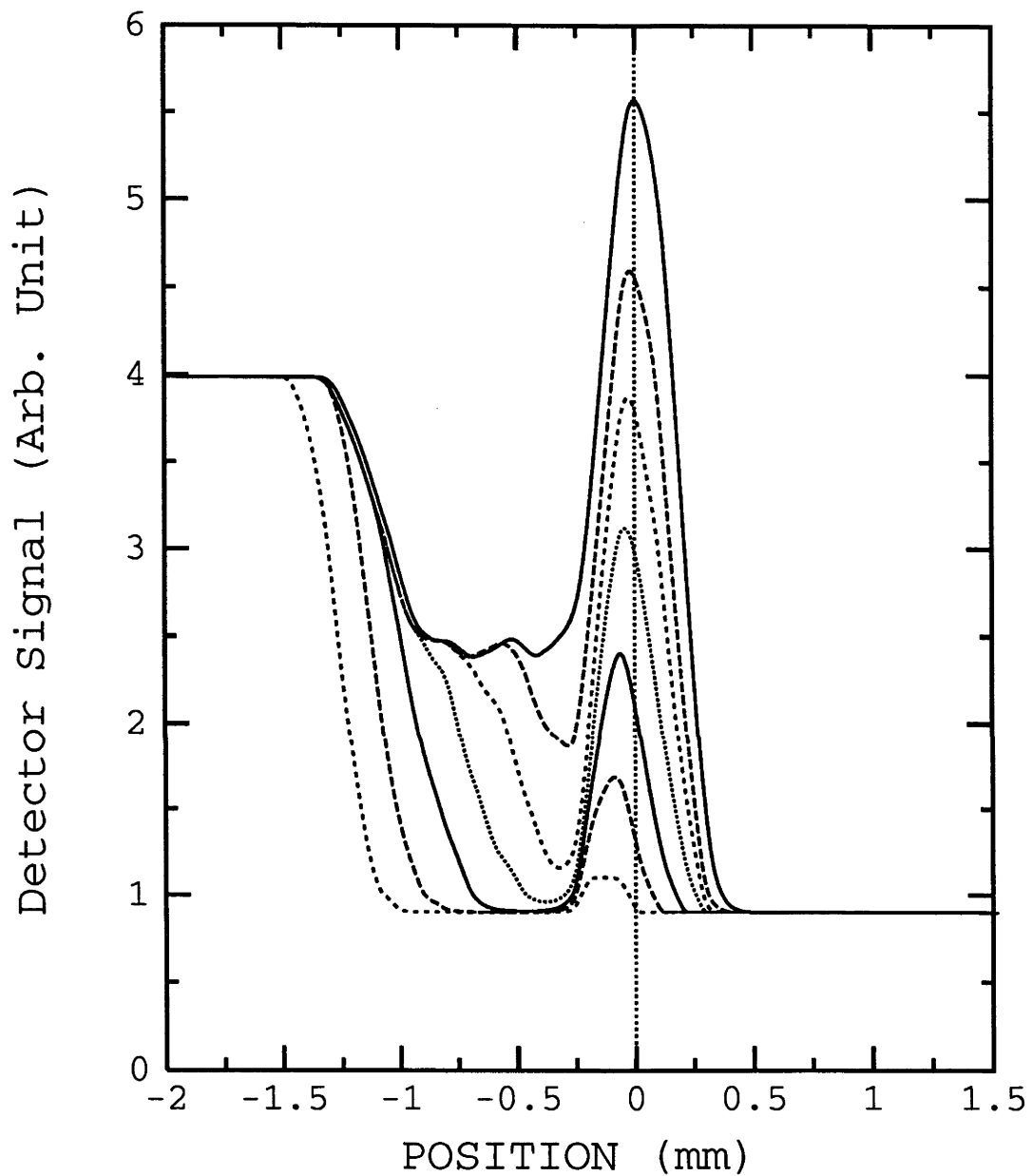


Figure 6.5: Simulation of fig.6.3 using continued fraction method. ($P = 160\text{mW}$, $\Omega = -1.3\text{GHz}$). It is clear, from the simulation, that there is small shift of the small peaks to the negative direction, toward the main atomic beam which is in good agreement with the experimental results. The small shift is caused by the size of the oven nozzle.

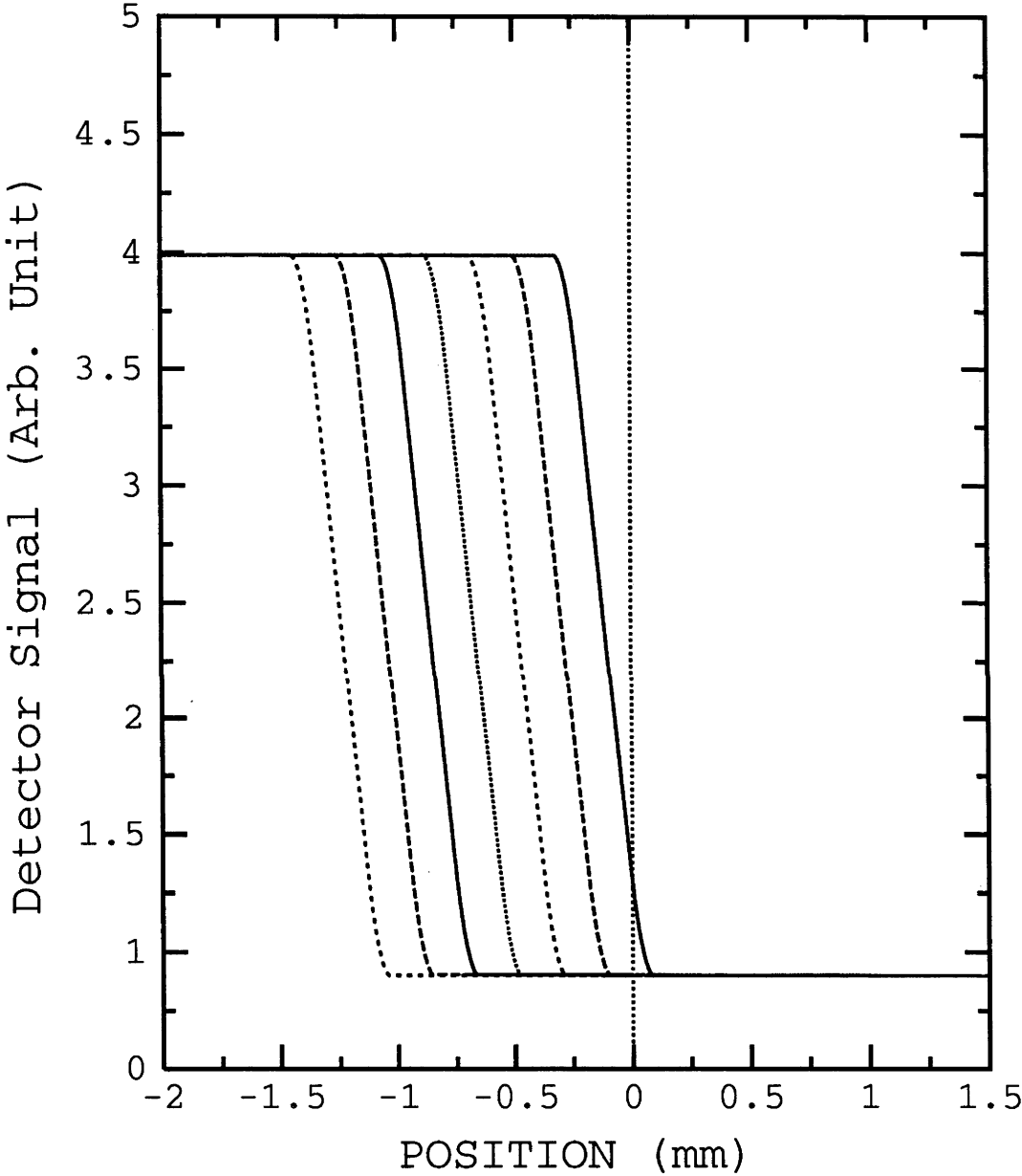


Figure 6.6: *The initial atomic beam profile used for simulation of fig.6.5.*

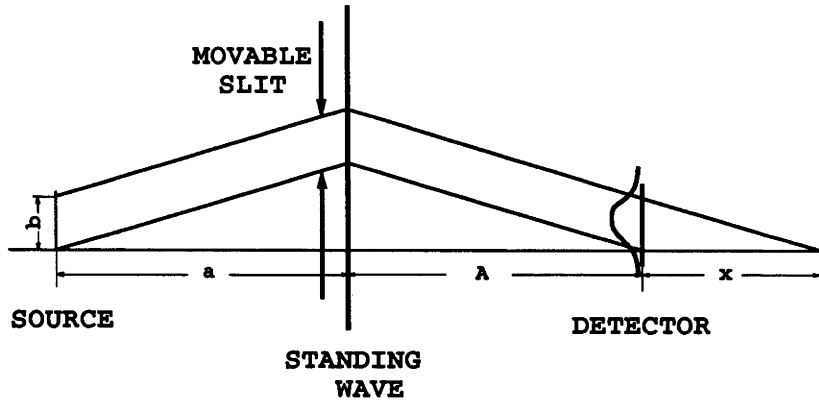


Figure 6.7: This diagram explains the small shift of the peak in fig.6.3. When the atomic beam moved upward, the peak in the detector would move upward because of the size of the atomic oven nozzle.

ing, contribute to the central peak but you can't distinguish them. When the mask moves away from the central position, the collimated atoms that run straight through the central position are blocked by the mask and only the deflected (focusing) atoms contribute to the central peak. Consequently, in the case of large detunings and large transverse velocity ($v_t > 0.1\text{m/s}$), the central peaks are mostly due to the focusing effect of atoms. At large detunings, there is no energy loss and the output energy should equal the input energy which means that the absolute values of the final transverse velocity should be the same as the initial transverse velocity. This will allow 1 : 1 focusing of atoms.

The simulation results of fig.6.3 using the continued fraction solution are shown in fig.6.5. The initial atomic beam profile (with the standing wave laser off) used in the simulation are presented in fig.6.6. The parameters used in the simulation are the same as those experimental parameters (fig.6.3). Also it is clear that, from the simulation, as the mask is moved to one side, the focused peak also shift slightly to one side toward the mask. The small shift of the small peak to one side is caused by the size of the oven nozzle. The simulation is in good agreement with the experimental results.

For small negative detunings, the problem becomes more complicated, since the spatial average force (heating effect) becomes important and the output velocity of atoms from the standing wave could be considerably larger than the input velocity. This can cause the change of the focusing position of atoms. Below we will present some experimental evidence which shows this kind of zoom-lens effect for different

laser intensities and detunings.

6.3.1 Intensity Dependence of Focusing Length of Atoms

Fig.6.8 shows a series of (five) experimental spatial profiles of the central peak for different standing wave intensities. The detector position scanning range for each profile is 3.5mm . The distance from the oven nozzle to the standing wave is 650mm and from the standing wave to the detector is 710mm . The detuning is fixed to be -240MHz for all these five profiles. From profile A to E, the power and the maximum saturation parameter G_0 of a single beam of the Gaussian standing wave lasers are as follows with 10% uncertainty

Fig.6.8	A	B	C	D	E
Power	75mW	166mW	280mW	520mW	650mW
G_0	582	1290	2176	4041	5051

It is clear from Fig.6.8 that for detuning of -240MHz , the height of the peak increases and then decreases as the intensity of the standing wave laser field increases. There are two possible explanations for this effect: the first explanation is that the decrease of the peak is possibly due to the diffusion process. The diffusion would increase as the intensity of the standing wave increases and this would decrease the number of atoms in the central area; the second explanation is based on a change of the focusing position (focusing length) of atoms. When the focusing length are changing, the size of the atomic profiles in the detector will change. If the focusing point moves away from the detector, the atoms will be spread out at in a larger spot and this reduces the detector signal in the center. As the detuning was small in this case, because of the heating effect, the capture velocity almost stayed the same when the intensity increases, and hence the peak change is caused by the shift of the focusing position.

Fig.6.9 shows another series of experimental spatial profiles of the central peak. This time, the position of the standing wave was moved 130mm toward the detector so that the distance from the oven nozzle to the standing wave became 780mm and the distance from the standing wave to the detector became 580mm . The detuning of the standing wave was -210MHz which is close to the detuning in the above experiment (fig.6.8). The power and G_0 for these five curves are shown in the

following table:

Fig.6.9	A	B	C	D	E
Power	40mW	70mW	180mW	230mW	500mW
G_0	311	544	1340	1787	3886

From this figure, we can see that when the intensity of the standing wave laser field increases, the peak always increases. We can compare fig.6.8 and fig.6.9, because the parameters (laser intensity, detuning et al.) are very close, the only significant difference between these two experiments being the different position of the standing wave. Also the diffusion effect in these two cases should be the same. From these two experimental results, we conclude that the height change of the central peak as function of intensity of the standing wave was caused by the focusing length change of the atoms and not the diffusion processes. If they are caused by the diffusion processes, a decrease of the peaks as function of laser intensity in fig.6.9 would be expected and, in contrast, the experimental results showed increase of the peaks.

The results in fig.6.8 and fig.6.9 can be explained by using fig.6.10. In fig.6.10(a), the ratio of the distance from the oven nozzle to the standing wave to the distance from the standing wave to the detector is $650\text{mm} : 710\text{mm}$ and the detector is close to the $1 : 1$ focusing point. For a small negative detuning, when the intensity of the standing wave laser field increases, the absolute value of output velocity will increase due to heating and the focusing position will move toward the standing wave. Hence the peak height would be expected to reach a maximum and then decrease.

In fig.6.10(a), for low intensity of the standing wave (say 75mW in fig.6.8), the atoms were focused near the $1 : 1$ position; when the intensity increases, the focusing position would move toward the standing wave and closer to the detector which would increase the peak. The peak was maximum for a critical intensity P_c when the focusing length was just the same as the distance from the standing wave to the detector.

When the intensity of the standing wave was higher than P_c , the focusing length would become less than the distance from standing wave to the detector and the peak would always decrease. The closer to the standing wave of the focusing point,

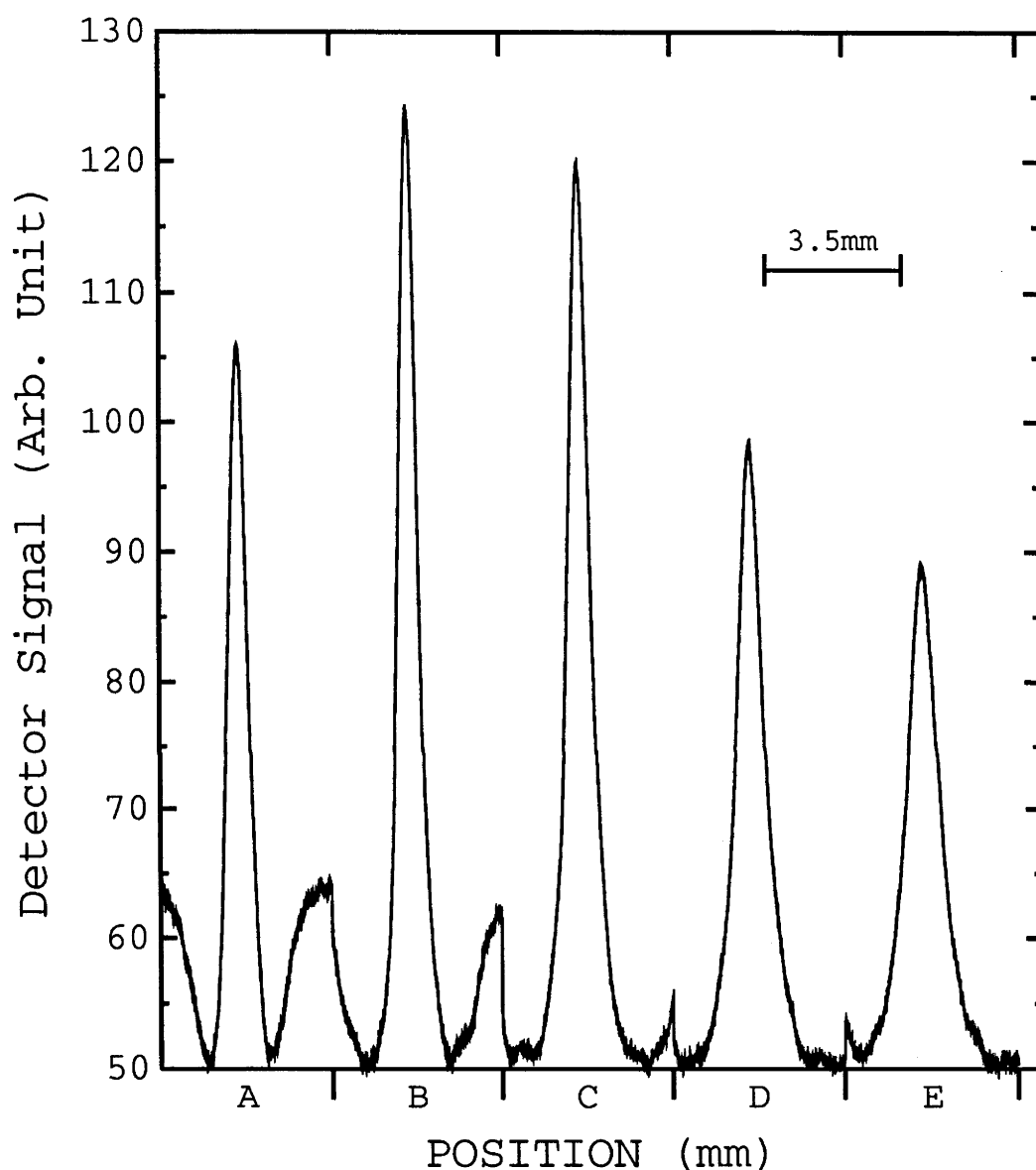


Figure 6.8: A series records of the central peaks as a function of the intensity of the strong standing wave laser field. The detuning was fixed to be -240MHz and the powers for these five curves are 75, 166, 280, 520 and 650mW. The ratio of the distance between the oven nozzle and the standing wave to the distance between the standing wave and the detector is 650 : 710mm. The detector scanning range for each curve is 3.5mm.

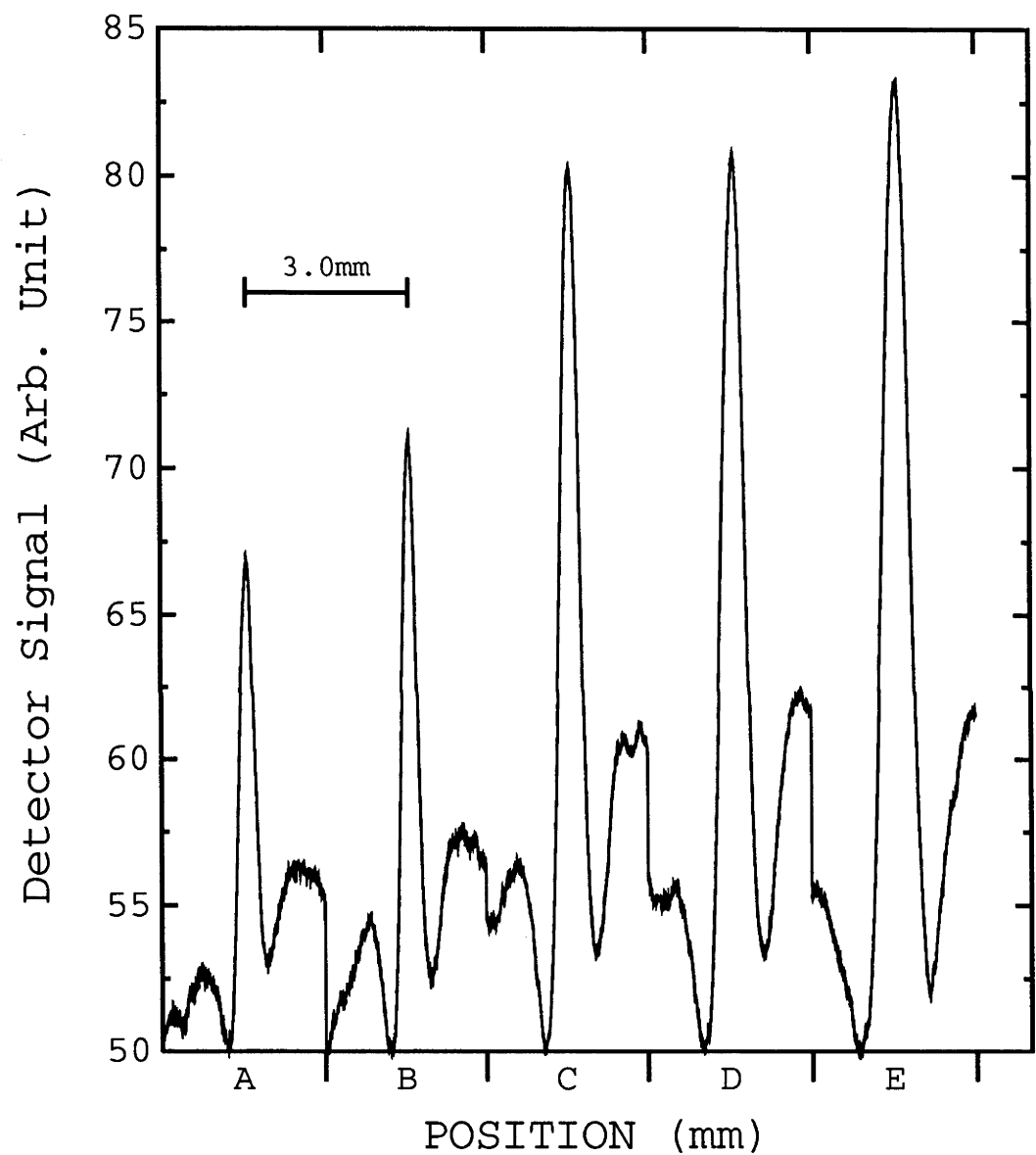


Figure 6.9: These five curves were recorded under different ratio of the distances, 780 : 580mm. The detuning was set to be -210MHz and the intensities were 40, 70, 180, 230 and 500mW . The detector scanning range for each curve is 3.0mm.

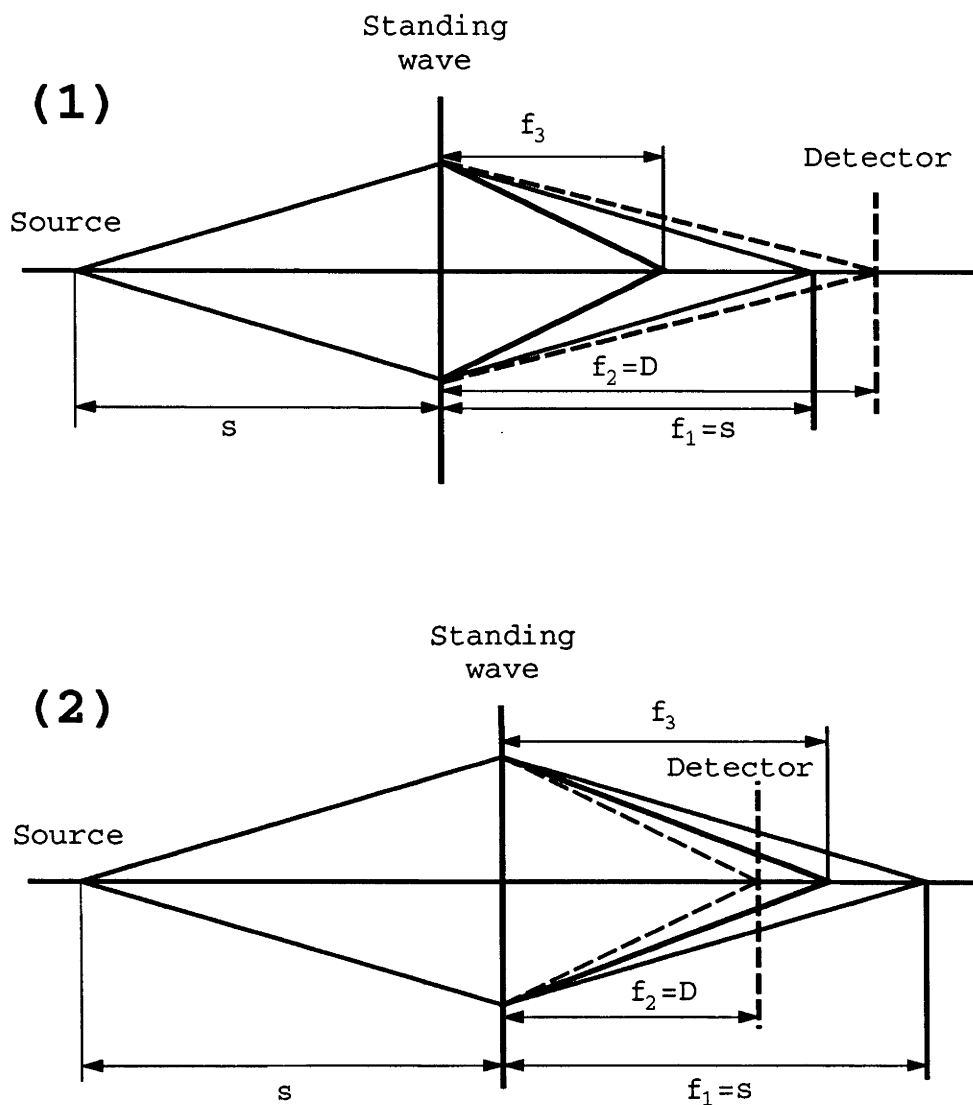


Figure 6.10: Explanation of the focusing length changing (zoom-lens) of the atoms. f_1 is 1 : 1 focusing position, $f_2 = D$ is the detector position and f_3 is the actual focusing position from the standing wave. (1) corresponding to 650 : 710mm. (2) corresponding to 780 : 580mm. It appears that in case (2), more power was needed to focus the atoms to the detector position.

the smaller the detector signal of the central peak because the increases of the focal spot size.

In fig.6.10(b), this ratio is $780mm : 580mm$ and the detector is close to the standing wave, far away from the $1 : 1$ focusing position. Hence, the critical intensity of the standing wave P_c was much larger than that in fig.6.10(a). If the intensity of the standing wave was less than P_c , the increase of the intensity would only increase the central peak of the atomic profile. Certainly, if the intensity in fig.6.9 was high enough, the peaks were expected to decrease again.

The above experimental evidence supports the interpretation of a ‘zoom-lens’ of standing wave laser field acting on atoms. In the following subsection, the height change of the central peaks as function of standing wave intensity will be used to further verify the zoom-lens focusing.

6.3.2 Detuning Dependence of Focusing Length of Atoms

In the above section, we discussed the intensity dependence of the central focusing peak. In this section, we will present some experimental results about the change of the central focusing peak as function of the detuning of the standing wave laser field. The distance ratio was the same as in fig.6.8 ($650mm : 710mm$)

Fig.6.11 shows the same results as in fig.6.8 except that the detuning here was $-1050MHz$. The power and the corresponding saturation parameters for these five curve are shown as follows:

Fig.6.11	A	B	C	D	E
Power	75mW	125mW	260mW	510mW	650mW
G_0	582	972	2021	3963	5051

Although in this case the detector was put beyond the $1 : 1$ focusing position, from this figure, we can still see the critical intensity P_c which is much larger than that in fig.6.8. This can be explained by the fact that when the intensity of the standing wave increases, the increase rate of the spatial averaged heating force F_0 is much slower than that of the harmonic forces (F_1^s and F_1^c). In the small velocity regime ($kv_t \ll \Gamma$), for fixed intensity of the standing wave, when the detuning increases, the force that an atom experiences in the standing wave will decrease.

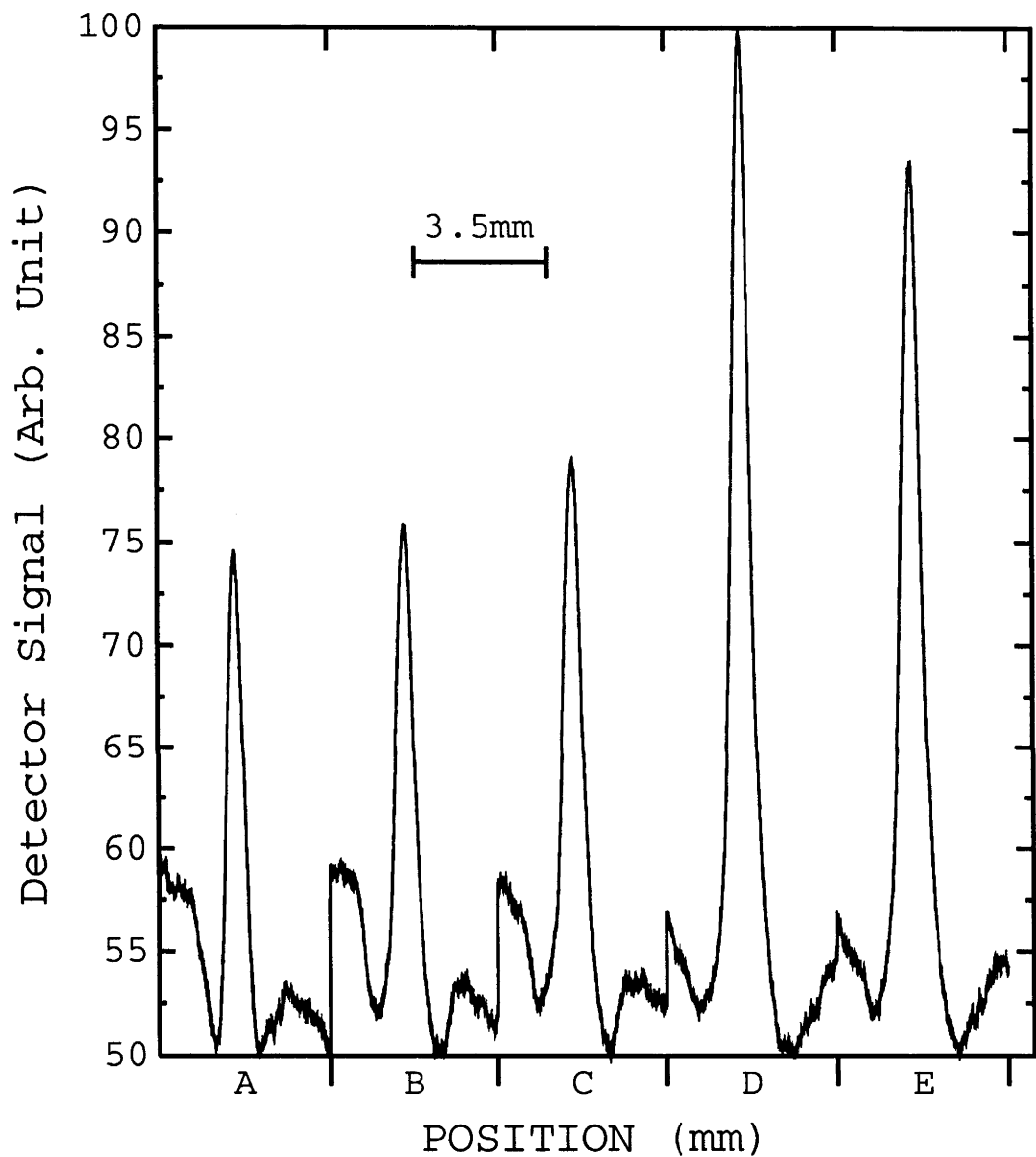


Figure 6.11: *The same result as fig.6.8, but with different detuning (-1050MHz) of the standing wave laser field.*

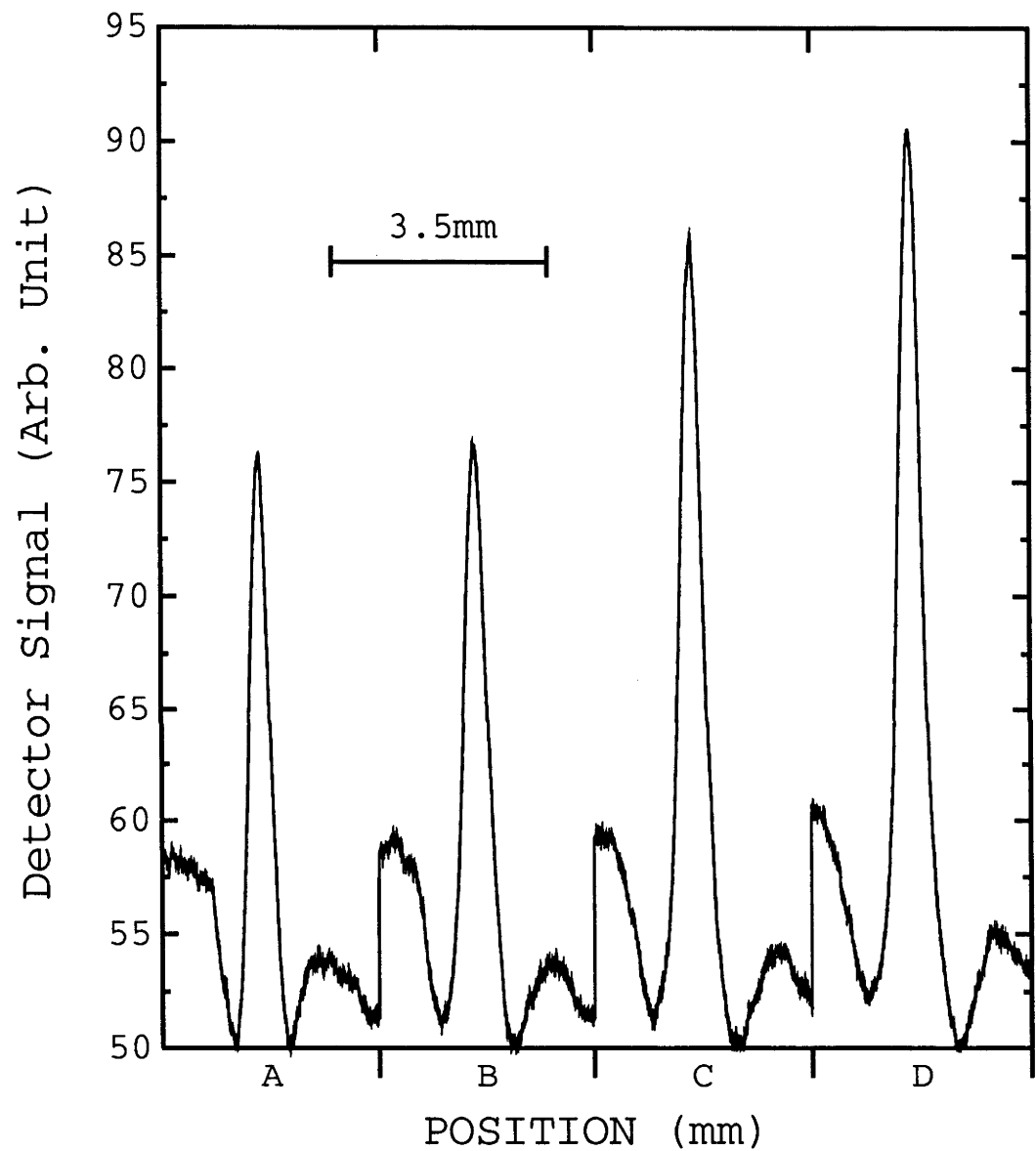


Figure 6.12: *The same result as fig.6.8, but with different detuning (-1960MHz) of the standing wave laser field.*

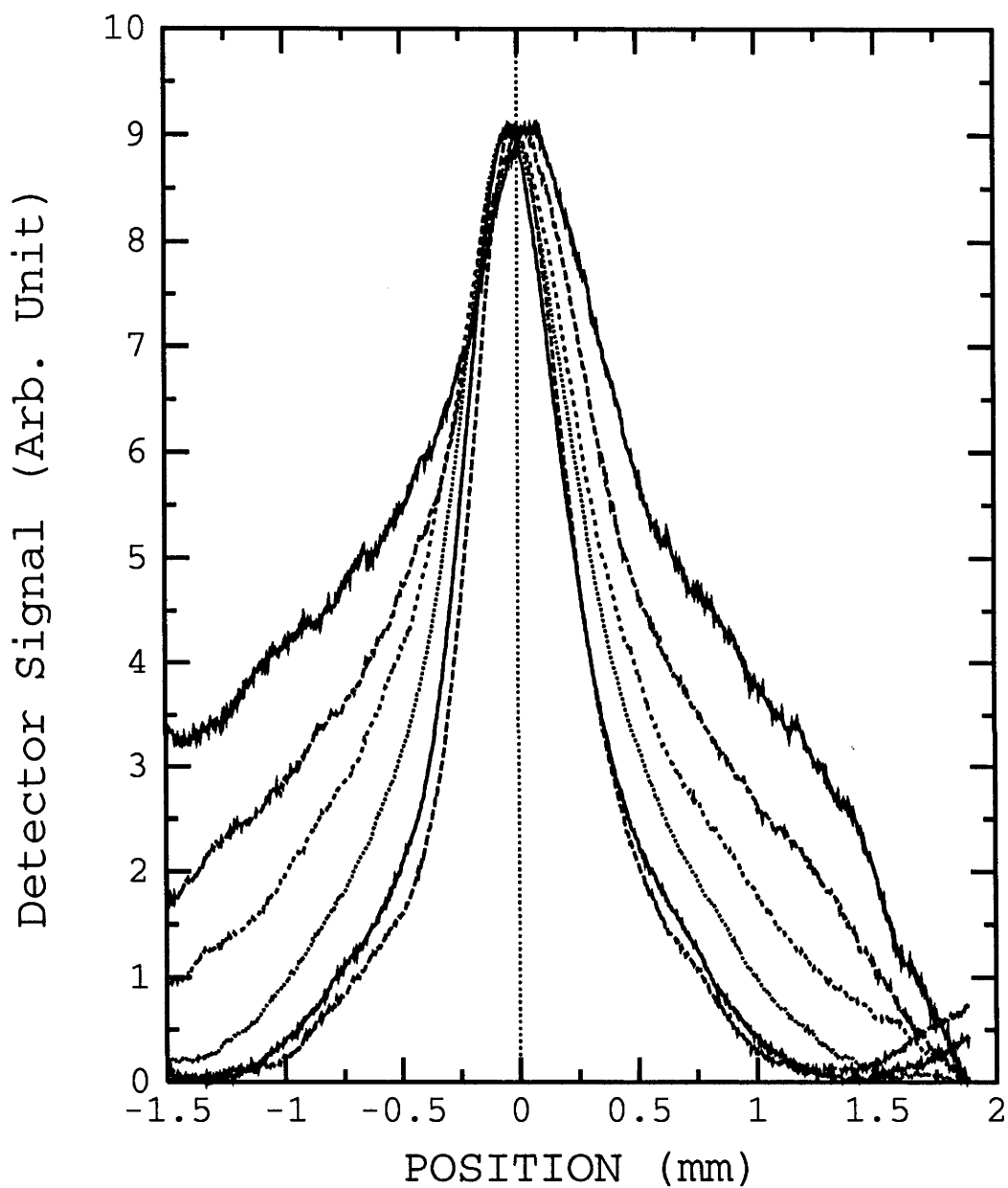


Figure 6.13: Variation of the experimental transverse central atomic beam spatial distribution with detuning of the standing wave laser for $P = 650\text{mW}$. The detunings for these six curves (from the widest to narrowest) are $+120\text{MHz}$, $+180\text{MHz}$, $+245\text{MHz}$, $+350\text{MHz}$, $+430\text{MHz}$, $+470\text{MHz}$.

Fig.6.12 shows the results with large detuning -1960MHz of the standing wave. We can see from this figure that there is no decrease of the peak height. This is because, for large detunings, the heating force equals zero and the total force is conservative, leading to 1 : 1 type focusing. The potential of the standing wave (or the transverse capture velocity) increases for large intensities of the standing wave and hence atoms with large transverse velocity will be specularly reflected to the atomic axis. So the peak height in the focusing point grows when the intensity of the standing wave increases. The following table shows the experimental parameters in fig.6.12

Fig.6.12	A	B	C	D
Power	125mW	260mW	510mW	650mW
G_0	971	2020	3963	5051

Fig.6.13 shows the experimental results of broadening of the central peak for small detunings. The power of the standing wave is 650mW which corresponds to the central saturation parameter $G_0 = 5051$. The detunings for these six curves (from the widest to the narrowest) are $+120\text{MHz}$, $+180\text{MHz}$, $+245\text{MHz}$, $+350\text{MHz}$, $+430\text{MHz}$ and $+470\text{MHz}$.

This figure shows that the smaller the detuning, the broader the curve. There are two factors which would broaden the atomic profiles. The first is due to the diffusion process which increases when the detuning decreases. The second factor is due to the change of the focal length. If the focal point of the atomic beam moved away from the detector (e.g. by changing the detuning or the intensity of the standing wave), the size of the focal spot would increase (the same as light focused by lens). The central peak sits on top of a large uniform background created by unaffected atoms (see the broad shoulders in fig.6.2). For the case of small detunings, both the central peak and the background are reduced by the optical pumping. Consequently, it is impossible to compare the area of the central peaks at different detunings in fig.6.13. As the optical pumping rate is the same for all of the focused atoms, it is reasonable to normalize these curves to the same height to eliminate the effect of optical pumping to compare the width of the central peaks.

In fact, the simplest way to measure the change of the focal spot is to move the detector along the atomic beam axis. But in our experimental apparatus, the

distance from the source of the atomic beam to the detector was fixed and it was impossible for us to move the detector.

6.4 Simulation Results

A model calculation using the continued fraction solution yields the theoretical spatial profiles as a function of detuning of the standing wave which are shown in fig.6.14 to fig.6.19. In fig.6.14, the detuning used was -240MHz which was the same parameters as one of the experiments and the peak saturation parameters were changed from $G_0 = 100$ (curve *A*) to 1300 (curve *I*) in increments of 150. In the other figures, the detunings were fixed and the maximum saturation parameters were changed from $G_0 = 100$ (curve *A*) to 2500 (curve *I*) in 300 increments. The diameter of the standing wave was 1.6mm . In each figure, the results are given for two different distance ratios used in the experiments: the ratios for (1) was $650\text{mm} : 710\text{mm}$ and for (2) was $780\text{mm} : 580\text{mm}$.

It is clear from the simulation, that for small detuning of the standing wave (see fig.6.15), the peaks first increase and then decrease with increasing standing wave intensity (G). In addition, there is an increase in the width of the peaks. When the detuning of the standing wave increases, the critical intensity P_c increases. If the position of the interaction standing wave is moved closer to the detector, P_c also increases which means a higher intensity of the standing wave is needed to focus the atoms to a shorter focusing length.

All the simulation results of the peak height as a function of detuning and intensity of the standing wave were in agreement with the experimental results. But the peak saturation parameters required in the simulation were different from the experimental parameters. The intensity of the standing wave in the experiments was about 4 times larger than the simulation parameters.

This difference between the experimental and theoretical intensities is probably caused mainly by the multi-level system of Na atoms. In our simulation, the force was calculated based on the two-level system. In the actual experiments, although some methods (for example, the use of circularly polarized laser beams, adding a small magnetic field etc.) were used to form a two-level system, it still was not possible to form a perfect two-level system in the actual experimental condition. For multi-level atoms, there are several energy levels in the excited states. Because

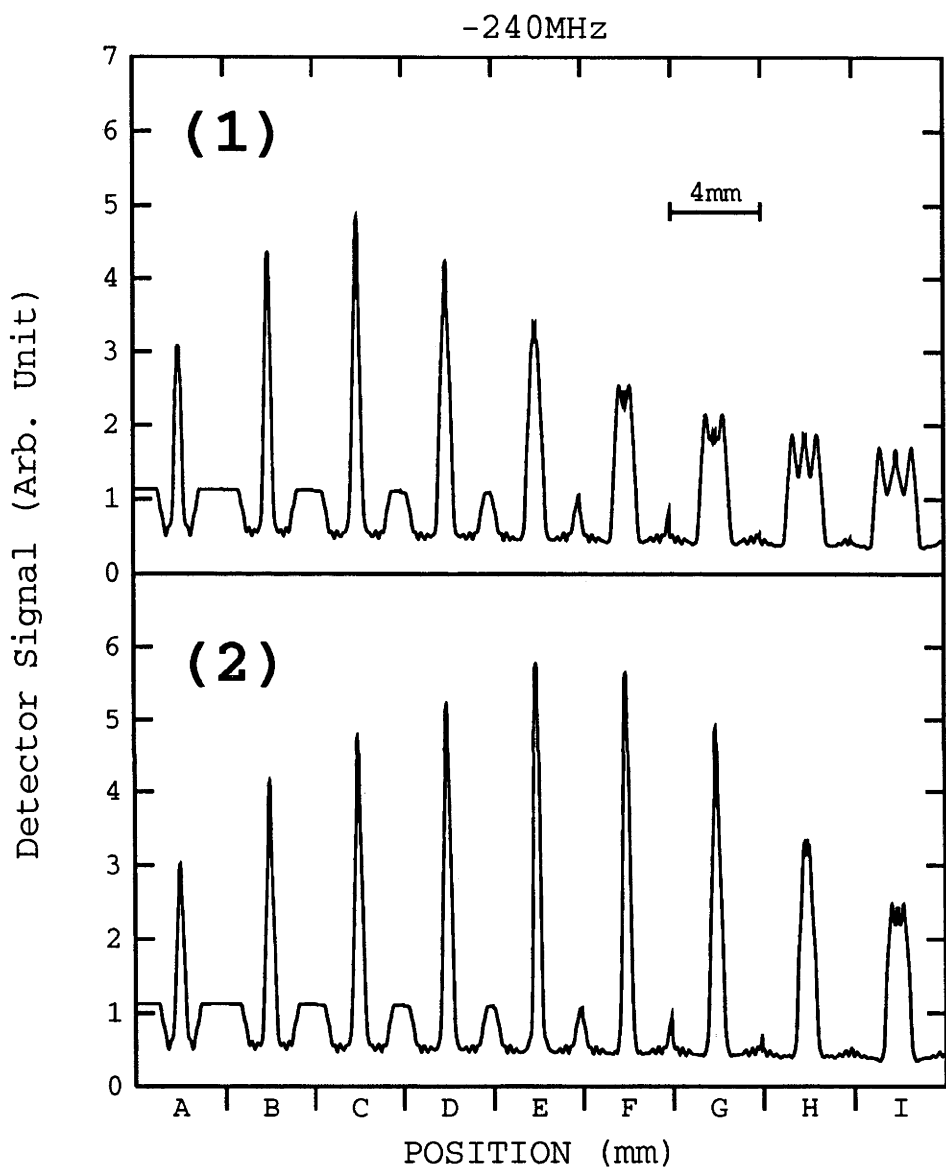


Figure 6.14: Simulation of focusing of an atomic beam as function of standing wave laser intensity. The detuning is -240MHz and for the maximum saturation parameters from $G_0 = 100$ (curve A) to 1300 (curve I) in increments of 150 . The distance ratios from the oven nozzle to the standing wave and from the standing wave to the detector are: (1) $650 : 710$; (2) $780 : 580$.

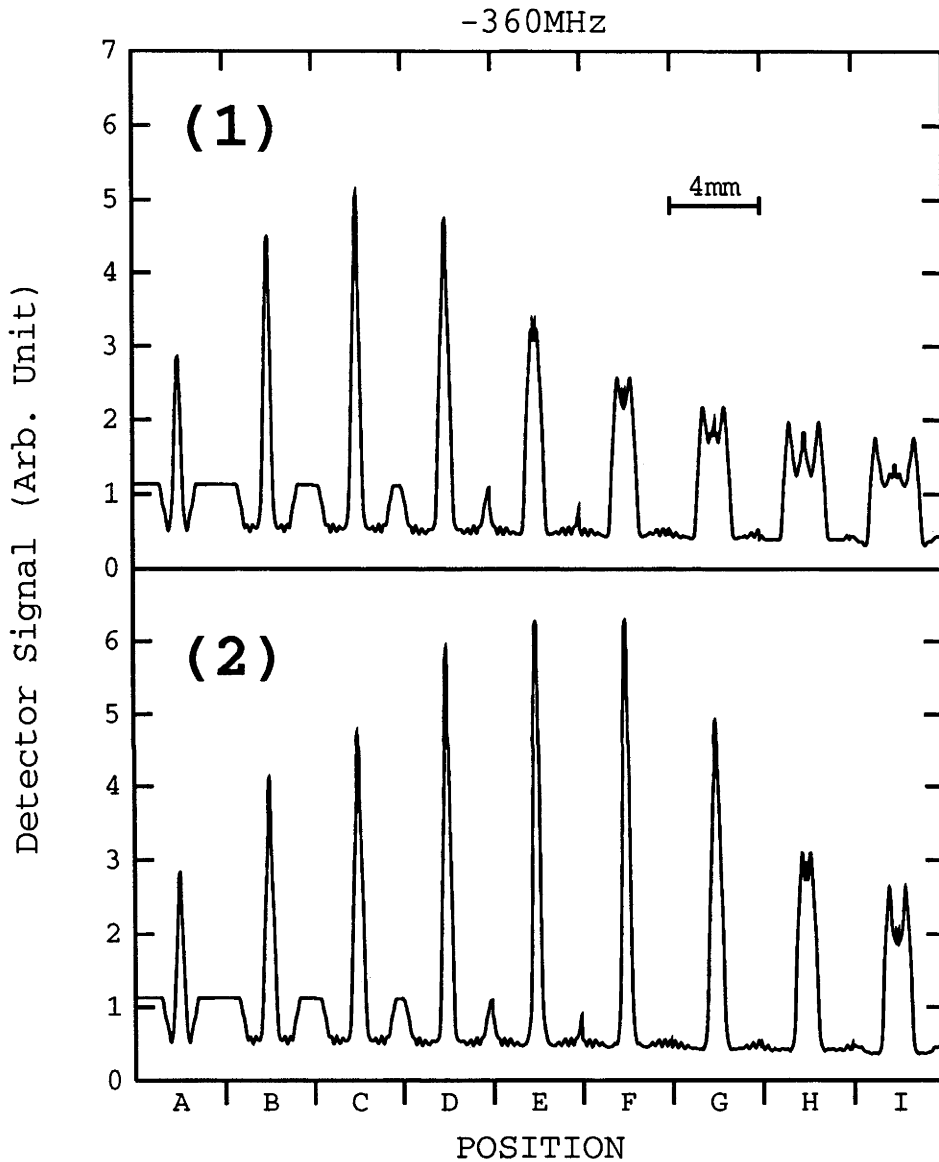


Figure 6.15: Simulation of focusing of an atomic beam as function of standing wave laser intensity. The detuning is -360MHz and for the maximum saturation parameters from $G_0 = 100$ (curve A) to 2500 (curve I) in increments of 300. The distance ratios from the oven nozzle to the standing wave and from the standing wave to the detector are: (1) $s : f_2 = 650 : 710$; (2) $s : f_2 = 780 : 580$.

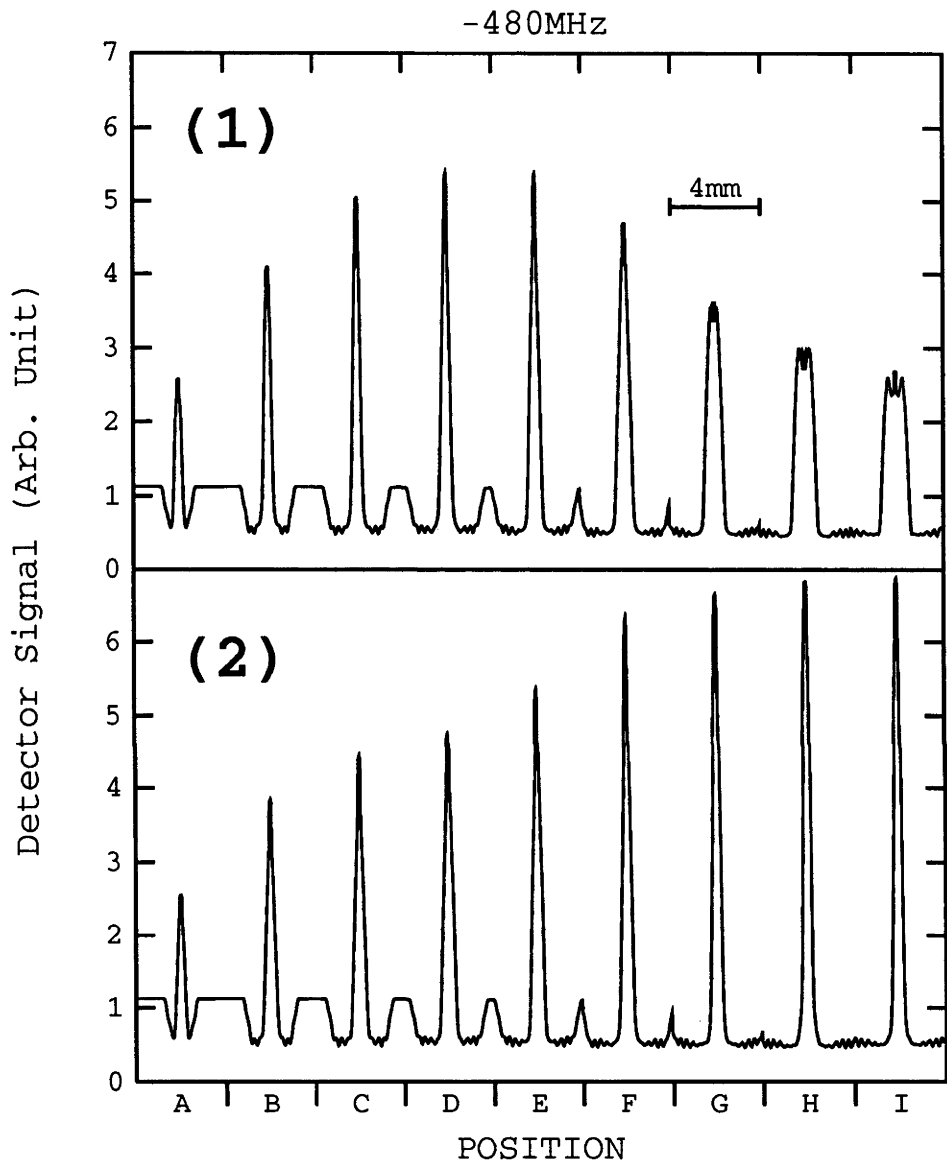


Figure 6.16: Simulation of focusing of an atomic beam as function of standing wave laser intensity. The detuning is -480MHz and for the maximum saturation parameters from $G_0 = 100$ (curve A) to 2500 (curve I) in increments of 300. The distance ratios from the oven nozzle to the standing wave and from the standing wave to the detector are: (1) 650 : 710; (2) 780 : 580.

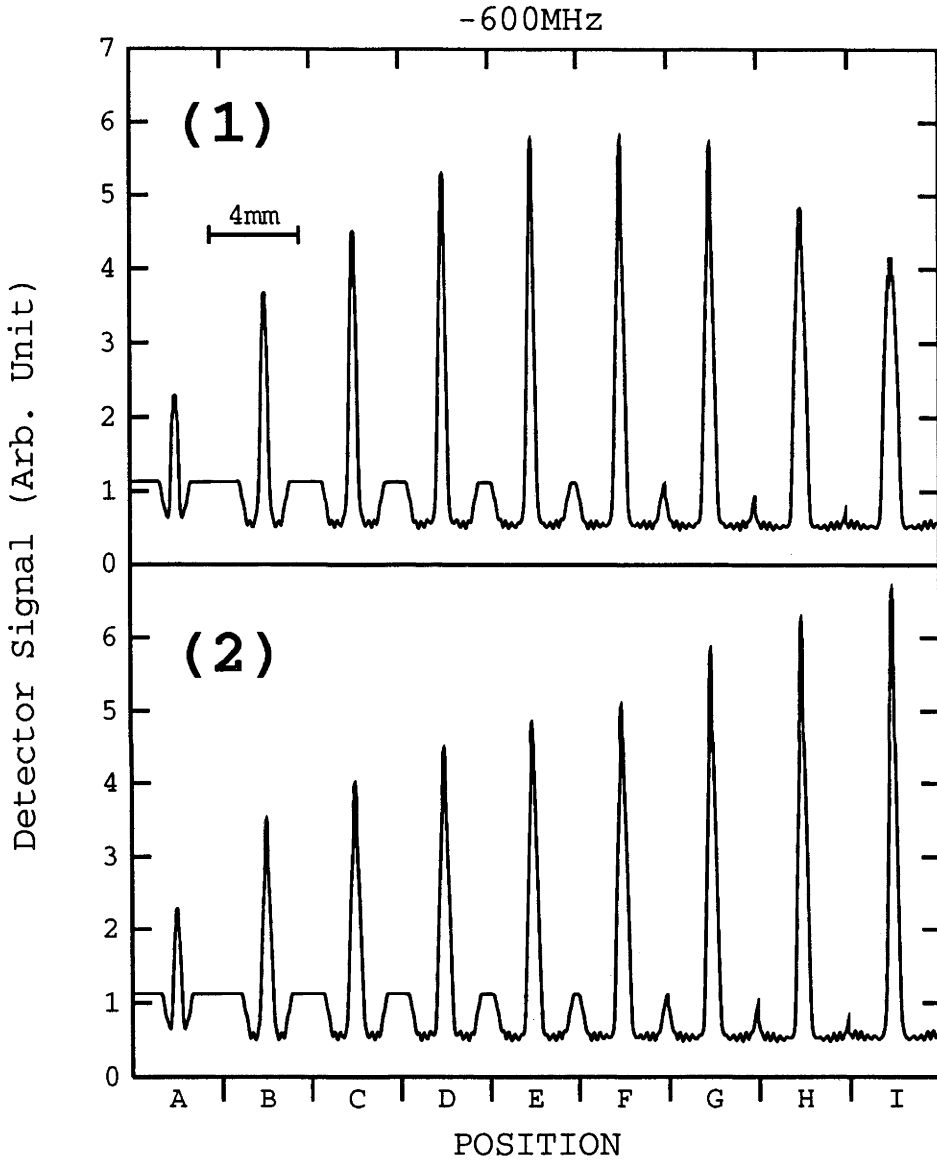


Figure 6.17: Simulation of focusing of an atomic beam as function of standing wave laser intensity. The detuning is -600MHz and for the maximum saturation parameters from $G_0 = 100$ (curve A) to 2500 (curve I) in increments of 300. The distance ratios from the oven nozzle to the standing wave and from the standing wave to the detector are: (1) 650 : 710; (2) 780 : 580.

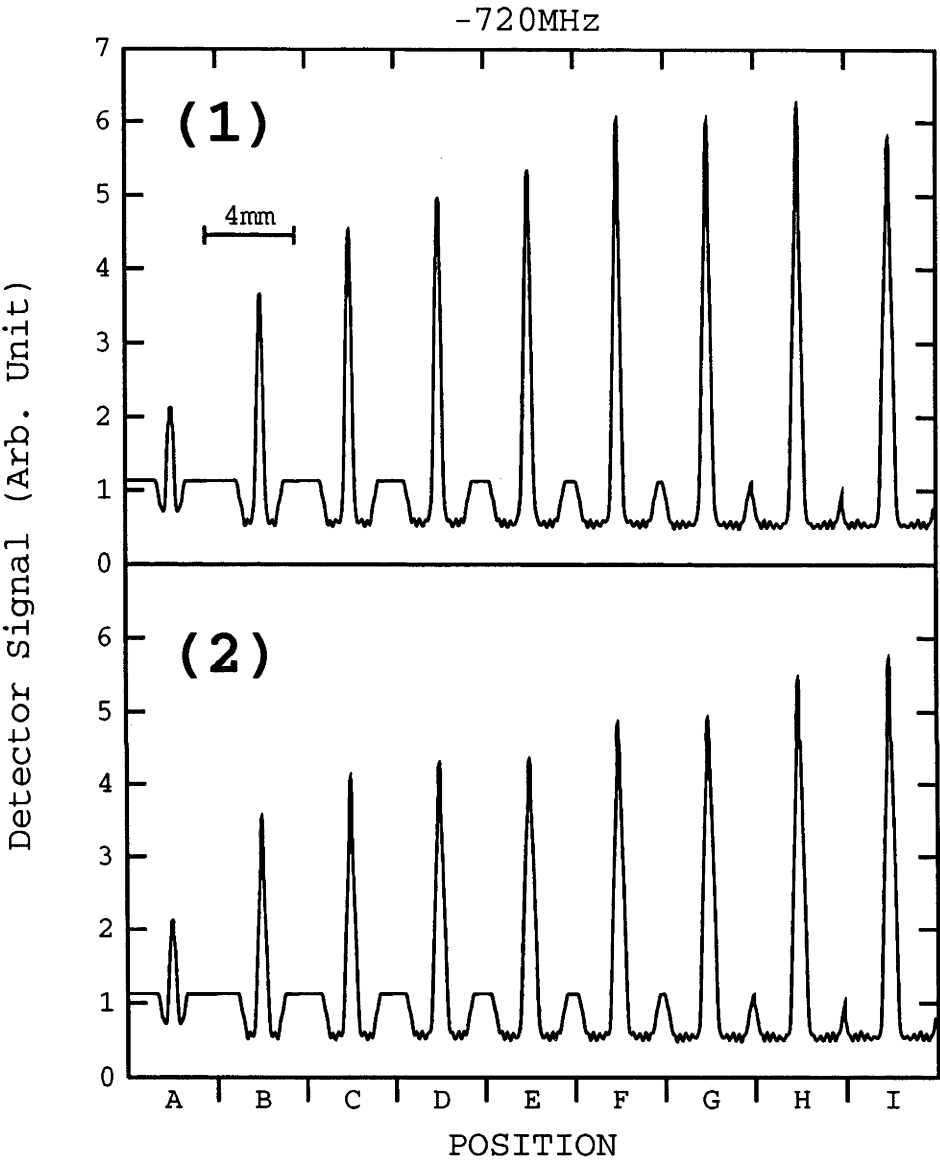


Figure 6.18: Simulation of focusing of an atomic beam as function of standing wave laser intensity. The detuning is -720MHz and for the maximum saturation parameters from $G_0 = 100$ (curve A) to 2500 (curve I) in increments of 300 . The distance ratios from the oven nozzle to the standing wave and from the standing wave to the detector are: (1) $650 : 710$; (2) $780 : 580$.

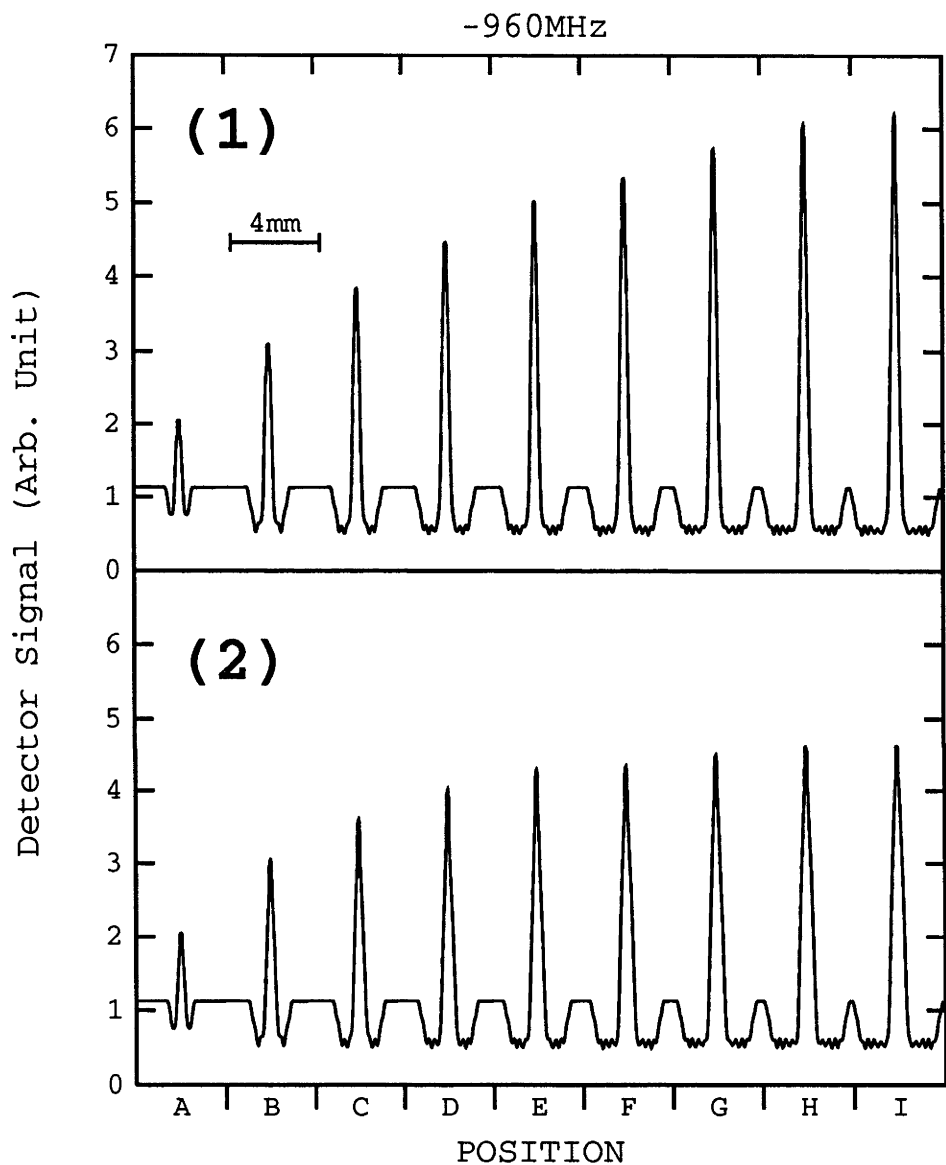


Figure 6.19: Simulation of focusing of an atomic beam as function of standing wave laser intensity. The detuning is -960MHz and for the maximum saturation parameters from $G_0 = 100$ (curve A) to 2500 (curve I) in increments of 300 . The distance ratios from the oven nozzle to the standing wave and from the standing wave to the detector are: (1) $650 : 710$; (2) $780 : 580$.

of the competition between these excited levels, more power is needed to saturate the multi-level atoms. The saturation intensity I_s for multi-level system should be larger than two-level system ($> 6.4 \text{ mW/cm}^2$ for sodium atoms) and, hence in order to get the same results, the experimental peak saturation parameter $G_0^e = I/I_s^e$ for the multi-level atoms should be larger than the theoretical peak saturation parameter $G_0^t = I/I_s^t$ of ideal two-level system (because $I_s^e > I_s^t$).

This is the possible explanation for the discrepancy between the experimental and theoretical results.

In Chapter 5, the theoretical parameters (detuning and intensity of the standing wave) were selected to match the experimental heating effect (to match the shoulder of the atomic spatial profile), while the central peak (caused by both collimation and focusing) was not taken into account. We found that both experimental and theoretical parameters matched well.

In this chapter, we concentrated on the central peaks rather than the heating effect. Because the central peaks were formed by both collimation and focusing, it is very difficult to determine the right theoretical parameters and, hence the discrepancy between the theoretical and experimental results were larger than those in Chapter 5. As the method for calculating the force is semi-classical, the nonlinear effect would become large if the intensity of the standing wave laser field is very high. Consequently the higher the intensity of the standing wave, the larger the nonlinear effect should be and a larger discrepancy would appear between the theoretical and experimental parameters.

6.5 Summary

The central peak was investigated both on experiments and simulation. We found that the peak was formed mainly by two effects: collimation and focusing. For small atomic transverse velocity (say $v_t < 0.1 \text{ m/s}$ under our experimental parameters), the atoms are channelled in the bottom of the standing wave which results in collimation in the central area (e.g. $v_{in} \sim v_{out}$ figures). For a large atomic transverse velocity ($v_t > 0.1 \text{ m/s}$ and smaller than the critical velocity v_c), the atoms are also channelled with turning point at the high potential areas in the standing wave. In a Gaussian standing wave, this channelling makes atoms emerge from the standing wave with only two possible output transverse velocities v_e and $-v_e$. The atoms with

$-v_e$ are focused to the atomic beam axis to form the central peak. For atoms with transverse velocity $v_t > v_c$, the transverse kinetic energy is larger than the potential energy of the standing wave, the gradient force has no effect on the atoms.

For small detunings, the diffusion processes play an important rule in decreasing the central peak of the spatial profile of the atomic beam and the formation of the central peak is the results of the competition between collimation, focusing and diffusion. Both collimation and diffusion are position independent. The focusing is position dependent and at different positions along the atomic beam axis, the focusing spot changes.

The experimental evidence showed this change of the focal spot, supporting the idea that the effect of a strong standing wave laser field is equivalent to imaging with a lens of variable focal length (zoom-lens). The focusing position of an atomic beam could be controlled by changing either intensity or the detuning of the standing wave. As the ratio v_{in}/v_{out} is not constant for all transverse velocities and increases with the intensity of the standing wave, the focusing of the atoms is chromatic. This kind of zoom-lens property is the effect of velocity dependent dipole force. The theoretical simulation results showed a good agreement with the experimental results except for some difference in the parameters (intensity and detuning) of the standing wave.

Chapter 7

Deflection and Doppleron Resonances

From the previous chapters, we know that in a strong standing wave laser field, the stimulated processes involving both traveling waves become important. By increasing the angle between the atomic beam and the standing wave, we can only let atoms with large transverse velocities ($v_t > v_c$) to interact with the standing wave. The averaged effects of the higher order force terms in the Fourier expansion (Eq.2.72) become zero as the transverse velocity almost remains the same ($\delta v_t = a\delta t = a \times \lambda/2v_t \ll v_t$, in which the coefficients of the higher order force terms keep the same) when the atom travels through a small distance of standing wave period ($\lambda/2$). In this case, only the spatial averaged force F_0 becomes important. From fig.2.2, for transverse velocity larger than the critical velocity v_c , the force F_0 no longer changes sign. Therefore, a collimated atomic beam with a small range of transverse velocity could experience deflection in the same direction (but with perhaps slightly different magnitude due to the Doppleron resonances) for all atoms in the beam.

Our purposes in this chapter are to investigate both the deflection of an atomic beam with large transverse velocity from a strong standing wave field, and the Doppleron resonances. The deflection was observed, but the Doppleron resonances were not found experimentally. We will give the explanation why the higher-order Doppleron resonance is difficult to observe experimentally.

By using the continued fraction solution, we calculated the transverse spatial distribution of an atomic beam nearly perpendicularly interacting with a strong standing wave laser field. The higher order Doppleron resonances would appear for

some critical conditions and are very sensitive to the detunings and the intensities of the standing wave laser field.

7.1 Experimental Arrangements And Procedures

The experimental arrangements for measuring the higher order Doppleron resonances are almost the same as described in Chapter 3. The difference in the experiments described in this chapter is that there is a small angle α between the atomic beam and a line normal to the strong standing wave laser field. By changing this angle, we could control the strong standing wave to interact with those atoms with variable transverse velocity range (achieved using different size of the slit in front of the standing wave) around a fixed central transverse velocity. The central transverse velocity of atoms interacting with the standing wave was calculated $v_t = v_l \sin \alpha$. If the divergent angle of the atomic beam was θ (half angle), the transverse velocity spread could be calculated by $\delta v_t = v_l(\sin(\alpha + \theta) - \sin(\alpha - \theta))$. (see fig.7.1).

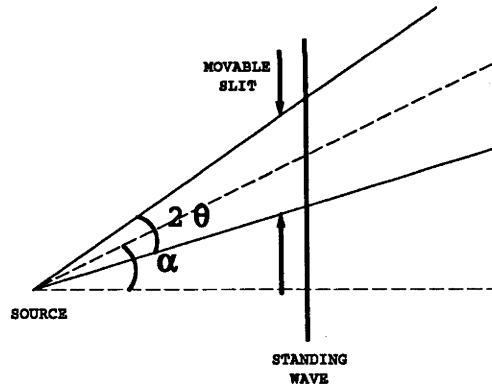


Figure 7.1: The transverse velocity of atoms interacting with the standing wave can be controlled by moving the slit. The transverse velocity divergence can be changed using different size of the slit.

In order to measure the angle between the atomic beam and the standing wave field, we first set the atomic beam at an exact perpendicular position to the standing wave laser field (using the method described in Chapter 6 to the standing wave laser field) by observing the focusing of the atoms in the atomic axis for larger detunings (normally within $1 - 2GHz$). The error of the perpendicular angle was about $0.13mrad$ which corresponds to $0.13m/s$ transverse velocity for atoms with a longitudinal velocity of $1000m/s$. The atomic beam was tilted by translating the

movable slit in front of the standing wave and the angle α was measured within an error of 0.01 degree which corresponds to 0.17 mrad. Accordingly, the change of the angle and the transverse velocity of atoms interacting with the standing wave laser field can be calculated.

In order to effectively observe the deflection, the smaller the transverse velocity spread, the easier to observe the deflection. For a large transverse velocity spread, the deflection could be washed out by the undeflected background atoms. A small slit with 0.5mm width in front of the standing wave laser field was used which produced a width of about 1.0mm of the initial atomic beam profile in the detector region.

7.2 Experimental Results

Fig.7.2 shows a series of measurements of the atomic beam profiles after interaction with a strong standing wave laser field with different detunings. The experimental parameters were as follows: The angle between the atomic beam and the standing wave laser field is $\alpha = 1.0^\circ$ (17.5mrad); the diameter of the standing wave was 1.6mm and the intensity (single beam) of the standing wave was 220mW, corresponding to a central saturation parameter $G_0 = 1700$; The longitudinal velocity was $v_l = 1000\text{m/s}$ which determined $v_l \times \alpha = 17.5\text{m/s}$ transverse velocity of atoms. The horizontal movable slit used in front of the standing wave was 0.5mm which allowed an atomic divergence angle of 0.36mrad (half angle). The vertical slit put in front of the standing wave was 0.3mm which allowed atoms only interacting with the central high intensity area of the Gaussian standing wave laser field.

Fig.7.3 shows the same result as fig.7.2 but with different angle ($\alpha = 1.5^\circ = 26.3\text{mrad}$) between the atomic beam and the standing wave.

It is clear from these figures that the deflection of the atomic beam was observed. For different detunings of the strong standing wave, the deflection angle of atoms is different and there is a maximum deflection angle for detunings around $|\Omega|/2\pi = 60\text{MHz}$. For detunings larger than 300MHz, the atoms were almost not affected.

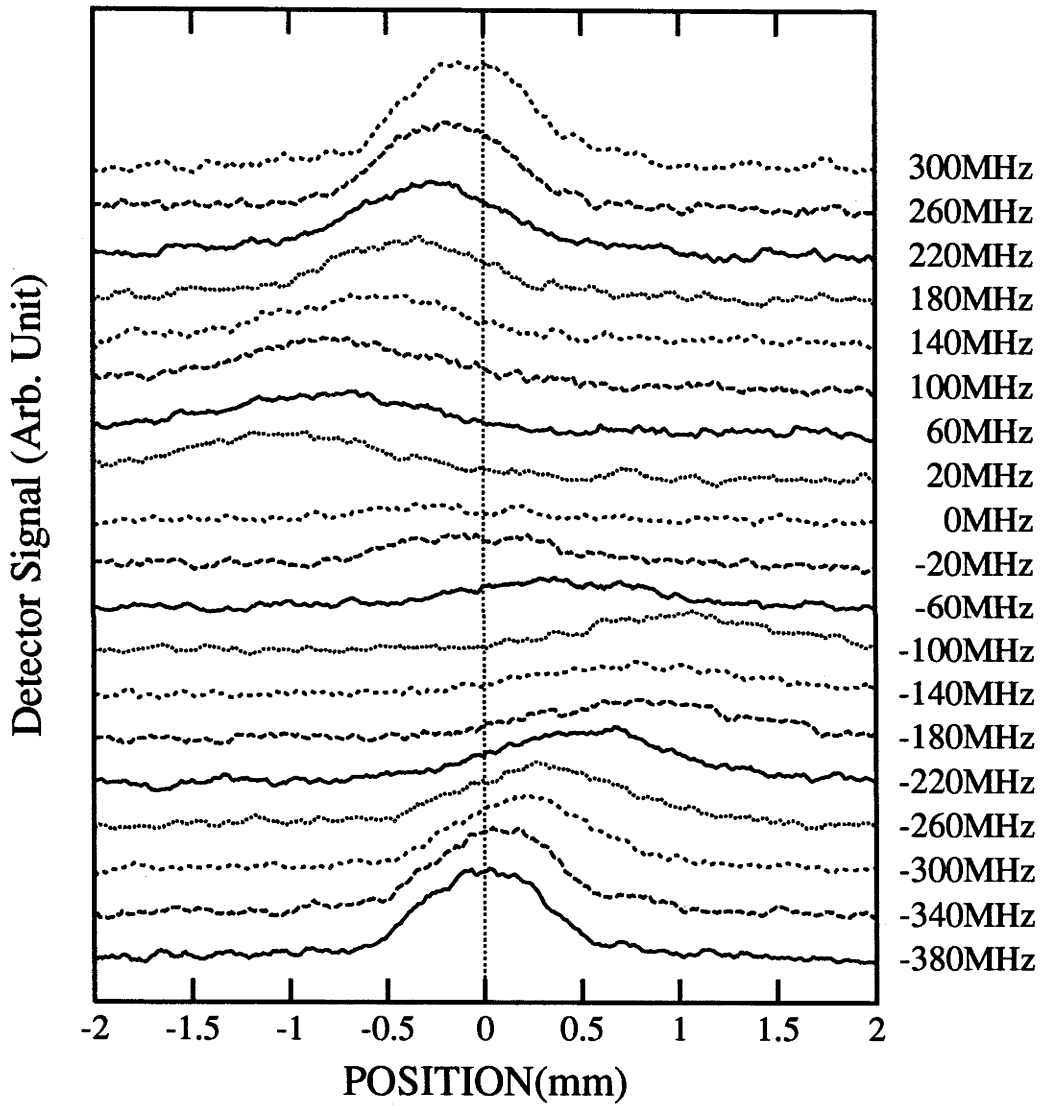


Figure 7.2: Deflection of atomic beam for different detunings of the standing wave laser field. The angle between the atomic beam and the standing wave was $\alpha = 17.5 \text{ mrad}$ with a divergence for the atomic beam of $\theta = 0.4 \text{ mrad}$.

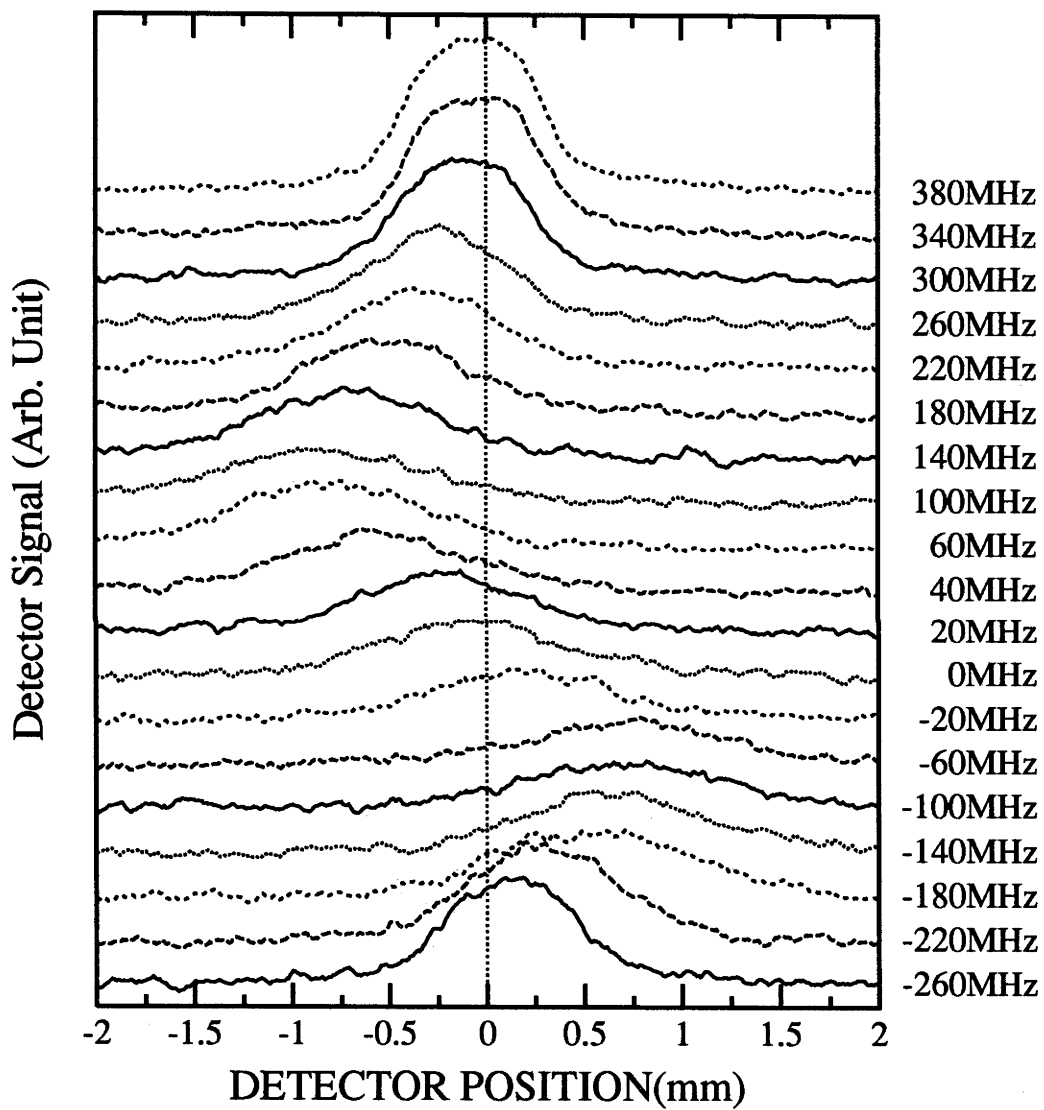


Figure 7.3: Deflection of atomic beam for different detunings of the standing wave laser field. The angle between the atomic beam and the standing wave was $\alpha = 26.3\text{mrad}$ with a divergence for the atomic beam of $\theta = 0.4\text{mrad}$.

7.3 Theoretical Simulation of the Deflection

In this experiment, the atomic beam was set not exactly perpendicular to the strong standing wave laser beam and the transverse kinetic energy of atoms was larger than the potential of the standing wave ($v_t \gg 2m/s$). The averaged effect of the higher order force coefficients in the Fourier force expansion term (Eq.2.72) were zero in this case. So in the simulation, only the spatial average force F_0 was considered to simulate the motion of atoms with large transverse velocity in the standing wave.

The frequency dependence of the force F_0 was shown in fig.7.4 for a fixed transverse velocity of $17.5m/s$. The saturation parameter was selected to be 1300 (Note that the saturation parameter G changed from 0 to 1700 in a Gaussian laser beam in the experiment). The maximum of the force was situated between $50MHz$ and $100MHz$ and for detunings larger than about $200MHz$, the force decreased rapidly.

The simulation of the deflection of an atomic beam under the same experimental condition as fig.7.2 was shown in fig.7.5.

Significant deflection of the atomic beam was predicted from the simulation. From fig.7.5, the largest deflection appeared at around $40MHz$ and there is no deflection for detunings larger than $100MHz$ which is about 3 times smaller than the experimental results.

Also it should be noted that from the simulation, the maximum deflection angle of the atomic beam is about 2 times larger than the experimental results. This discrepancy between the experimental and theoretical results is caused by the same effect discussed in Chapter 6 (e.g. multi-level system of sodium atoms).

Except for the difference in the parameters (detuning and intensity), the simulation predicted the deflection property of the atoms in a strong standing wave which is in agreement with the experimental results.

7.4 Theoretical Prediction of Higher Order Doppleron Resonances

Using the continued fraction solution, we simulated the near perpendicular interaction of an atomic beam with a standing wave laser field. The simulation of the transverse atomic beam profile was performed under different parameters. Because

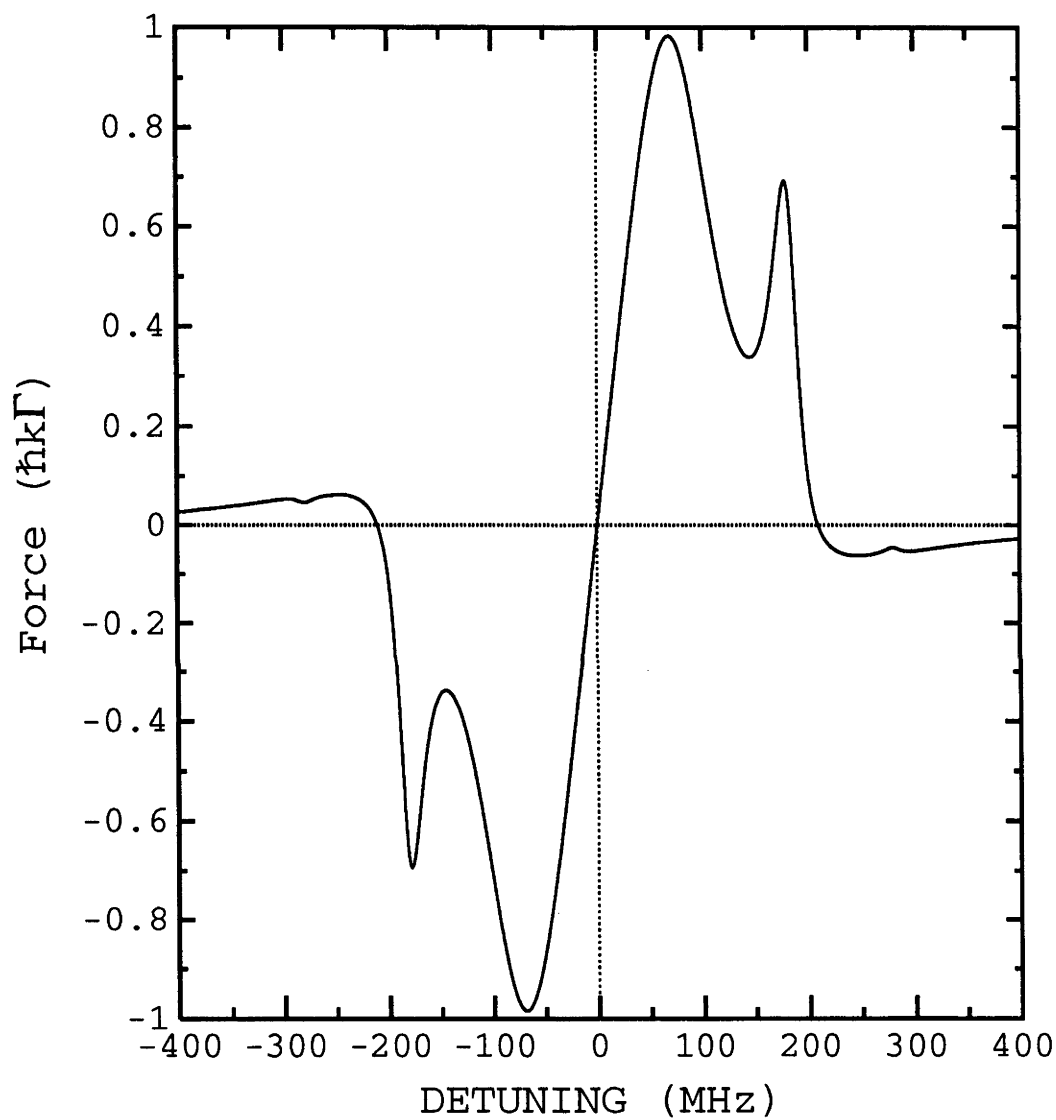


Figure 7.4: Force F_0 as function of detuning under condition: $v_t = 17.5\text{m/s}$ ($\alpha = 17.5\text{mrad}$), $G = 1300$.

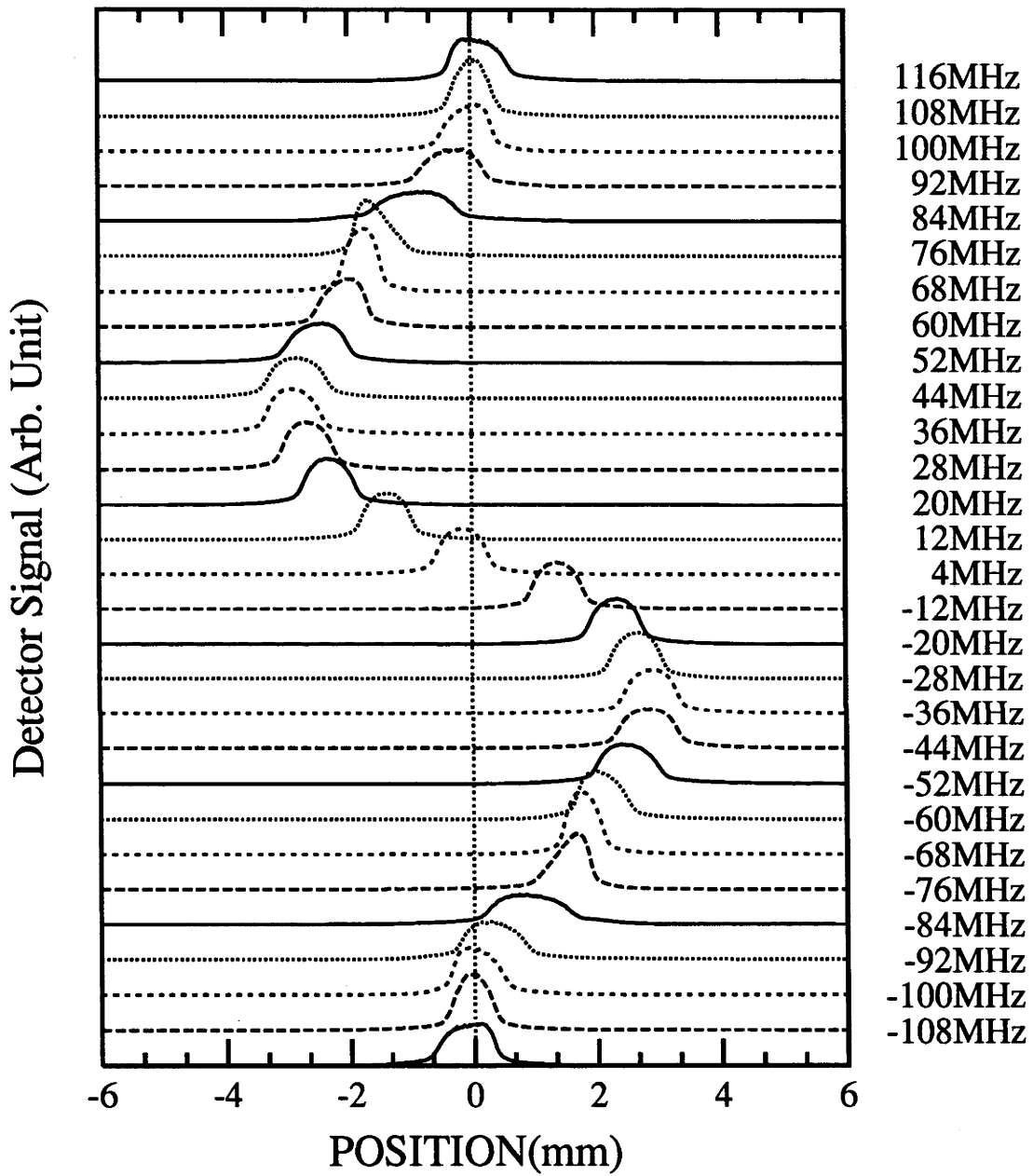


Figure 7.5: Simulation of the deflection of atomic beam under the same condition as fig. 7.3.

the transverse velocity of atoms in near perpendicular situation was larger than $2m/s$ and the averaged effect in a standing wave period of the higher order force terms in Eq.2.72 equal zero, it was not important to use the higher order forces in the force expression (Eq.2.72). So, in our simulation, only the zero order spatial averaged force F_0 was used to simulate the transverse distribution of the atomic beam.

In the simulation, the diameter of the standing wave was selected to be $4.2mm$ and the central saturation parameter was $G_0 = 140$, which corresponds to one of the experimental conditions (heating experiment, see Chapter 5). A large transverse velocity spread is required to observe the difference of the force for different transverse velocities. A large $1mm$ slit was placed in front of the standing wave and the distance from the oven nozzle to the standing wave was measured as $720mm$ and from the standing wave to the detector as $640mm$.

Fig.7.6 shows the changing of the atomic beam profile as function of detuning of the standing wave (from $+2MHz$ to $+100MHz$ in steps of $2MHz$). In this figure, the longitudinal velocity was $700m/s$. The angle between the atomic beam and the standing wave laser field was $6mrad$. Not only a significant deflection of the atomic beam was predicted but a multi-peak structure of the profile was clearly resolved from the simulation at various detunings. The multi-peak structure is very sensitive to the frequency of the standing wave.

Fig.7.7 shows the same simulation result as fig.7.6, but for $1000m/s$ longitudinal velocity. Because the atoms traveled faster than the atoms in Fig.7.6, the interaction time with the standing wave was shorter and then, the deflection angle was smaller than that in fig.7.6.

Fig.7.8, fig.7.9 and fig.7.10 show the simulation results of an atomic beam with $1000m/s$ longitudinal velocity interacting with the standing wave with larger angles between the atomic beam and the standing wave laser field. It is clear that only deflection was predicted and no multi-peak structure appeared.

In fact, a lot of simulations (over 50 graphics) of the atomic beam profiles like fig.6.12 were performed under different conditions (intensity, longitudinal velocity, angle between the atomic beam and the standing wave et al.) which can not be shown here because of the limitation of this thesis. In most cases, only deflection was predicted and just in a few critical cases, the multi-peak structure would appear.

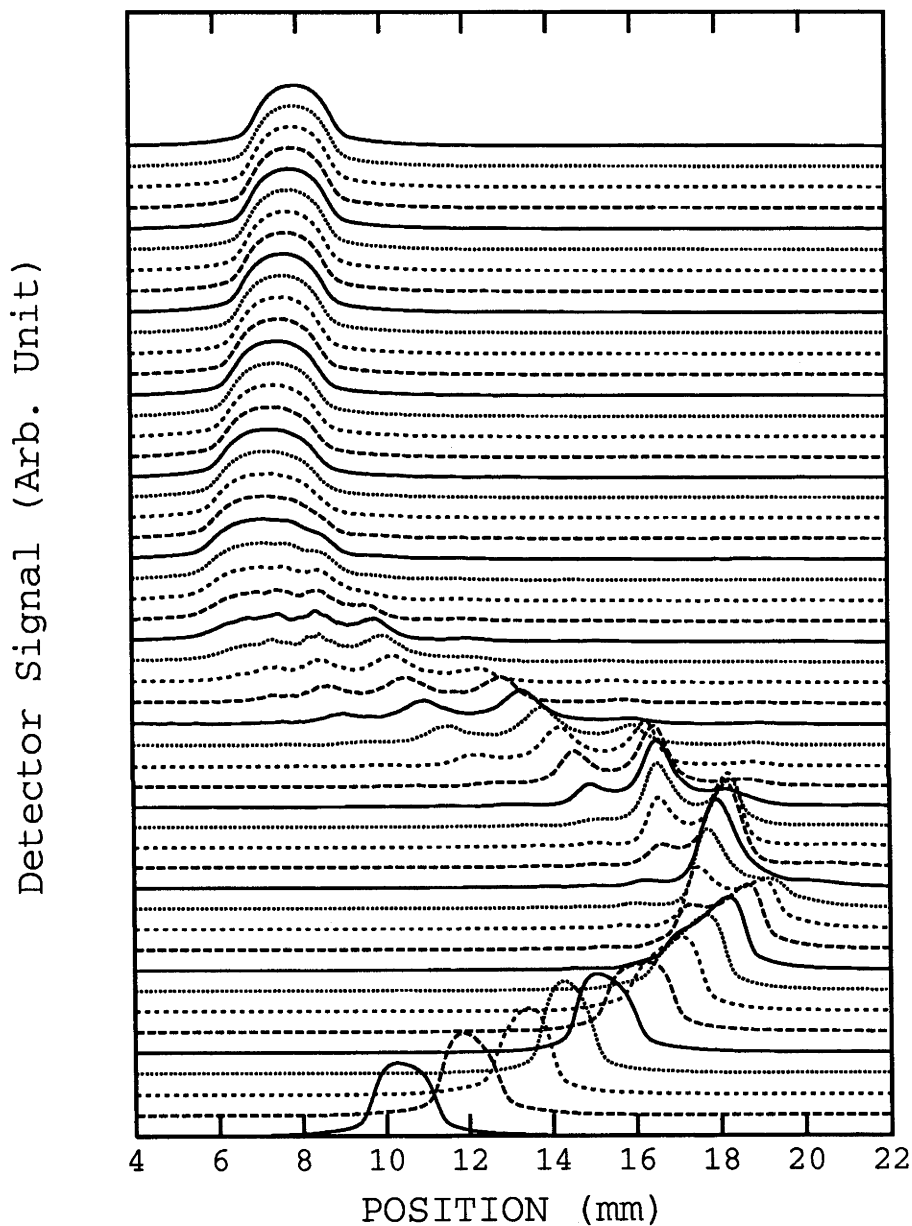


Figure 7.6: Simulated spatial profiles of an atomic beam interacting with a strong standing wave (peak saturation parameter $G_0 = 140$, $1/e$ intensity radius is 2.1mm) as a function of laser detuning (from 2MHz to 100MHz in steps of 2MHz). The angle between the normal to the standing wave and the atomic beam is 6mrad . The longitudinal velocity of the atoms is 700m/s . Simple deflection is evident for detuning less than 20MHz , while structure due to higher order Doppleron resonances is predicted for detuning between 20MHz and 60MHz .

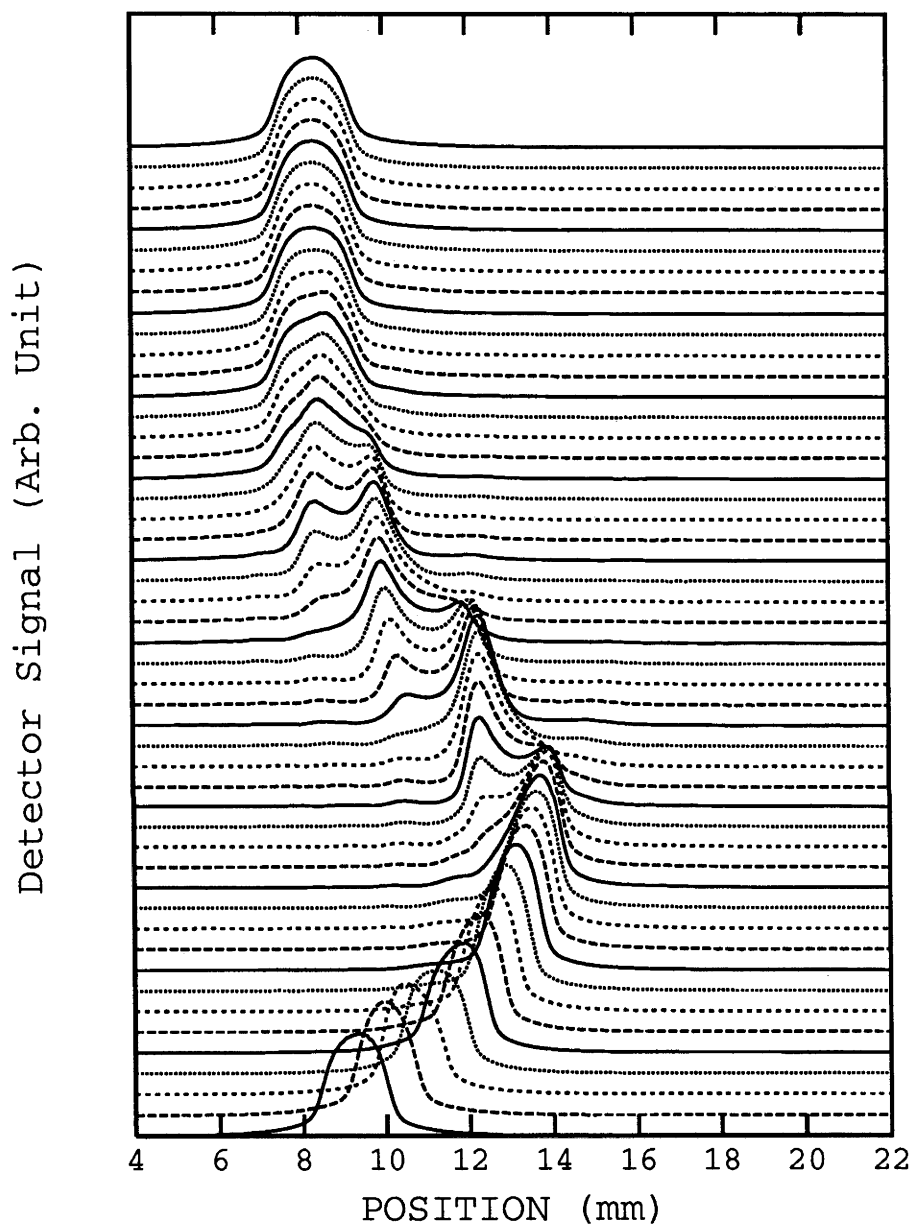


Figure 7.7: *Simulated spatial profiles of atoms with the longitudinal velocity of the atoms is 1000m/s and other parameters are the same as fig.7.6.*

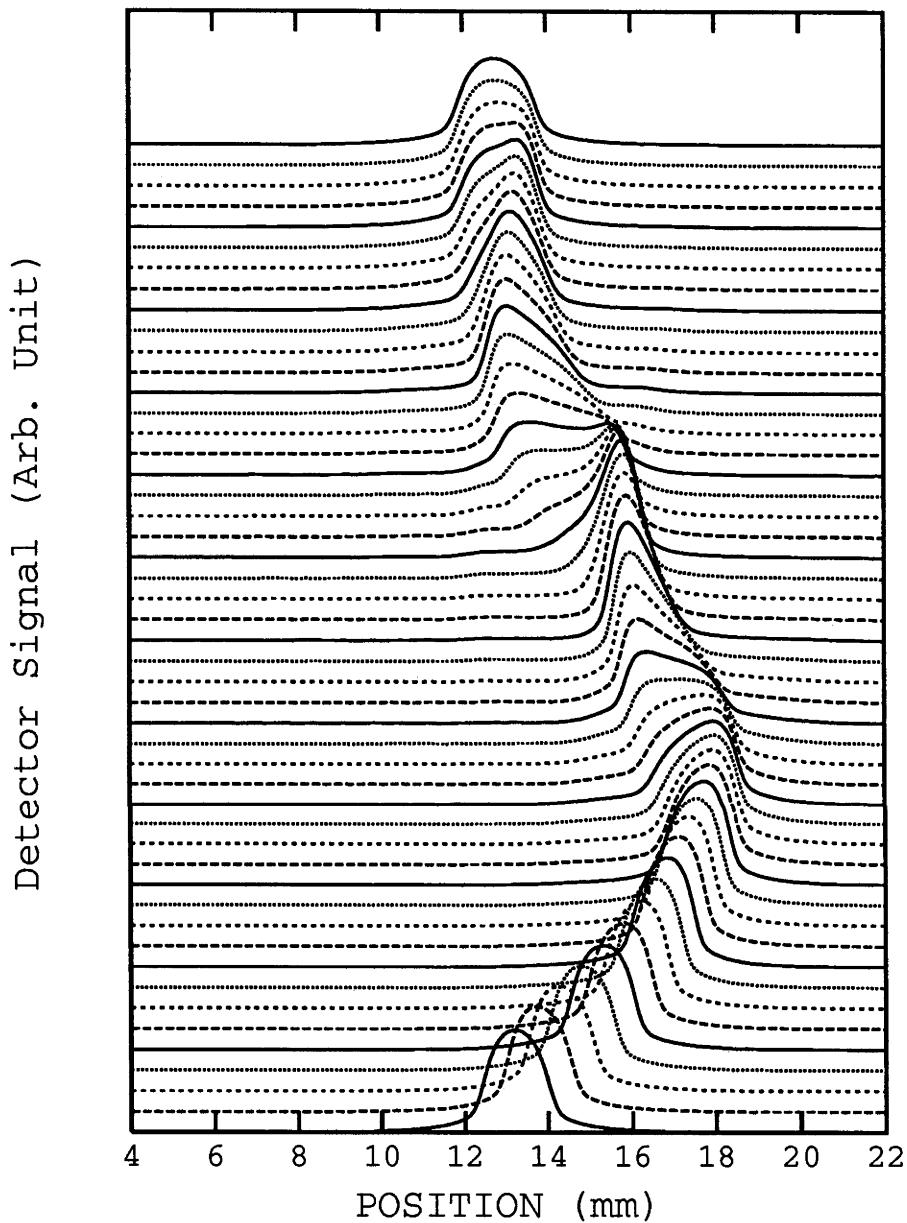


Figure 7.8: Simulated spatial profiles of atoms with the longitudinal velocity of the atoms is 1000m/s. The angle between the normal to the standing wave and the atomic beam is 9mrad and other parameters are the same as fig.7.6.

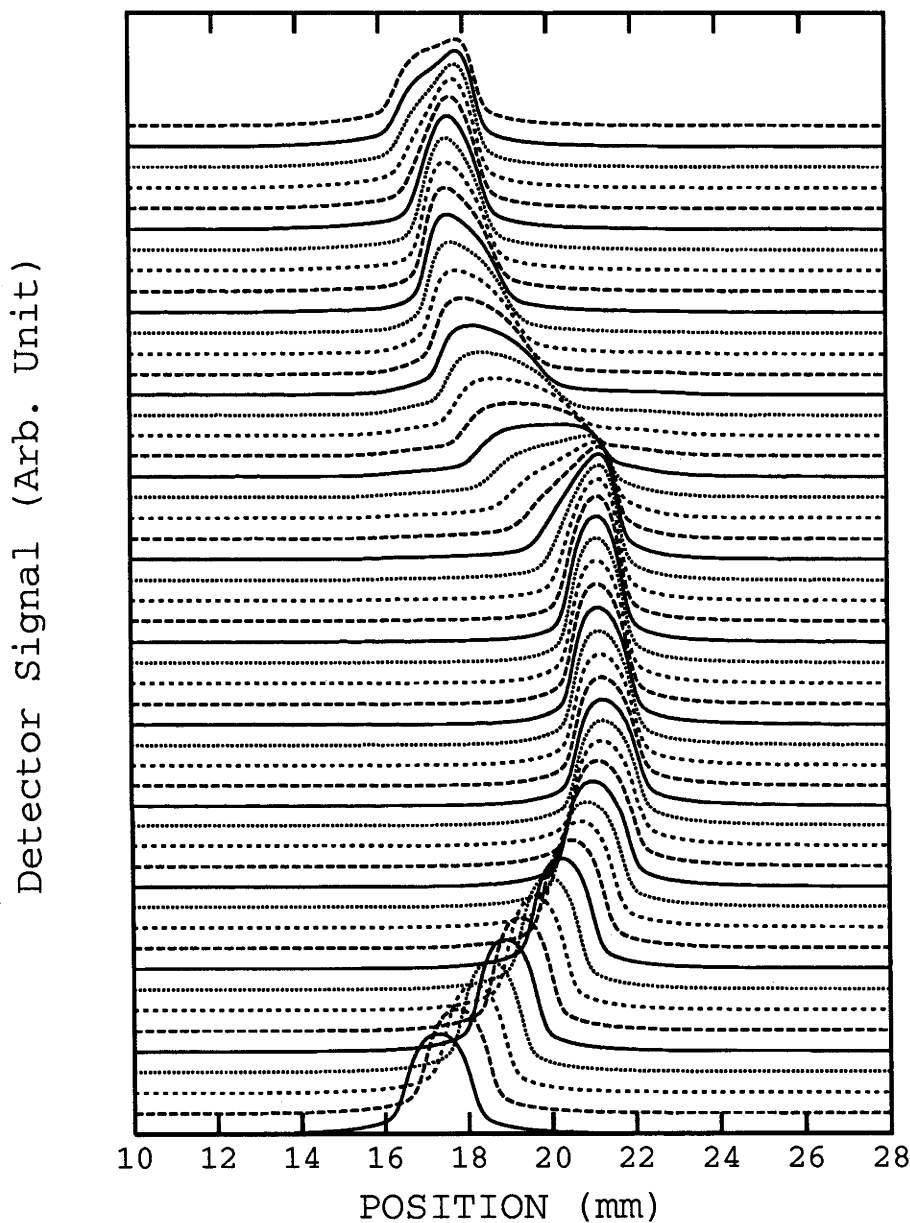


Figure 7.9: Simulated spatial profiles of atoms with the longitudinal velocity of the atoms is 1000m/s. The angle between the normal to the standing wave and the atomic beam is 12mrad and other parameters are the same as fig.7.6.

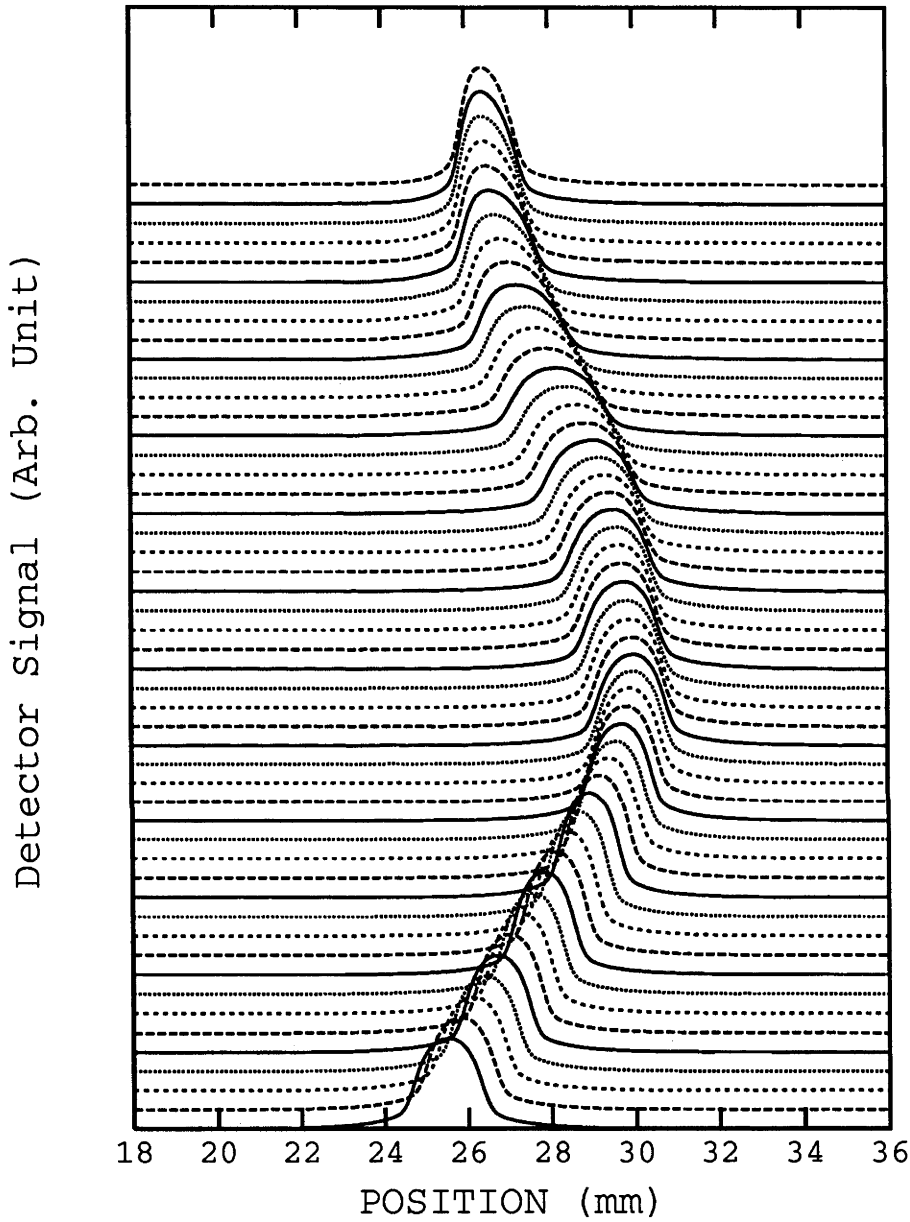


Figure 7.10: *Simulated spatial profiles of atoms with the longitudinal velocity of the atoms is 1000m/s. The angle between the normal to the standing wave and the atomic beam is 18mrad and other parameters are the same as fig.7.6.*

From the simulation, it appears that the higher order Doppleron resonances may be very difficult to observe. The multi-peak structure was very sensitive to the detuning and intensity of the standing wave and one would have to use highly stabilized (both frequency and intensity) dye lasers to observe the higher order Doppleron resonances experimentally.

We have done the experiments trying to observe the higher order Doppleron resonances, but the experimental results only showed the deflection of the atomic beam and no multi-peak structure was observed. The failure to observe the higher order Doppleron resonances experimentally maybe was due to the fluctuation of the intensity of the standing wave, and the diffusion processes in our experiment.

Fig.7.11 shows the influence of the intensity fluctuation of the standing wave. The solid line curve is one of the curves in fig.7.6 with detuning $+40MHz$. The other two curves (dashed and dotted lines) are calculated under the same conditions as solid curve but for different central saturation parameters. The intensity for dashed curve is $G_0 = 130$ and for dotted curve is $G_0 = 150$ ($G_0 = 140$ for solid curve) which give about 7 percent change of the intensity.

In our experiments, the intensity fluctuation of the standing wave laser was about 5%. Although we used a $1mm$ vertical slit in front of the standing wave beam to allow atoms interacting with strong uniform Gaussian laser area, still there is about 5.5% intensity change in the $1mm$ area ($0.055 = 1 - \exp[-(0.5/2.1)^2]$). The actual intensity change in our experiment was about 10%. It is clear from fig.7.11 that the peaks will be washed out if the intensity fluctuation of the standing wave is larger than 7 percent and no peaks can be observed.

Because the Doppleron resonances appear only at small detunings, the diffusion processes becomes important which also make it difficult to observe the higher order Doppleron resonances. In our experimental parameters, the diameter of the standing wave was $1.6mm$ in e^{-1} intensity region. For atoms with longitudinal velocity of $1000m/s$, the transit time through the standing wave was about $2\mu s$ which corresponds to about 120 spontaneous emissions for sodium atoms. The transverse velocity spread due to the spontaneous emission was about $\sqrt{120}v_r = 0.33m/s$, where v_r is the recoil velocity of atoms. The spatial distribution spread of atoms at the detector due to the spontaneous diffusion could be calculated as $0.33 \times 1360/1000 = 0.45mm$. From Chapter 2, we know that for a high intensity of the standing wave, the stimulated diffusion is larger than the spontaneous dif-

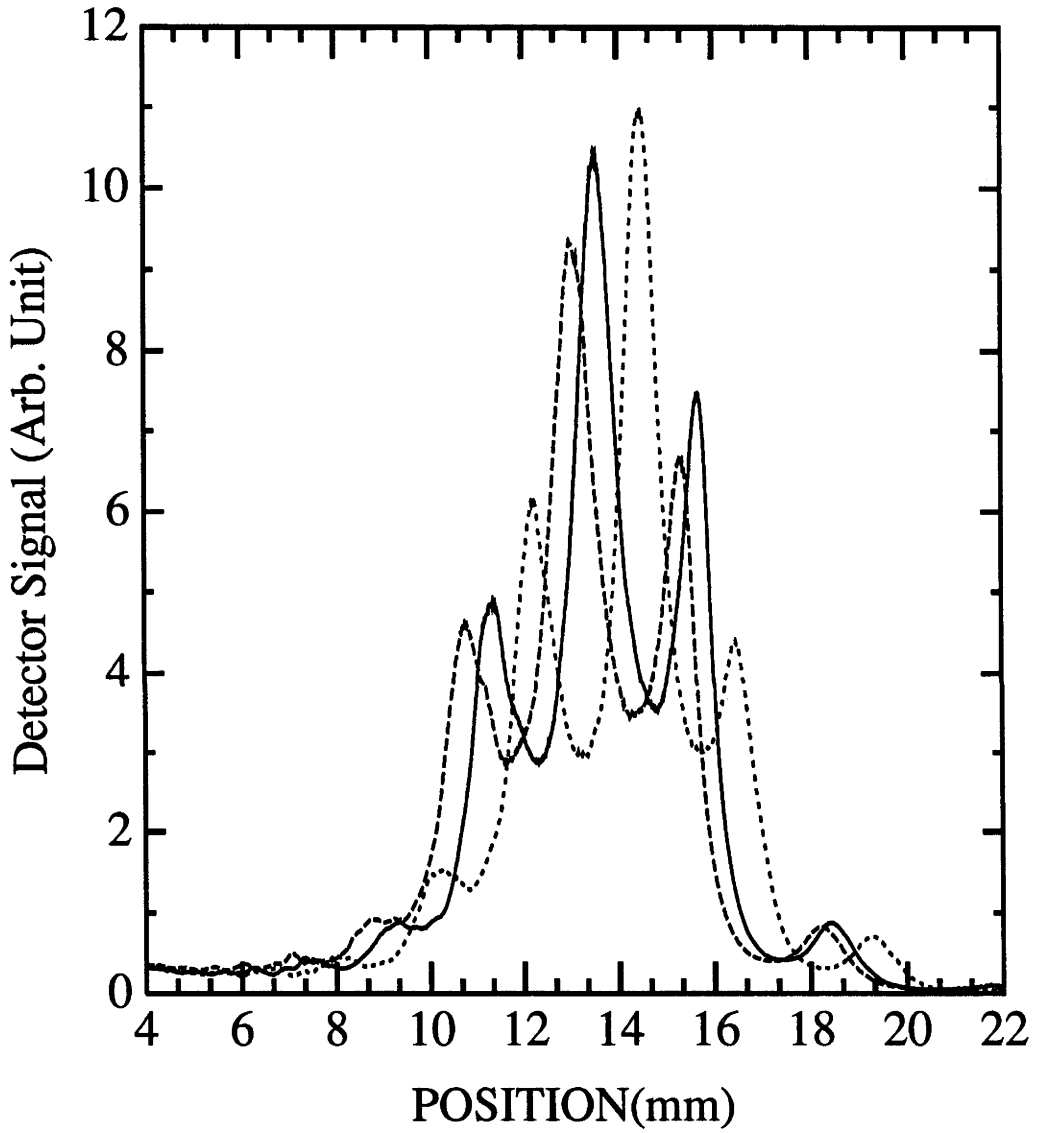


Figure 7.11: The deflection dependence on the intensity of the standing wave for a fixed detuning (40 MHz). Solid line: $G_0 = 140$; dotted line $G_0 = 150$ and dashed line $G_0 = 130$.

fusion, hence the diffusion processes were large enough to wash out the multi-peak structure.

7.5 Summary

In conclusion, the significant deflection of the atomic beam was observed as a function of laser detuning which is consistent with the predictions of a model based on a continued fraction solution of the light force.

The multi-peak structure associated with Doppleron resonances were predicted by the model but were not observed experimentally, probably due to the influence of intensity fluctuations and diffusion processes.

Chapter 8

Conclusion

The work which has been described in this thesis may be summarized as follows

(1). The light pressure force on an two-level atom moving in a light field was calculated using the Optical Bloch Equations (OBE) and the detailed procedures were given. We found that the simple gradient force in a standing wave laser field was only a special solution of the OBE for zero velocity or for large detunings where there are no dissipative effects. There is no analytical solution of the force for an atom with arbitrary velocity in a strong standing wave laser field. In this case, the continued fraction expansion method[42] was used to get a numerical solution of the force. It was found that the forces parallel to the path of atoms (longitudinal forces) can be ignored and it is sufficient to set $v_l = \text{constant}$

(2). Experiments have been performed to study the effect of a strong, near resonant, standing wave laser field on the transverse velocity distribution of a sodium atomic beam. The laser field was detuned negatively with respect to the atomic transition in order to distinguish the effects of light forces which lead to transverse heating and channeling of the atoms. In order to separate the contributions of the longitudinal and transverse velocity contributions to the far field spatial beam profile, a velocity sensitive detection system was used to select particular longitudinal velocity groups with high resolution.

(3). The experimental results showed that for larger detunings, the central peaks were more clearly resolved than for small detunings. In the cases of larger detunings, the spatial averaged force F_0 and diffusion processes are negligible and only the velocity independent dipole force (the gradient force) is important.

(4). The central peaks were studied in details in both experiments and simu-

lation. For large detuning, the central peaks were formed mainly by the collimation/focusing effect of the strong standing wave. Decreasing the detuning, both heating force (for negative detuning) and diffusion become more and more important and the diffusion reached an maximum at zero detuning of the standing wave laser field. Both of these processes would decrease the height of the central peaks of the atomic profiles, but in different ways. The heating force shifted the focusing points and, hence changed the focusing length which increased the focusing spot size and decreased the height of the peak. The diffusion processes would always decrease the height of the peak and broaden the width.

(5) The focusing of atoms passing near perpendicular to a negative detuned standing wave was observed in agreement with the model based on continued fraction solution. The focusing is predicted to be transverse velocity dependent and, thereby leading to the possibility of a variable focal length zoom lens for atoms.

In fact, the small central peaks of the experimental results (see fig.5.1 and fig.5.2 or fig.3 in Aspect et al) are due to both collimation and focusing. For small detunings of the standing wave, the diffusion processes are large and the small peaks are the results of the competition between the collimation/focusing and the diffusion. If there is no diffusion processes, the central peak should be much larger than the experimental results.

Experimental evidence was found for a zoom lens property of the standing wave acting on atoms. The focusing of atoms from a standing wave is **Chromatic** depending on the transverse as well as longitudinal velocity. From the experimental results, the central peak of the transverse profile of the atomic beam was dependent on both the intensity and detuning of the standing wave, because different parameters (intensity and detuning) of the standing wave can cause atoms to be focused at different position on the atomic beam axis. This is an effect corresponding to the focusing of light beam by different focal length lenses.

(6) For atoms with large transverse velocity ($\gg 1m/s$) interacting with with a strong standing wave, a significant deflection of the atomic beam was observed experimentally which depended on the detuning of the standing wave. The deflection was qualitatively consistent with the simulation using the continued fraction solution of the light force. Such an atomic deflector has applications for the control of an atomic beam in two dimensions.

(7) From the simulation, the higher order Doppleron resonances were predicted but found to be very sensitive to the intensity and detuning of the standing laser field. Because the width of the higher order Doppleron resonances is narrower than that of lower order Doppleron resonances, it is more difficult to observe the higher order Doppleron resonances than the lower order Doppleron resonance. In our experiment, only the significant deflection of the atomic beam was observed as a function of standing wave laser detuning. The structure of the Doppleron resonances was washed out, mostly due to the fluctuation of the intensity or the shift of the frequency of the standing wave. From our calculation, a 7% intensity change or a few MHz frequency shift of the standing wave will wash out the multi-peak structure. Because the Doppleron resonances only happen for small detunings (for large detuning, the probability of multi-photon process is low) for which the diffusion process becomes significant, this also makes the higher order Doppleron resonance structure to be observed experimentally much more difficult. From our

	Small v_t	Large v_t
Large Detuning Ω	1:1 Imaging	Little Effect
Small Detuning Ω	Heating, Collimation, Zoom-Lens	Frequency Dependent Deflection

experimental and theoretical results, for different parameters (transverse velocity of atoms, detuning and intensity of the standing wave laser field), the different effects due to the interaction of atomic beam with the standing wave laser field were observed. The above table summarized the effects of atomic beam interacting with a standing wave laser field.

For large detunings, the standing wave acts like a conservative potential (gradient

force) and atoms with small transverse velocity will be channelled in this potential. For atoms with small transverse velocity (e.g. 0.1m/s in Chapter 5), the atoms will be collimated within a small regime around $v_t = 0$. For $0.1 < v_t < \text{capture velocity}$, the output velocity of atoms from the standing wave has mainly two directions: most atoms either travel along the original direction or are specularly reflected. In this case the specularly reflected atoms will be focused with 1 : 1 imaging length.

For atoms with transverse velocity larger than the capture velocity, the kinetic energy of atoms will be larger than the potential energy of the standing wave and the atoms will keep their original travelling direction. Standing waves with large detuning will have almost no effect on atoms.

For small detunings, the non-conservative force becomes important and the magnitude of the output transverse velocity of atoms from the standing wave will not be equal to that of the input transverse velocity. For different detunings, the magnitude of the output transverse velocity can be either larger (for small negative detunings) or smaller (for small positive detunings) than that of the input transverse velocity. Heating (for negative detuning) or cooling (for positive detuning) becomes important for atoms with small transverse velocity which can cause the atoms to be focused at atomic axis with variable focusing length (zoom-lens).

For atoms with large transverse velocity (larger than the capture velocity), the atoms will not be affected by the periodic standing wave potential and only spatial averaged force will affect the motion of atoms. Because the spatial averaged force F_0 is both velocity and detuning dependent, the atoms can be deflected to different position for different detuning and transverse velocity.

The present experimental results were generally in agreement with the theoretical simulation.

This study could be extended by further experiments on the interaction of an atomic beam with a standing wave laser wave field which can be summarized as follows

- (1). Using a movable detector (along the atomic beam axis) to further verify the zoom-lens property of the standing wave.
- (2). Because the central peak is formed by two effects: collimation and focusing, it will be better to further investigate the contribution of these two effects to the

central peak. One possible way to do this is as follows. First the detector is set at the focusing point to measure the central peak height. Second, move the detector far away from the focusing point to measure the central peak height again under the same experimental condition. By comparing these two peaks, the collimation can be distinguished from focusing effect. This is based on the fact that the collimated atoms have very small divergence angle while the focused atoms have large divergence angle. When the detector is far away from the focal point, the peak formed by collimation (which will be still at the central position) will be separated from the peak formed by focusing (which will move away from the central position).

(3). Two-dimension experiments to observe the change of the central peak. If the two-dimension standing waves are formed with the same frequency and intensity, a uniform distribution (normally in a circular shape) of the central peak should be observed. If the frequency and intensity are different, the different shapes of the central focused peak could be shown which could be useful in the atomic lithography.

(4). Other configuration (e.g. multi-path standing waves; cone mirrors) of the standing wave laser fields could be used to greatly enhance the atomic flux in a very small area.

(5) Using positively detuned standing wave to cool and collimate that atomic beam near the atomic axis.

Appendix

Magnetic-optic Trap of Sodium Atoms in a Glass Vapor Cell

As part of my Ph.D. work, I spent about half a year on building and operating a magnetic-optic trap of Na atoms in a vapor cell with the help of Dr. I.C.M. Littler (post doctor) in the Department of Physics & Theoretical Physics, the Australian National University.

In our experiment, we observed a cloud of cold sodium atoms using a magnet-optical trap. The experimental set-up consists of a sodium cell, three orthogonally trapping beams generated by a commercial dye laser (Coherent 699), and an inhomogeneous magnetic field. The glass cell is a spherical shape with good-quality optical windows. It is connected to an ion pump and to a sodium reservoir which is heated to about 100°C , so that in the operating conditions the cell contains a low pressure of sodium vapour of the order of 10^{-8} Torr. Each trapping beam contains a pair of counterpropagating waves with opposite circular polarisations (σ^+ and σ^-), having an intensity of $10\text{mW}/\text{cm}^2$ and a diameter of 1cm . The frequency of these beams is detuned by a few linewidths to the red side of the transition frequency of Na atoms $3^2S_{1/2}(F=2) \longrightarrow 3^2P_{3/2}(F'=3)$. In order to avoid optical pumping to the $3^2S_{1/2}(F=1)$ ground state, an EO modulator with 886MHz sideband is used to recycle the atoms. The inhomogeneous magnetic field is produced by coils in the anti-Helmoltz position and its gradient is about $5\text{Gauss}/\text{cm}$ in the symmetry plane of the coils and $10\text{Gauss}/\text{cm}$ along their axis.

The density and the temperature of the trapped atoms was measured by Dr. I.C.M. Littler. We obtained a cloud of about 8.4×10^6 sodium atoms of about 2mm in diameter ($2 \times 10^9/\text{cm}^3$). The typical temperature of the cloud is about $200\mu\text{K}$, which gives a Doppler width much smaller than the natural width. As the trapped atoms respond very sensitively to the frequency of the laser, (because they have been cooled to near the Doppler limit), we can use this trap to set the laser frequency to the atomic transition frequency $3^2S_{1/2}(F=2) \longrightarrow 3^2P_{3/2}(F'=3)$ with a uncertainty of 20MHz .

Bibliography

- [1] J.C.Maxwell, A Treatise On Electricity and Magnetism, 3rd Edition, V.2 (Clarendon Press, Oxford, 1982), P.440
- [2] O.R.Frisch, Zs. Phys. 86, 42 (1933)
- [3] A.Ashkin and J.M.Dziedzic, Appl. Phys. Lett., 19, 283 (1971)
- [4] A.Ashkin, Sci. Amer. 63, 226 (1972)
- [5] D.J.Wineland and H.J.Dehmelt, Bullet. Amer. Phys. Soc., 20, 637 (1975)
- [6] H.J.Dehmelt, Nature, 262, 777 (1976)
- [7] H.J.Hänsch and A.L.Schawlow, Opt. Commun. 13, 68 (1975)
- [8] A.Ashkin, Science 210, 1081 (1980)
- [9] V.S.Letokhov and V.G.Minogin, Physics Reports 73 1 (1981)
- [10] H.Dehmelt, Advances in laser spectroscopy, ed. by F.T.Arecchi, F.Strumia, and H.Walther, (Plenum Press, New York, 1983), p.153
- [11] D.J.Wineland and W.M.Itano, Phys. Rev. A20, 1521 (1979)
- [12] S.Stenholm, Rev. Mod. Phys. 58, 699 (1986)
- [13] D.J.Wineland and W.M.Itano, Physics Today 34, (June 1987)
- [14] S.Chu, Science 253, 861 (1991)
- [15] D.Philips, P.I.Gould, P.D.Lett, science 239, 878 (1991)
- [16] C.Cohen-Tannoudji, **Fundamental systems in Quantum Optics**, (Elsevier Science Publ., B.V., 1991)
- [17] P.Meystre and S.Stenholm, eds. J.Opt.Soc.Am. B5 No.11, 1706 (1985)
- [18] S.Chu and C.Wieman, eds. J.Opt.Soc.Am. B6, 2109 (1990)
- [19] V.G.Minogin and V.S.Letokhov, **Laser Light Pressure on Atoms**. (Gordon and Breach, N.Y., 1987).
- [20] A.P.Kazantsev, G.I.Surdutovich, and V.P.Yakovlev, **Mechanical Action of Light on Atoms**, (World Scientific Publishing Co., Singapore, 1991)
- [21] L.Moi, S.Gozzini, C.Gabbanini, E.Arimondo and F.Strumia, eds. **Light Induced Kinetic Effects**, (ETS Editrice, Piza, 1991).
- [22] J.P.Gordon and A.Ashkin, Phys.Rev.Lett. 21, 1606 (1980)
- [23] S.Stenholm, Phys.Rev.A 27, 2513 (1983)

- [24] M.Preitiss and A.Cable, *Phys.Rev.Lett.* 62, 1354 (1989)
- [25] D.Gottesman, J.Mervis, M.Preitiss and N.P.Bigelow, *Phys.Rev. A* 46, 356, (1992)
- [26] M.Preitiss, A.Cable and N.P.Bigelow, *J.O.S.A. B*6, 2155 (1989)
- [27] M.G.Preitiss and S.Ezekiel, *Phys.Rev.Lett.*56, 46 (1986)
- [28] C.Salomon, J.Dalibard, A.Aspect, H.Metcalf and C.Cohen- Tannoudji, *Phys. Rev. Lett.* 59, 1659 (1987)
- [29] V.I.Balykin, V.S.Letokhov, Yu.B.Ovchinnikov, A.I.Sidorov and S.V.Shul'ga, *Opt. Lett.* 13, 958 (1988)
- [30] V.I.Balykin, Yu.E.Loikov, Yu.B.Ovchinnikov, A.I.Sidorov, S.V.Shul'ga and V.S.Letokhov, *J.O.S.A. B*6, 2178 (1989)
- [31] Yu.B.Ovchinnikov and V.S.Letokhov, *Comm.Atom.Molec.Phys.* 27, 185 (1992)
- [32] C.I.Westbrook, R.N.Watts, C.E.Tanner, S.L.Rolston, W.D.Phillips, P.D.Lett and P.L.Gould, *Phys.Rev.Lett.* 65, 33 (1990)
- [33] P.Verkerk, B.Lounis, C.Salomon, C.Cohen-Tannoudji, J.-Y.Courtois and G.Grynberg, *Phys.Rev.Lett.* 68, 3861 (1992)
- [34] P.S.Jessen, C.Gerz, P.D.Lett, W.D.Phillips, S.L.Rolston, R.J.C.Spreeuw and C.I.Westbrook, *Phys.Rev.Lett.* 69, 49 (1992)
- [35] P.R.Hemmer, M.S.Shahriar, M.G.Preitiss, D.P.Katz, K.Berggren, J.Mervis and N.P.Bigelow, *Phys.Rev.Lett.* 68, 3148 (1992)
- [36] P.L.Gould, G.A.Ruff and D.E.Pritchard, *Phys. Rev. Lett.* 56, 827 (1986)
- [37] P.J.Martin, B.G.Oldaker, A.H.Miklich and D.E.Pritchard, *Phys. Rev. Lett.* 60, 515 (1988)
- [38] G.Timp, R.E.Behringer, D.M.Tennant, J.E.Cunningham, M.Preitiss and K.K.Berggren, *Phys.Rev.Lett.* 69, 1636 (1992)
- [39] P.D.Lett, W.D.Phillips, S.R.Rolston, C.E.Tanner, R.N.Watts and C.I.Westbrook, *J.O.S.A. B*6, 2084 (1989)
- [40] J.Dalibard and C.Cohen-Tannoudji, *J.O.S.A. B*2, 1707 (1985)
- [41] E.Kyrölä and S.Stenholm, *Opt.Comm.* 22, 123 (1977)
- [42] V.G.Minogin and O.T.Serimaa, *Opt. Commun*, 30, 373 (1979)
- [43] S.Stenholm and W.E.Lamb, Jr. *Phys. Rev.* 181, 618 (1969)
- [44] E.Kyrola and S.Stenholm, *Opt. Commun.* 22, 123 (1979)
- [45] N.P.Bigelow and M.G.Preitiss, *Phys. Rev. Lett.* 65, 555 (1990)
- [46] J.J.Tollett, J.Chen, N.W.M.Ritchie, C.C.Bradley and Randall G.Hulet, *Phys. Rev. Lett.* 65, 559 (1990)
- [47] T.Esslinger, A.Hemmerich and T.W.Hänsch, *Opt. Commun.* 93, 49 (1993)
- [48] J.E.Bjorkholm, R.R.Freeman, A.Ashkin and D.B.Pearson, *Phys. Rev. Lett.* 41, 1361 (1978)
- [49] J.E.Bjorkholm, R.R.Freeman, A.Ashkin and D.B.Pearson, *Opt. Lett.* 5, 111 (1980)
- [50] V.I.Balykin, V.S.Letokhov, Yu.B.Ovchinnikov and A.I.Sidorov, *J.Mod.Optics* 35, 17 (1988)
- [51] V.I.Balykin and V.S.Letokhov, *Opt. Comm.* 64, 151 (1987)

- [52] S.Stenholm, Reviews of Modern Physics 58, 699 (1986)
- [53] Ph.D. Thesis of Bruce Stenlake in the Australian National University.
- [54] N.F. Ramsey, **Molecular Beams**. Oxford, Clarendon Press, 1956.
- [55] E.L.Raab, M.Prentiss, Alex Cable, Steven Chu and D.E.Pritchard Phys.Rev.Lett. 59, 2631 (1987)
- [56] H.R.Gray, R.M.Whitley and C.R.Stroud, Opt. Lett. 3, 218 (1978)
- [57] M.L.Citron, H.R.Cray, C.W.Cabel and C.R.Stroud, Phys.Rev. 16, 1507 (1977)
- [58] V.I.Balykin and A.Z.Sidorov, Kvantovaya Elektron. 11, 2001 (1984)
- [59] J.Dalibard and C.Cohen-Tannoudji, J.Opt.Soc.Am. B2, 1707 (1985)
- [60] R.J.Cook, Phys.Rev.A22, 1078 (1980)
- [61] R.G.DeVoe, Opt.Lett. 16, 1605 (1991)
- [62] A.P.Kazantsev, Sov. Phys. JETP 39, 784 (1974)
- [63] A.P.Kazantsev, G.A.Ryabenko, G.I.Surdutovich and V.P.Yakovlev, Phys. Reports 129, 75 (1985)
- [64] A.Ashkin, Phys. Rev. Lett. 40, 729 (1978)
- [65] David Park, **Introduction to Quantum Theory**, p299, Eq.10.14
- [66] A.Aspect, J.Dalibard, A.Heidmann, C.Salomon and C.Cohen- Tannoudji, Phys. Rev. Lett. 57, 1688 (1986)
- [67] J.Dalibard, A.Heidmann, C.Salomon, A.Aspect H.Metcalf and C.Cohen- Tannoudji, **Fundamentals of Quantum Optics II**, F.Ehottzky (ed.), Springer verlag, Berlin, 196 (1987)
- [68] C.E.Tanner, B.P.Masterson and C.E.Wieman, Opt. Lett. 13, 357 (1988)
- [69] Jian Chen, J.G.Story, J.J.Tollett and Randall G.Hulet, Phys. Rev. Lett. 69, 1344 (1992)
- [70] Y.Z.Wang, W.Q.Cai, Y.D.Cheng, L.Liu, Y.Luo and X.D.Zhang, Phys.Rev.A 42, 4032 (1990)
- [71] Y.Z.Wang, L.Liu, X.Z.Chen, X.J.Wang, S.W.Fang, W.Q.Cai, S.Y.Zhou and Y.S.Liu, Appl. Phys. B 58, 327 (1994),
- [72] J.J.Tollett, J.G.Story and Randall G.Hulet, Phys.Rev.A 47, 2128 (1993)